LOHANNA FERREIRA PAIVA

AERODYNAMIC ANALYSIS OF BIOINSPIRED BLADES BASED ON CERRADO SEEDS FOR SMALL-SCALE WIND TURBINES

Universidade Federal de Uberlândia

Faculdade de Engenharia Mecânica

2024

LOHANNA FERREIRA PAIVA

AERODYNAMIC ANALYSIS OF BIOINSPIRED BLADES BASED ON CERRADO SEEDS FOR SMALL-SCALE WIND TURBINES

Dissertação submetida ao Programa de Pós-Graduação em Engenharia Mecânica da Universidade Federal de Uberlândia como requisito para obtenção de título de **Mestre em Engenharia Mecânica.**

Área de concentração: Mecânica dos Fluidos

Orientador: Prof. Dr. Aldemir Aparecido Cavallini Junior

Co-orientador: Prof. Dr. Odenir de Almeida

UBERLÂNDIA - MG

2024

UNIVERSIDADE FEDERAL DE UBERLÂNDIA
Coordenação do Programa de Pós-Graduação em Engenharia
Mecânica
Av. João Naves de Ávila, nº 2121, Bloco 1M, Sala 212 - Bairro Santa Mônica, Uberlândia-
MG, CEP 38400-902
Telefone: (34) 3239-4282 - www.posmecanicaufu.com.br - secposmec@mecanica.ufu.br

ATA DE DEFESA - PÓS-GRADUAÇÃO

Programa de Pós-Graduação em:	Engenharia Mecânica
Defesa de:	Dissertação de Mestrado Acadêmico, nº 644, PPGEM

Data:	31/01/2024	Hora de início:	14:00	Hora de encerramento:	16:40

Matrícula do Discente:	12122EMC006
Nome do Discente:	Lohanna Ferreira Paiva
Título do Trabalho:	Aerodynamic Analysis of Bioinspired Blades Based on Cerrado Seeds for Small-Scale Wind Turbines
Área de concentração:	Transferência de Calor e Mecânica dos Fluidos
Linha de pesquisa:	Dinâmica dos Fluidos e Transferência de Calor
Projeto de Pesquisa de vinculação:	

Reuniu-se por meio de videoconferência a Banca Examinadora, designada pelo Colegiado do Programa de Pós-graduação em Engenharia Mecânica, composta pelos professores doutores: João Marcelo Vedovotto - FEMEC/UFU; Demetrio Cornilios Zachariadis - USP, Odenir de Almeida- FEMEC/UFU, coorientador da candidata, e Aldemir Aparecido Cavallini Junior - FEMEC/UFU, orientador da candidata.

Iniciando os trabalhos, o presidente da mesa, Dr. Aldemir Aparecido Cavallini Junior, apresentou a Comissão Examinadora e a candidata, agradeceu a presença do público, e concedeu à Discente a palavra para a exposição do seu trabalho. A duração da apresentação da Discente e o tempo de arguição e resposta foram conforme as normas do Programa.

A seguir o senhor(a) presidente concedeu a palavra, pela ordem sucessivamente, aos(às) examinadores(as), que passaram a arguir o(a) candidato(a). Ultimada a arguição, que se desenvolveu dentro dos termos regimentais, a Banca, em sessão secreta, atribuiu o resultado final, considerando o(a) candidato(a):

Aprovada.

Esta defesa faz parte dos requisitos necessários à obtenção do título de Mestre.

O competente diploma será expedido após cumprimento dos demais requisitos, conforme as normas do Programa, a legislação pertinente e a regulamentação interna da UFU.

Nada mais havendo a tratar foram encerrados os trabalhos. Foi lavrada a presente ata que após lida e achada conforme foi assinada pela Banca Examinadora.

Documento assinado eletronicamente por **Odenir de Almeida**, **Professor(a) do Magistério Superior**, em 14/05/2025, às 09:36, conforme horário oficial de Brasília, com fundamento no art. 6º, § 1º, do Decreto nº 8.539, de 8 de outubro de 2015.

Documento assinado eletronicamente por **João Marcelo Vedovotto**, **Professor(a) do Magistério Superior**, em 19/05/2025, às 14:17, conforme horário oficial de Brasília, com fundamento no art. 6º, § 1º, do Decreto nº 8.539, de 8 de outubro de 2015.

Documento assinado eletronicamente por **Aldemir Aparecido Cavalini Junior**, **Professor(a) do Magistério Superior**, em 10/06/2025, às 09:01, conforme horário oficial de Brasília, com fundamento no art. 6º, § 1º, do Decreto nº 8.539, de 8 de outubro de 2015.

A autenticidade deste documento pode ser conferida no site https://www.sei.ufu.br/sei/controlador_externo.php?acao=documento_conferir&id_orgao_acesso_externo=0, informando o código verificador **6326011** e o código CRC **07A78636**.

AERODYNAMIC ANALYSIS OF BIOINSPIRED BLADES BASED ON CERRADO SEEDS FOR SMALL-SCALE WIND TURBINES

Dissertação **APROVADA** pelo Programa de Pós-Graduação em Engenharia Mecânica da Faculdade de Engenharia Mecânica Federal de Uberlândia.

BANCA EXAMINADORA

_____
Prof. Dr. Aldemir Aparecido Cavallini Junior – Orientador
Universidade Federal de Uberlândia

_____
Prof. Dr. Odenir de Almeida – Co-orientador
Universidade Federal de Uberlândia

_____
Prof. Dr. João Marcelo Vedovotto
Universidade Federal de Uberlândia

_____
Prof. Dr. Demétrio Cornilios Zachariadis
Universidade de São Paulo

UBERLÂNDIA - MG

2024

"The Earth speaks to all of us,
and if we listen, we can understand."
Castle in the Sky (1986) – Hayo Miyazaki.

ACKNOWLEDGMENT

RESUMO

A crescente demanda por fontes de energia sustentável impulsionou pesquisas intensivas em tecnologias renováveis, e a energia eólica emerge como uma protagonista no cenário da energia verde. Nesse contexto, a otimização de pás de turbinas eólicas desempenha um papel crucial para a eficiência global dos sistemas de geração de energia eólica. A busca por designs mais eficientes e inovadores leva à aplicação de abordagens bioinspiradas, onde os princípios da natureza são incorporados para aprimorar o desempenho aerodinâmico. Dessa forma, esta dissertação abrange uma investigação inédita das propriedades aerodinâmicas de samarídeo do Cerrado, destacando o comportamento de autorotação, padrões de fluxo e velocidades de queda livre. A análise experimental em túnel de vento foi complementada por simulações RANS (*Reynolds-Averaged Navier-Stokes*) para o samarídeo (em escala real), a pá de referência de geometria convencional baseado nos aerófólios SG6043 sem ângulo de ataque e a pá bioinspirada (com redução de solidez), e simulações QBlade para a pá de referência. Para isso utilizou-se o software ANSYS Fluent®, usando o modelo *Moving Frame Reference* – MRF, empregado para modelar o fluxo de ar ao redor da turbina. As simulações cobriram uma faixa de velocidade do vento de 4 a 12 m/s, com acréscimo de 2m/s e uma velocidade de rotação variando de 300 a 700 RPM, com acréscimo de 100 RPM. Houve concordância entre as simulações e os dados experimentais, estabelecendo que a faixa operacional eficaz deste rotor está entre 4.5 e 6 m/s. Os resultados, consistentes com estudos anteriores, revelam padrões de autorotação eficientes, contribuindo significativamente para a compreensão dos princípios aerodinâmicos subjacentes. Nessas condições, a turbina bioinspirada prosposta tem para um TSR = 5, entre com Ω = 300 – 500 RPM, $C_{P,máx} \approx 0.54$, enquanto a referência apresentou um $C_{P,máx} \approx 0.55$, com TSR = 6, cerca de 460 RPM, no software Qblade®, e $C_{P,máx} \approx 0.55$, com TSR = 8, cerca de 600 RPM no Ansys Fluent®.Além disso, foi construído um comparativo entre a pá bioinspirada desenvolvida neste estudo e outras pás bioinspiradas existentes. Essas análises detalhadas oferecem uma base sólida para futuras inovações em turbinas eólicas, fornecendo informações cruciais sobre o desempenho relativo das pás, suas características de início de rotação e torques associados. Todos os experimentos foram realizados no LAEX (Laboratório de Aerodinâmica Experimental) do Centro de Pesquisas Aerodinâmicas Experimentais (CPAERO) na Universidade Federal de Uberlândia (UFU).

Palavra-chave: *Aerodinâmica experimental; CFD; Turbina Eólica de Pequeno Porte, Bioinspirado, Samarídeo, Cerrado.*

ABSTRACT

The increasing demand for sustainable energy sources has propelled intensive research in renewable technologies, with wind energy emerging as a critical player in the green energy landscape. In this context, optimizing wind turbine blades plays a crucial role in the overall efficiency of wind energy generation systems. Pursuing more efficient and innovative designs has led to applying bioinspired approaches, incorporating natural principles to enhance aerodynamic performance. This dissertation encompasses a novel investigation into the aerodynamic properties of Cerrado samara, focusing on autorotation behavior, flow patterns, and free-fall velocities. Experimental analysis in a wind tunnel was complemented by Reynolds-Averaged Navier-Stokes (RANS) simulations for the full-scale samara, a conventional reference blade based on SG6043 airfoils without angle of attack, and a bioinspired blade with reduced solidity. QBlade simulations were performed for the reference blade. The ANSYS Fluent® software, using the Moving Frame Reference (MRF) model, was employed to model airflow around the turbine. Simulations covered a wind speed range of 4 to 12 m/s, with increments of 2 m/s, and a rotation speed ranging from 300 to 700 RPM, with increments of 100 RPM. There was an agreement between simulations and experimental data, establishing the effective operational range of this rotor between 4.5 and 6 m/s. Consistent with previous studies, results reveal efficient autorotation patterns, significantly contributing to understanding underlying aerodynamic principles. Under these conditions, the proposed bioinspired turbine achieves a TSR of 5, with Ω ranging from 300 to 500 RPM, yielding CP,max of approximately 0.54. In comparison, the reference blade demonstrated a CP max of roughly 0.55 at TSR 6, around 460 RPM, using QBlade®, and a $C_{P,max}$ of approximately 0.55 at TSR 8, around 600 RPM, using Ansys Fluent®. A comparative analysis was also conducted between the bioinspired blade developed in this study and existing bioinspired blades. These detailed analyses provide a solid foundation for future innovations in wind turbines, offering crucial insights into the relative performance of blades, their initiation characteristics, and associated torques. All experiments were conducted at the LAEX (Laboratório de Aerodinâmica Experimental) of the Centro de Pesquisas Aerodinâmicas Experimentais (CPAERO) at the Universidade Federal de Uberlândia (UFU).

Keywords: *Aerodynamic; CFD; Small Wind Turbine, Bioinspired, Samarid, Cerrado.*

LIST OF FIGURES

LIST OF TABLES

LIST OF SYMBOLS

ABEEólica	Associação Brasileira de Energia Eólica
BEM	Blade Element Momentum
CFD	Computational Fluid Dynamics
CCPIU	Clube Caça e Pesca Itororó de Uberlândia
CPAERO	Centro de Pesquisas Aerodinâmicas Experimentais
FAPEMIG	Fundação de Amparo à Pesquisa de Minas Gerais
FPS	Frames per second
DNS	Direct Numerical Simulation
GWEC	Global Wind Energy Council's
HAWT	Horizontal Axis Wind Turbine
InBio	Instituto de Biologia
LES	Large Eddy Simulation
LMEst	Laboratório de Mecânica de Estruturas
MRF	Moving Reference Frame
NREL	National Renewable Energy Laboratory
RANS	Reynolds-averaged Navier–Stokes
RBM	Rigid Body Motion
RMS	Root Mean Square
RPM	Revolutions per minute
TSR	Tip Speed Ratio
UFU	Universidade Federal de Uberlândia
VAWT	Vertical Axis Wind Turbine

Summary

CHAPTER 1

1 INTRODUCTION

The need for sustainable energy solutions to meet modern demands and combat climate change has fostered a surge in renewable energy demand worldwide. Green energy shows great promise in balancing energy provision and environmental preservation. Wind energy is a viable option among renewable sources due to its abundant availability and electricity-generating potential. However, maximizing wind utilization and optimizing wind turbine performance have been areas of intense research to achieve efficiency.

The Global Wind Energy Council's (GWEC) latest report predicts that wind energy will surpass the monumental 1 TW milestone by 2023 and the 2 TW mark by 2030, marking a decade of incredible progress. According to the International Energy Agency, over 98 % of electricity will come from renewable sources between 2022 and 2025. GWEC anticipates an additional 680 GW of wind capacity will be installed globally between 2023 and 2027, including 130 GW of offshore capacity (GWEC, 2023).
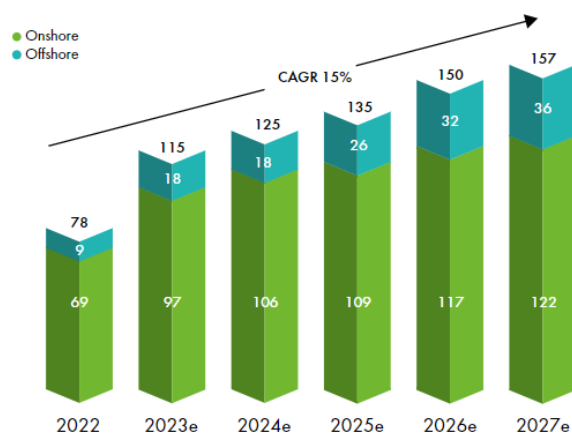
*Compounded annual growth rate (CAGR)

Figure 1. The outlook for new installations 2022–2026 (GW) (*New installations outlook 2022-2027*) (GWEC, 2023).

The use of wind energy is rapidly expanding across many nations, including Brazil. The president of the Brazilian Wind Energy – Associação Brasileira de Energia Eólica (ABEEólica) revealed in a recent report that the industry has achieved an installed capacity of 25.6 GW by 2022, solidifying wind energy's position as one of Brazil's most resilient power generation sectors. Brazil's offshore wind energy development holds excellent promise alongside the consistent growth of onshore wind energy. The concerns mentioned above are often associated with large

wind farms. However, they are just as significant for smaller-scale projects such as household installations and small wind turbines operating in less favorable conditions, such as the atmospheric boundary layer or urban influence.

In the wake of COVID-19, the trend toward utilizing small-scale renewable energy sources has gained significant momentum. This has resulted in small wind turbines being grouped in arrays on small farms and integrated with photovoltaic and energy storage systems. Moreover, certain countries have enacted policies restricting the construction of megawatt-sized land-based wind turbines, further enhancing the appeal of small-scale installations as a source of sustainable energy (Wiklak et al., 2022).

Enhancing the efficiency of wind turbines is necessary to meet the increasing global demand for renewable energy. Consequently, researchers have conducted numerous studies to analyze and improve the processes of capturing, converting, and storing the kinetic energy of wind. A critical focus of research has been on modifying the design of turbine blades (Habali & Saleh, 2000; Ankour et al., 2018). By optimizing the aerodynamics of the blades, researchers can increase turbine efficiency, resulting in better conversion of wind energy into electrical power (Maalawi & Khalil, 2018).

In addition to advancements in aerodynamic engineering, an emerging concept has garnered interest in wind energy: biomimicry. This concept is related to nature's ability to inspire efficient and sustainable solutions to technological challenges. Through the observation and study of phenomena present in the wings of birds (Fig. 2, Ikeda et al., 2018; Bodling et al., 2017; Top, 2022; Zeisberger, 2021; Kolvart, 2021; Walsum, 2013; Bodling et al., 2017), flight of insects (Cognet et al., 2017; Kumar & Pendyala, 2022), fish (Zari, 2007; Isaac & Swanson, 2011; Swanson & Isaac, 2011; Chowdhury et al., 2019), whales (Fish & Lauder, 2006; Fish et al., 2011), and shells (Hadi et al., 2021; Xia et al., 2023).

Inspired by studies of seeds that rotate automatically as they fall, providing favorable performance characteristics compared to current wind turbines, some researchers (Castañeda, 2010; Holden; Caley; Turner, 2015; Chu, 2016; Correa-Álvarez et al., 2016; Chu & Chong, 2017; Seidel et al., 2017; Chu & Chong, 2018; Chu, 2018; Herrera et al., 2019; Chu, 2020; Chu; Lam; Peng; 2021) have explored innovative strategies to optimize blade design, making them more efficient in capturing and harnessing wind energy.

In this context, the ability of the seed to convert kinetic energy into lift is akin to the purpose of a wind turbine, which seeks to transform the kinetic energy of moving fluid (wind) into electricity, even approaching the theoretical limit with which energy can be extracted from the air (Holden et al., 2015). These seeds have developed aerodynamic adaptations over evolution to optimize their dispersal capacity and ensure efficient propagation of their species (Lentink et al., 2009; Aydin et al., 2023). By exploring the concept of biomimicry in the context of wind energy, valuable insights can be gained for enhancing the efficiency of wind turbines and developing more advanced technologies.
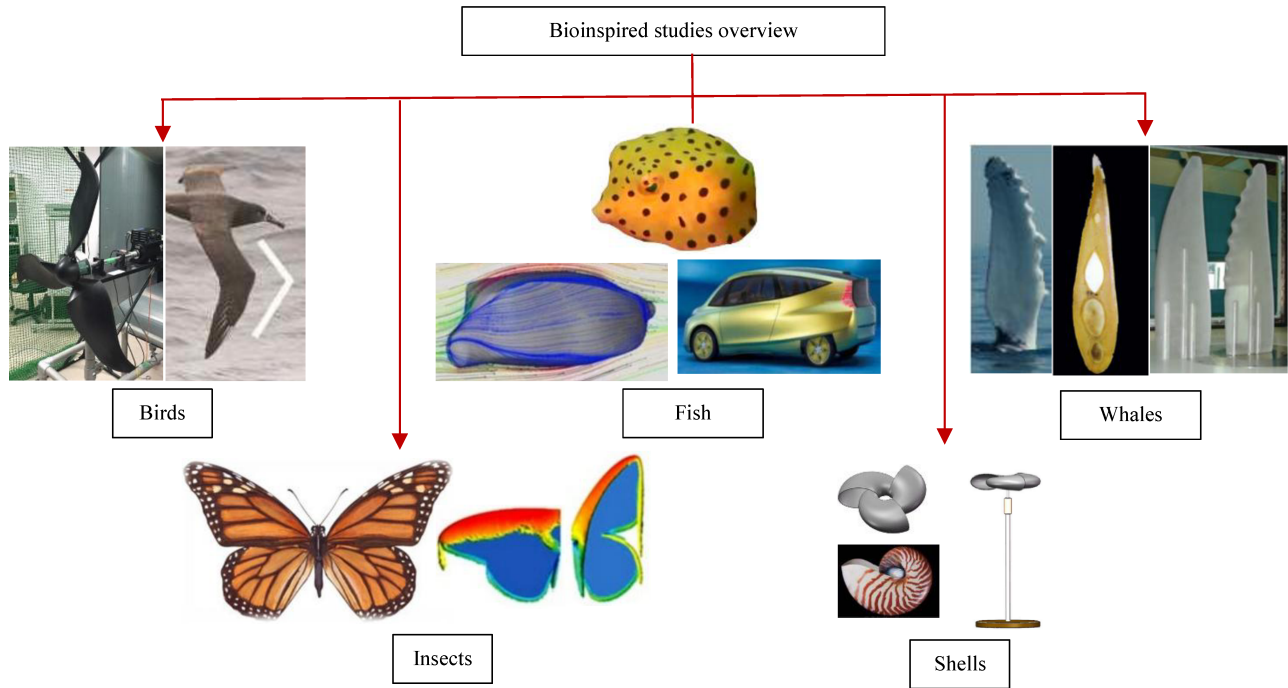
Figure 2. (a) Prototype rotor with bioinspired-flexion blade and flexed wings of flying birds in flight (b) Daimle Crysler bionic car inspired by the box fish and tree growth patterns (Zari, 2007) (c) Flippers on humpback whale showing scalloped pattern of tubercles (left), and flipper cross-section (center) The models with and without tubercles were machined from clear polycarbonate, based on a symmetrical NACA 0020 foil section. (right) (Fish & Lauder, 2006; Fish et al., 2011) (d) Monarch Butterfly "Danaus plexippus", Monarch Butterfly "Danaus plexippus" (Kumar & Pendyala, 2022) (e) Nautilus wind turbine model (Xia et al., 2023).

This study presents a novel approach to improving the efficiency of wind turbines by drawing inspiration from the morphology of anemochore's seed. The study uses experimental and numerical methods to understand better airflow patterns and aerodynamic parameters involved in the biomimetic blade design. To accomplish this, a laser scanning method was utilized to obtain profiles/airfoils along the wingspan of seeds. The resulting data was then used to derive a complete 3D turbine blade, which was prototyped and tested on a bench under various flow velocities. The results are visually presented regarding power (P_{mec}), flow velocity ($u\infty$), power coefficient, and tip speed ratio and compared with baseline values. Notably, this work builds upon and expands the findings of "Experimental analysis of biomimetic blades for small wind generators" by Paiva (2021).

Furthermore, this study includes evaluating the analysis techniques employed to assess the aerodynamic efficiency of Horizontal Axis Wind Turbine (HAWT) blades. As detailed in prior literature, the analysis techniques encompass numerical and experimental approaches. Specifically, for numerical methods, this study delves into Computational Fluid Dynamics (CFD) methods to accurately predict HAWT blades' aerodynamic performance. Wind tunnel experiments are employed to analyze HAWT blade performance for experimental procedures. Figure 3 provides an overview of the analysis techniques examined in this study.
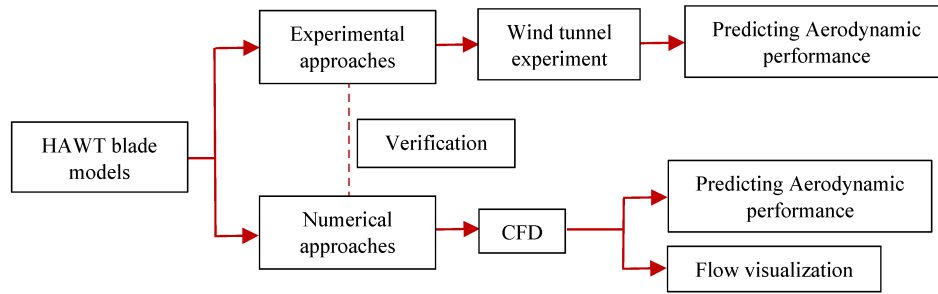
Figure 3. Summary of analysis methods for predicting and measuring aerodynamic performance of a HAWT blade.

This multidisciplinary approach aims to advance wind turbine blade design, enhance efficiency, and promote the sustainable development of renewable energies. Additionally, it seeks to introduce the concept of biomimicry as a promising approach to improving wind turbine performance, drawing inspiration from the morphology of tree seeds. The results obtained in this research could provide valuable insights for future innovations, paving the way for cleaner and more efficient energy generation.

1.1 RESEARCH OBJECTIVES

The focus of this study is to delve into the aerodynamic design and simulation of a three-bladed biomimetic HAWT rotor, taking inspiration from the winged geometry of anemochore's seeds, and compare them to a reference rotor created based on the blade element momentum theory. Thus, the objectives of this research include:

- Analyzing bioinspired wind turbine designs;
- Collecting seeds from the Cerrado biome dispersed by anemochory, studying their morphological parameters that influence their aerodynamics;
- Designing a bioinspired HAWT blade based on one of the chosen seeds;
- Designing a reference HAWT blade using the QBlade software;
- Conducting velocity profile surveys, static torque curves, and RPM measurements of the prototypes based on experimentally measured variables, aiming to contribute to the understanding of turbine performance during operation in free flow;
- Determining the performance of the developed HAWTs in various aspects, including energy extraction capability using a commonly employed steady-state CFD approach with moving components, namely the Moving Reference Frame (MRF);
- Comparing the performance predictions of the proposed biomimetic HAWT with a reference HAWT to deduce the strengths of the proposed biomimetic HAWT;
- Comparing the performance of the biomimetic HAWT with some turbines from the literature with a similar concept.

1.2 WORK STRUCTURE

In Chapter 2, the main equations of the Actuator Disk model, Blade Element Momentum Theory, and Blade Element Theory will be presented, along with an explanation of the general aerodynamics of airfoils, establishing the theoretical basis for subsequent analyses.

In Chapter 3, the aerodynamics of a self-rotating seed will be discussed in detail, utilizing the principles addressed in Chapter 2 to understand its aerodynamic behavior.

Chapter 4 will conduct a literature review focusing on studies related to bioinspired wind turbines or those that consider seeds as wind turbines. This review will contextualize the applications of the theories discussed in Chapters 2 and 3.

Chapter 5 will introduce the concept of wind turbine wakes, address turbulence models, convergence criteria, and techniques for simulating rotational motion in wind turbines, and lay the groundwork for analysis in Chapter 7.

Chapter 6 will detail the methodology adopted in this study, from seed collection and experimental identification of aerodynamic parameters to developing reference turbine blades using QBlade® software and parameters for CFD simulation.

In Chapter 7, the researchers will present and discuss the results obtained, covering the free-flight behavior of seeds, the rationale for seed selection, the development and final configuration of reference and bioinspired blades, wind tunnel experiments, CFD simulations of the samara and blades using the MRF approach. Finally, the researchers will conduct a comparative analysis of performance parameters between the blades of this study and some from the literature presented in Chapter 4.

Finally, in Chapter 8, the study's main conclusions will be discussed. The results obtained in the previous chapter will be summarized, identified trends and patterns highlighted, and future work suggested by knowledge gaps identified.

CHAPTER 2

2 THEORY APPLY TO WIND TURBINE

Various techniques can be utilized to evaluate the efficiency of wind turbines under constant conditions. The most widely recognized Betz and Glauert established approaches in their respective works (Betz, 1926; Glauert, 1926). This principle allows for estimating the performance characteristics of an annular section of an ideal wind turbine rotor. This section will explore the actuator disc and Blade Element Momentum (BEM) theories. The sizing calculations for this endeavor were based on the equations derived from Manwell et al. (2009) and Tong (2010). Only the primary equations essential to the thoroughness of this study will be presented.

2.1 ACTUATOR DISK MODEL

The so-called actuator disc model, initially introduced by Froude (1889) as an extension of Rankine's work (1865), allows for characterizing the fundamental flow phenomena expected in HAWT operation. This enables the determination of information regarding flow rate, showing that the upstream and downstream velocities of the rotor differ from the velocity in the rotor plane, in addition to the possibility of estimating the local power coefficient, considering a one-dimensional model of an ideal rotor (assuming infinite blades, no hub, and no axial thickness), as Hansen (2008) conducted.

In this model, the turbine is simplified as a one-dimensional actuator disc, which creates a pressure discontinuity in the fluid flowing through it and extracts energy from the flow (Zhao et al., 2019; Dixon; Hall, 2010). Thus, only the momentum exchange between the flow and the disc in the axial direction of the disc is analyzed (De Lellis et al., 2018). Accordingly, the rotor is modeled through a permeable actuator disc, which reduces the upstream velocity (V_0) to a value (u) at the rotor and (u_1) in the wake (Fig. 4). Assuming no compressibility effects due to the deceleration induced by the kinetic energy extraction by the rotor, the application of mass conservation implies a divergence of streamlines. The disc loading is obtained from a discontinuous pressure drop over the rotor. The Bernoulli equation can be applied upstream and downstream of the rotor position to relate pressure and velocity evolutions.

The turbine can be identified at the center of Fig. 4, which presents the control volume, the air inflow and outflow, and their respective velocity symbols in specific enumerated regions.
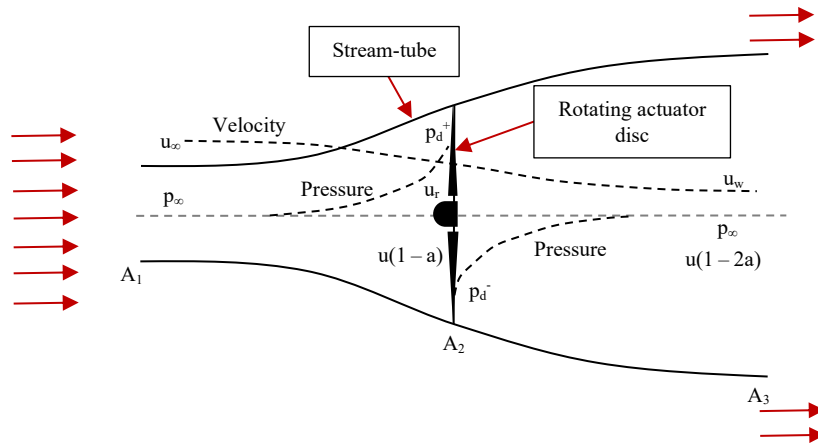
Figure 4. Wind flow through a turbine in an idealized control volume (Adapted from Wang & Alden, 2016).

Thus, Fig. 4 presents the parameters necessary for the wake effect. The subscripted values indicate the values at the identified cross-sections by the numbers. Considering that the angular velocity imparted to the flow stream, ω, is significantly smaller than the angular velocity, Ω, of the wind turbine rotor. We can assume that the pressure in the far wake is equal to that in the free stream (Wilson, 1976). The subsequent analysis uses an annular stream tube with a radius r and thickness dr, resulting in a cross-sectional area of $2\pi r dr$. Pressure, wake rotation, and induction factors are considered functions of radius.

In traditional BEM, the basic assumptions made are (Gazon, 2017; Snel, 2003; De Lellis et al., 2018; Zhao et al., 2019):

- Infinite-bladed rotor;
- No wake rotation;
- No drag effects;
- The flow is one-dimensional, irrotational, incompressible, and steady-state;
- The flow is unobstructed upstream and downstream of the rotor plane;
- The aerodynamic thrust is uniform over the entire rotor disc area.

These assumptions are known to be incorrect, but they reduce the complexity of the problem by an order of magnitude. Thus, they allow for the calculation of the force, combined with structural dynamics, in a computationally efficient manner, enabling the model to be used in design iterations and various calculations required for certification (SNEL, 2003).

Furthermore, the current model cannot correlate the rotor's geometry and performance, making it unsuitable for optimizing the blade to attain maximum performance. Betz's theory can be extended to incorporate angular momentum transfers between the rotor and the wind to overcome this deficiency. These transfers are directly related to the torque generated by the blades, which transfers significant amounts of angular momentum to the downstream wind through the rotation of the blades, as illustrated in Figure 5. As Maxwell et al. (2009) discussed, in a rotating wind turbine rotor, the flow behind the rotor rotates in the opposite direction due to the reaction to the torque exerted by the flow on the rotor.
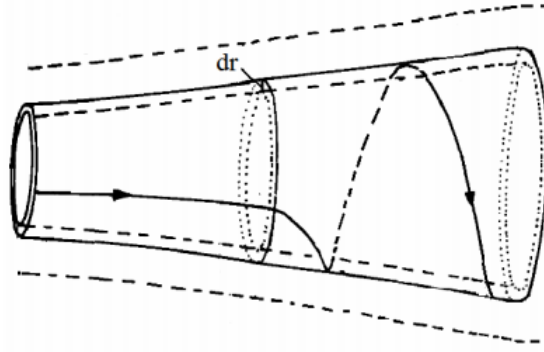
Figure 5. Flow tube model of the wake behind a rotating wind turbine blade (Manwell et al., 2009).

The wake rotation diminishes the wind generator's power output, primarily through kinetic energy transfer from the rotor to the rotational kinetic energy of the wind downstream of the turbine. Typically, the wind's angular momentum downstream of the rotor, and thus the wake rotation, will be more significant the more torque the blades exhibit. Consequently, turbines with low rotational speed and high torque experience fewer energy losses than those with high rotational speed and low torque.

As the turbine blades partially intercept the airflow, they capture energy from the wind, resulting in a decrease in velocity within the turbine rotor (or disc) and in the region behind it, known as the turbine wake. This reduction in flow implies an increase in the air passage area inside the turbine and the wake, as illustrated in the figure. From the assumption that the continuity of velocity through the disk exists, the velocities at sections 2 and 3 are equal to the velocity at the rotor:

$$u_2 = u_3 = u_R \tag{2.1}$$

For steady-state flow, the air mass flow rate through the disk can be written as:

$$\dot{m} = \rho.A.u_R \tag{2.2}$$

According to Biadgo and Aynekulu (2017), by applying the law of conservation of linear momentum to a control volume encompassing the entire system, the resultant force can be determined within that control volume. This force is equal and opposite to the thrust, representing the force exerted by the wind on the wind turbine. Therefore, according to the law of conservation of linear momentum for a one-dimensional, incompressible, and steady flow, the thrust is equal and opposite to the change in air momentum:

$$T = -\dot{m}(u_\infty - u_w) \tag{2.3}$$

Since no work is performed on either side of the turbine rotor, we can apply Bernoulli's equation to both control volumes on each side of the individual rotor. Therefore, we can use it between sections 1 and 2, representing the free flow and the windward side of the rotor, and between sections 3 and 4, representing the windward side of the rotor and the region far from the rotor.

$$p_0 + \frac{1}{2}.\rho.u_\infty{}^2 = p_u + \frac{1}{2}.\rho.u_R{}^2 \tag{2.4}$$

$$p_d + \frac{1}{2}.\rho.u_R{}^2 = p_0 + \frac{1}{2}.\rho.u_w{}^2 \tag{2.5}$$

The thrust, T, can also be expressed as the net sum of forces on each side of the actuator disc:

$$T = A.p' \tag{2.6}$$

where,

$$p' = (p_u + p_d) \tag{2.7}$$

Using Eqs. (2.4), (2.5), and the pressure decreases, you can find:

$$p' = \frac{1}{2}.(u_\infty{}^2 + u_w{}^2) \tag{2.8}$$

Substituting equation (2.8) into equation (2.6):

$$T = \frac{1}{2}.\rho.A(u_\infty{}^2 + u_w{}^2) \tag{2.9}$$

Equalizing the buoyancy values from Eq. (2.3) and substituting Eq. (2.2) for ṁ, and Eq. (2.9) for defining the rotor speed as:

$$u_R = \frac{u_\infty - u_w}{2} \tag{2.10}$$

Considering that an axial induction factor is a fractional decrease in wind velocity between the rotor plane and the free stream, therefore:

$$a = \frac{u_\infty - u_R}{u_\infty} \tag{2.11}$$

$$u_R = u_\infty(1 - a) \tag{2.12}$$

Using Eqs. (2.10) and (2.12), we obtain:

$$u_w = u_\infty(1 - 2a) \tag{2.13}$$

Biadgo and Aynekulu (2017) define velocity and pressure distribution, as shown in Fig. 4. Due to mass conservation, the diameter of the flow field increases as its velocity decreases, and there is a noticeable sharp drop in pressure at the rotor plane, contributing to the torque generated by the turbine's rotating blades.

The output power, P, can be defined as:

$$P = T.u_R \tag{2.14}$$

Using equation (2.9):

$$P = \frac{1}{2}\rho A(u_\infty{}^2 - u_w{}^2)u_R \tag{2.15}$$

or

$$P = \frac{1}{2}\rho A.u^3 \tag{2.16}$$

Finally, substituting u_R and u_w from equations (2.12) and (2.13) into equations (2.15):

$$P = 2\rho Aa(1 - a)^2 u_\infty{}^3 \tag{2.17}$$

The power coefficient is a measure that expresses the amount of power generated by a wind turbine and the available power in the wind. This is calculated as the ratio of generated power to the power available in the wind (Manwell et al., 2009). Wind turbines are now being manufactured in larger sizes to overcome the issue of unadjustable natural wind speeds. According to Custódio (2013), in an actual turbine, a portion of the maximum power will be extracted, resulting in the power coefficient C_P, represented in Eq. (2.18). P_{mec} is the power extracted from the turbine, P_{wind} is the power available in the wind, ρ is the air density, A is the area swept by the turbine rotor, and v is the wind speed in m/s. The energetic performance parameters of a wind turbine can be expressed in a dimensionless form, defined as:

$$C_P = \frac{P_{mec}}{P_{wind}} = \frac{T \cdot \omega}{0.5\rho u_\infty{}^3 A} \tag{2.18}$$

where C_P is the power coefficient, A is the swept area of the rotor (m^2), u_∞ is the free-stream flow velocity (m/s), ρ is the air density (kg/m^3), T is the torque in N.m, and ω is the angular velocity (rad/s).

By using Eqs. (2.16) and (2.17), C_P can be expressed as:

$$C_P = \frac{P_e}{P_t} = 4a(1-a)^2 \tag{2.19}$$

The axial thrust on the disk can be written as follows:

$$T = 2\rho Aa(1-a){u_\infty}^2 \tag{2.20}$$

Another necessary coefficient in the aerodynamic aspect of wind turbines is the torque coefficient, Eq. (2.21). This coefficient is related to the power coefficient, tip-speed ratio (TSR, λ), rotor solidity, and lift-to-drag ratio. The lower the torque, the higher the rotational speed of the rotor shaft, and the higher the rotational speed, the lower the solidity. Like the method used to obtain the power coefficient, the thrust coefficient can be described as the ratio of the thrust force to the dynamic force, as given by the following equation:

$$C_T = \frac{T}{0.5.\rho.{u_\infty}^2.A} \tag{2.21}$$

Similarly, to Eq. (2.19), the thrust coefficient, C_T, can be defined as the ratio of the thrust force to the dynamic force. Thus, the thrust coefficient can be written as:

$$C_T = 4a(1-a) \tag{2.22}$$

Thus, Manwell et al. (2010) give the relationship between the power and torque coefficients:

$$C_P = \lambda C_T \tag{2.23}$$

Axial induction factors, C_P, and C_T are standard metrics for simple wind turbine designs (Manwell et al., 2009). The values of $C_{P,max}$, and $C_{T,max}$ can be obtained by taking the derivative of Eq. (2.19) with respect to the axial induction factor and setting it equal to zero (Gasch & Twele, 2012). Figure 6 illustrates the behavior of these parameters. This derivation from one-dimensional momentum theory shows a more direct relationship between axial force and power ratios, resulting in:

$$C_{P,max} = \frac{16}{27} \cong 0.5926 \tag{2.24}$$

$$C_{T,max} = \frac{8}{9} \cong 0.8888 \tag{2.25}$$

when, $a = \frac{1}{3}$.
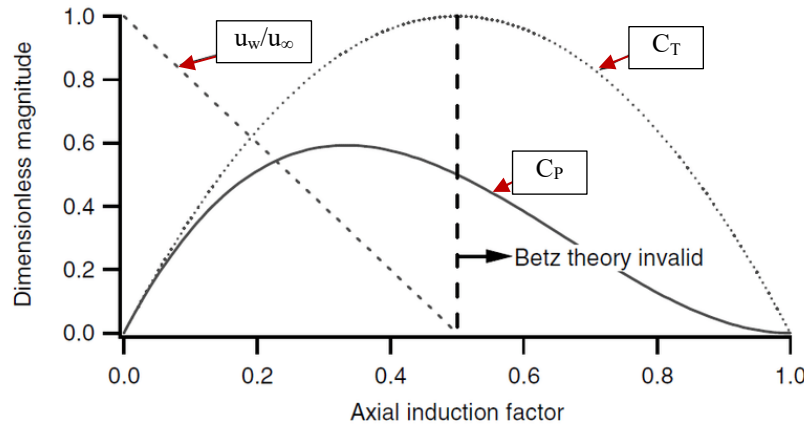
Figure 6. The variation of C_P e C_T with axial induction factor (Manwell et al., 2009).

Figure 6 displays a graph with the power and thrust coefficients for an ideal Betz turbine and the dimensionless downstream wind speed (Manwell et al., 2009). This idealized model is not applicable when the axial induction factor is less than 0.5. As the axial induction factor approaches and exceeds 0.5, complex flow patterns not represented in this simplified model led to thrust coefficients that can reach 2.0 (Wilson, 1976).

In other words, the downstream wind speed must decrease to approximately one-third of the upstream wind speed. According to this model, a turbine cannot extract more than 59.26 % of available wind energy within an area equivalent to its diameter. This limit, known as the Lanchester–Betz–Joukowsky limit or "Betz limit" (1926) (Ragheb & Ragheb, 2011; Hansen, 2015), represents the maximum percentage of energy that can be captured. It is important to note that this limit is optimistic, with more realistic models considering effects such as wake rotation leading to lower limits. For example, Glauert (1935) showed that the optimal efficiency of a wind turbine depends on the TSR, λ, the ratio between the speed of the turbine blade tips and the wind speed (Ragheb & Ragheb, 2011).

'In practice, according to Hartwanger and Horvat (2008), a wind turbine does not achieve higher levels of efficiency due to various factors, including:

- Rotation in the wake due to interaction with the moving rotor;
- Non-uniform pressure distribution in the turbine plane;
- Aerodynamic drag due to viscous effects;
- Energy loss due to vortex formation at the blade tips.

If we employ a moving control volume with the blade angular velocity, we can apply the energy equation at sections before and after the blades to derive an expression for the pressure difference across the blades (Glauert, 1935; Biadgo & Aynekulu, 2017). It is important to note that as the flow passes through the rotor disk, the angular velocity of the air relative to the blade

increases from Ω to $\Omega+\omega$. In contrast, the axial component of velocity remains constant. The results are as follows:

$$p_2 - p_3 = \rho\left(\Omega + \frac{1}{2}\omega\right)\omega r^2 \tag{2.26}$$

The resulting thrust on an annular element, dT, is:

$$dT = (p_2 - p_3)dA = \left[p_2 - p_3 = \rho\left(\Omega + \frac{1}{2}\omega\right)\omega r^2\right]2\pi r dr \tag{2.27}$$

An angular induction factor, a', is expressed as:

$$a' = \frac{\omega}{2\Omega} \tag{2.28}$$

where ω is the angular velocity of the incoming flow stream, and Ω is the angular velocity of the wind turbine.

The insertion of the effect studied in this section of the model implies that the induced wind speed at the rotor will be the vector sum of the standard component Ua and the angular component $r\Omega a'$. Introducing the angular induction factor into Eq. (2.29), we have:

$$dT = 4\pi\rho u_\infty{}^2 a(1-a)r dr \tag{2.29}$$

By equating the two expressions for thrust, we have:

$$\frac{a(1-a)}{a'(1-a')} = \frac{\Omega^2 r^2}{u_\infty{}^2} = \lambda_r^2 \tag{2.30}$$

where λ is the local tip speed ratio.

The TSR (λ) is defined as the ratio of the tangential speed of the rotor at its tip to the wind speed, and is given by:

$$\lambda = \frac{\Omega.R}{u_\infty} = \frac{V_{tan}}{u_\infty} \tag{2.31}$$

This result will be used later in the analysis, where V_{tan} is the tangential speed at the tips. Figure 7 shows the relationship between TSR and the coefficient of power of various rotors and the influence of the number of blades. In contrast, Figure 8 demonstrates the relationship of the torque coefficient with TSR. Based on the type of rotor and the desired goal for the turbine, a value for the overall speed ratio λ is established.
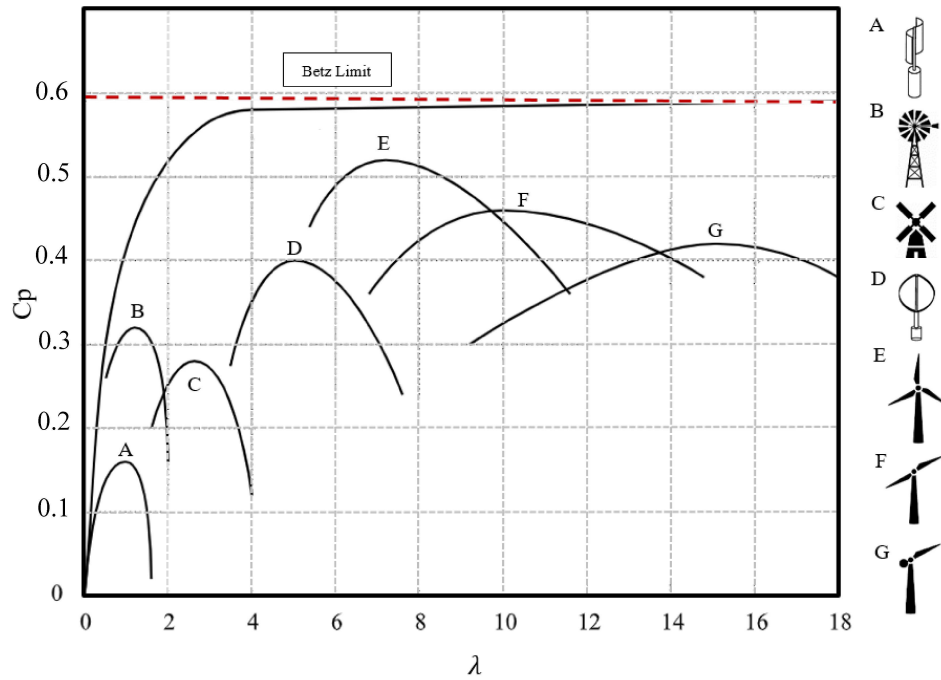
Figure 7. Blade tip speed ratio and power coefficient (Adapted from Hau, 2006).
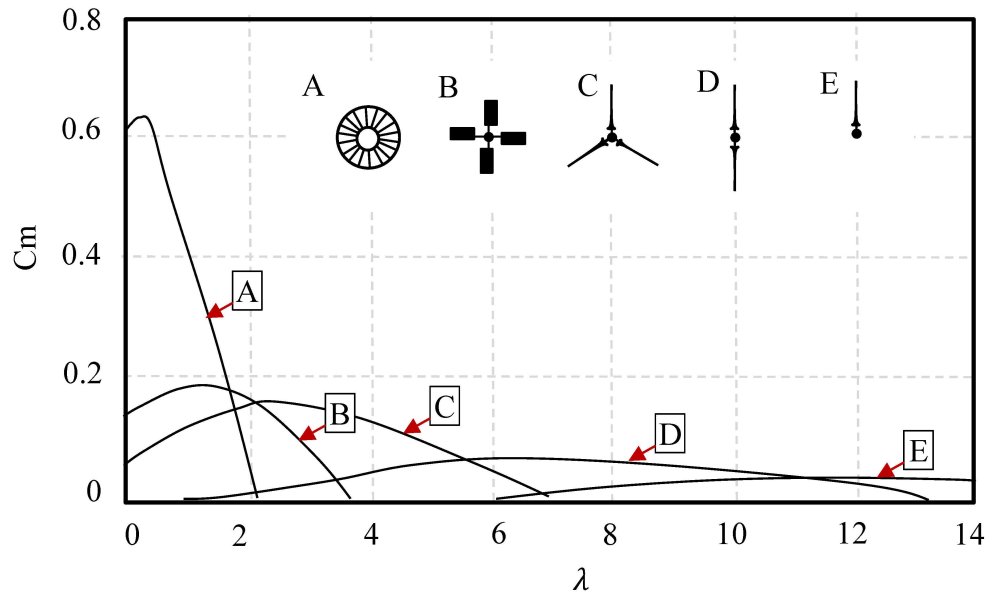
Figure 8. Blade tip speed ratio and moment coefficient (Adapted from Hau, 2006).

It is observed, from Figure 8, that the number of blades reduces λ and influences the power coefficient; furthermore, the fewer blades a turbine has, the faster the turbine rotor needs to rotate to extract maximum wind power and, consequently, the less torque. Pumping rotors have a low rotational speed, reducing the maximum speed ratio. Additionally, they exhibit a low power coefficient, and a high torque coefficient compared to rotors used for electrical power generation.

This is due to the high torque generated on the shaft, resulting in a high angular momentum in the wake and an increase in rotational kinetic energy, leading to less extractable energy. It is worth noting that the Savonius rotor has a simple design and is easy to construct, although it has inferior performance. Given this and knowing that fewer than three blades tend to present dynamic and structural problems (Manwell et al., 2009), the choice of three blades was made for this project.

An example of the typical dependence of wind turbine rotor power is the C_P coefficient in the TSR relationship, as illustrated in Figure 9 below for different pitch angles (Miller; Price; Snachez-Gasca, 2003). The maximum value of C_P, i.e., $C_{pmax} = 0.48$, is achieved for $\beta = 0°$ and for $\lambda = 6.75$ and decreases as β increases (Soni; Kumar; Kumar, 2014). This value of λ_{opt} results in the ideal efficiency point where the wind turbine captures maximum power from the wind (Molina & Mercado, 2011; Salles et al. 2011; Elbahi, 2017).

It is also possible to verify that the maximum power production point is difficult to achieve with increasing rotor speed, which means that the higher the rotor speed, the higher the wind speed required to achieve the maximum power coefficient. This can be explained by the following partial analysis of the impact of adjusting the synchronous rotation speed of the generator. The diagram below is plotted from extracting the power curve under rotor speeds of 1,250 RPM, 1,500 RPM, and 2,000 RPM, respectively (Zhou et al., 2017).
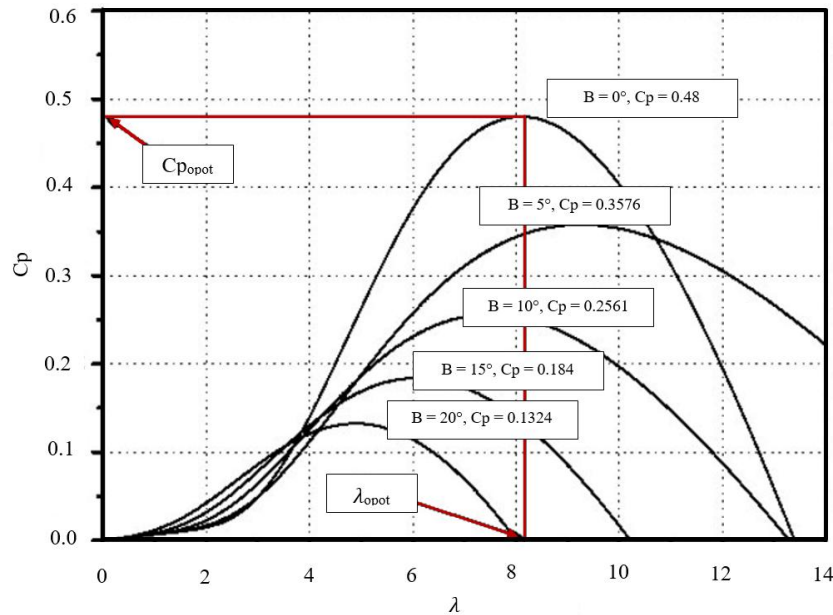
Figure 9. C_P vs. TSR for a typical wind turbine (Adapted from Rosyadi et al., 2012).

A range of $4 < \lambda < 10$ is generally recommended for electrical power production, as shown in Figure 8. Empirically, it is observed that faster rotors require less material in their blades and have smaller gearboxes; however, they require more advanced aerodynamic profiles (Manwell et al., 2009).

The graph in Figure 10 shows that the highest power for each wind speed is achieved when C_P is at its maximum. The generator should have a power characteristic that follows the maximum C_{pmax} to generate the most power. The mechanical power of the turbine is increased by both rotor and wind speed. When the turbine reaches its rated power, an increase in wind speed can cause the

turbine rotor to spin faster than its rated speed. When this happens, it is important to control the rotor speed and pitch angle properly, or the turbine blades may be damaged (Sarkar et al., 2020).
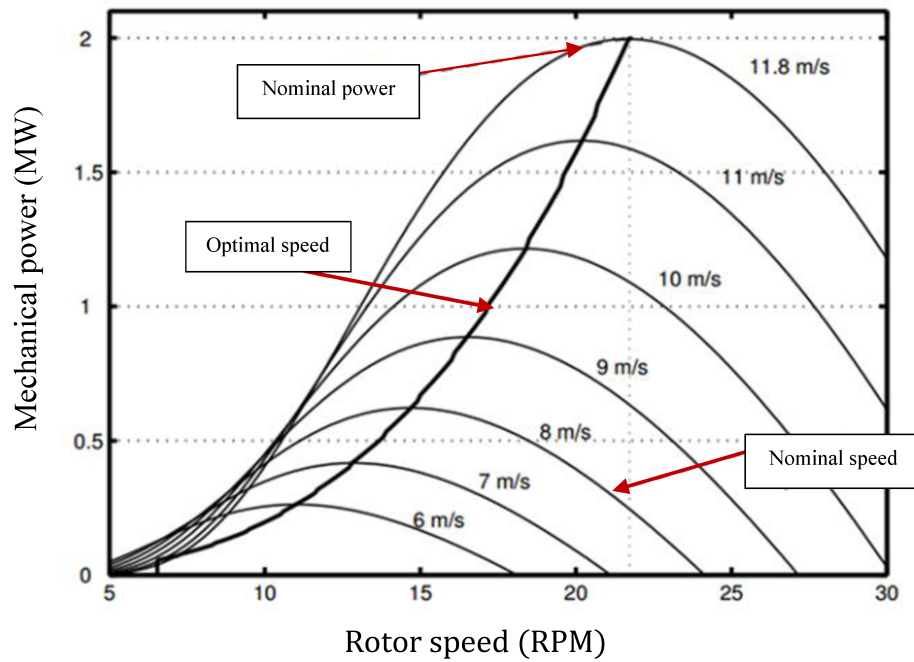
Figure 10. Wind turbine per unit torque versus speed characteristic (Adapted from Taveiros et al., 2013).

On the other hand, according to Sarkar et al. (2020), the operational region of the wind turbine has been divided into four areas, as depicted in Fig. 11. In Region I, wind speed ranges from 0 to the cut-in speed, where the output power is zero because the wind turbine does not operate. Region II indicates that wind speed ranges from initial to rated speed. In this region, the wind turbine starts operating as it reaches the cut-in speed. Region III shows that wind speed is between the rated and cut-out speeds, where the wind turbine can produce nominal wind power with a rated wind speed.
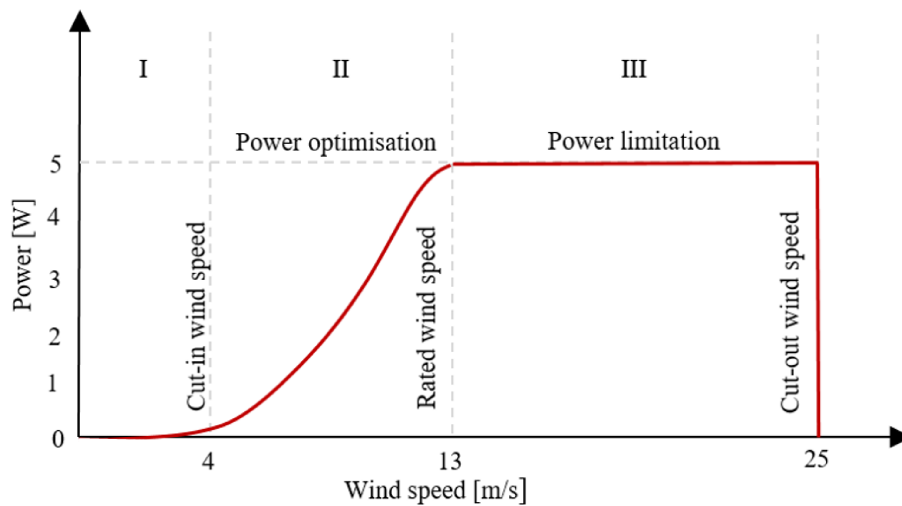
Figure 11. Power curve of a wind turbine (Adapted de Pinto, 2013).

2.2 THE BLADE ELEMENT THEORY (BET)

The moment theories presented in the previous sections consider the average axial and rotational velocity in the wake, allowing the determination of a blade's thrust and torque based on the decrease in the rate of fluid momentum. These theories establish an upper limit for the power coefficient of any blade, depending on the free-stream wind velocity and the extracted power. However, these theories have limitations when understanding the effect of rotor geometry, such as the blade airfoil section, its chord, and twist.

An alternative approach to analyzing blade behavior is the blade element theory. This analysis divides the blade into N sections (or elements). The aerodynamic force acting on each blade element can be estimated based on the appropriate characteristics of the airfoil of the same cross-sectional adopted for the blade elements, as shown in Fig. 12. In this analysis, it is assumed that the behavior of each element is not affected by the adjacent elements of the same blade. Thus, the force on the entire blade can be determined by summing the contributions of all elements along the blade (Rijis, 1990; Manwell et al., 2009).
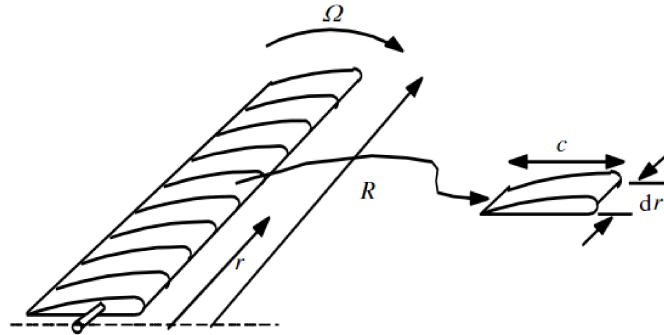
Figure 12. Schematic elements; c – airfoil chord length; dr – radial length of the element; r – radius; R – rotor radius; Ω - angular velocity of the rotor (Manwell et al., 2009).

The blade element theory follows the following premises (Ingram, 2011):
- There is no aerodynamic interaction between the elements, meaning others do not feel the actions experienced by one element.
- The lift and drag coefficients determine the forces applied to each blade element.

Figure 13 presents a diagram of the blade element developed at radius r, along with the velocities and forces acting on this element. The relative wind velocity is denoted by $u_\infty(1 - a)$ (the vector combination of the free-stream wind velocity, u_∞, and the induced axial velocity $-au_\infty$) and the wind velocity due to the rotation of the blade. This rotational component is the vector sum of the section blade velocity, Ωr, and the induced angular velocity $a'\Omega r$. Consequently, the velocity diagram in Fig. 12 represents the relative wind velocity.

The negative sign in the term $u_\infty(1 - a)$ is due to the deceleration of the flow as the air approaches the rotor. In contrast, the positive sign in the term $\Omega r(1 - a')$, as shown in Fig. 13, results from the airflow opposite to the blade rotation after the air particles hit the blades and thus provide torque.
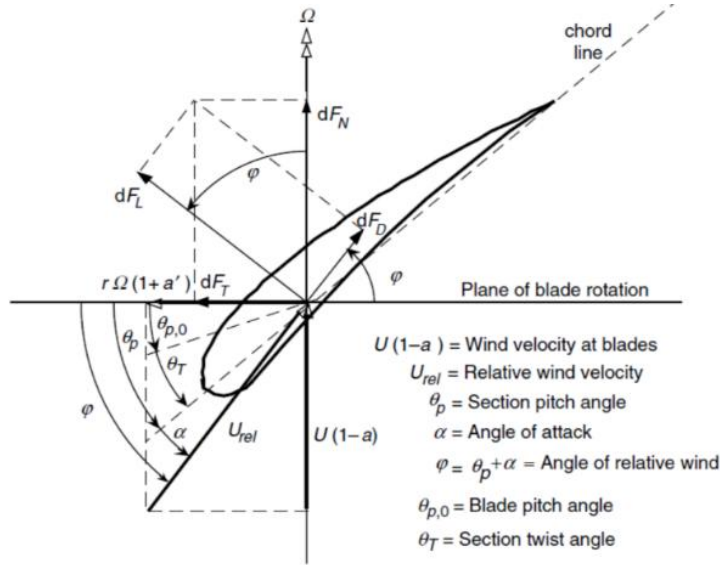
Figure 13. Blade geometry is used to analyze a horizontal axis wind turbine; for the definition of variables, see the text (Manwell et al., 2009).

From the above diagram, the following relationships can be obtained:

$$\varphi = \theta + \alpha \tag{2.32}$$

$$u_{rel} = \frac{u_\infty(1-a)}{sen(\varphi)} \tag{2.33}$$

$$\tan(\varphi) = \frac{u_\infty(1-a)}{\Omega r(1-a')} = \frac{(1-a)}{(1-a')\lambda_r} \tag{2.34}$$

$$dF_D = C_D \frac{1}{2}\rho u_{rel}{}^2 cdr \tag{2.35}$$

$$dF_L = C_L \frac{1}{2}\rho u_{rel}{}^2 cdr \tag{2.36}$$

$$dT = dF_L \cos(\varphi) + dF_D sen(\varphi) \tag{2.37}$$
$$dL = dF_L \sin(\varphi) - dF_D \cos(\varphi) \tag{2.38}$$

If the rotor has B number of blades, the total normal (thrust) and tangential force on the element at a distance r can be rearranged using Equations (2.37) and (2.38) with the use of Equations (2.33), (2.34), and (2.35) (Moriarty, 2005):

$$dT = B\frac{1}{2}\rho u_{rel}^2 (C_L \cos(\varphi) + C_D sen(\varphi))cdr \tag{2.39}$$

$$dL = B\frac{1}{2}\rho u_{rel}^2 (C_L \cos(\varphi) - C_D sen(\varphi))cdr \tag{2.40}$$

where φ is the flow angle, c is the airfoil's chord, and C_L and C_D are the lift and drag coefficients, respectively.

The elemental torque due to the tangential force's dL operating at a distance r from the center is given by:

$$dQ = rdL \tag{2.41}$$

Hence the elementary torque by inserting Eq. (2.40) into Eq. (2.41):

$$dQ = B\frac{1}{2}\rho u_{rel}^2 \,(C_L \, sen(\varphi) - C_D cos(\varphi))crdr \qquad (2.42)$$

Moreover, defining the solidity ratio, σ, as follows:

$$\sigma = \frac{Bc}{2\pi r} \qquad (2.43)$$

Additionally, a factor to be observed is solidity, which is the ratio between the blades' total area and the rotor's swept area. Small wind turbines with fewer rotor blades have lower solidity and use less material for the blades, resulting in less tower mass and lower production costs (Reinders et al., 2012). According to Pinto (2013), this aspect also affects turbine performance, where a high solidity results in low speed and high torque. In contrast, a low solidity results in high speed and low torque, and within a reasonable range, the turbine is independent of this parameter. Therefore, optimal solidity is achieved with three blades, as shown in Fig. 14.
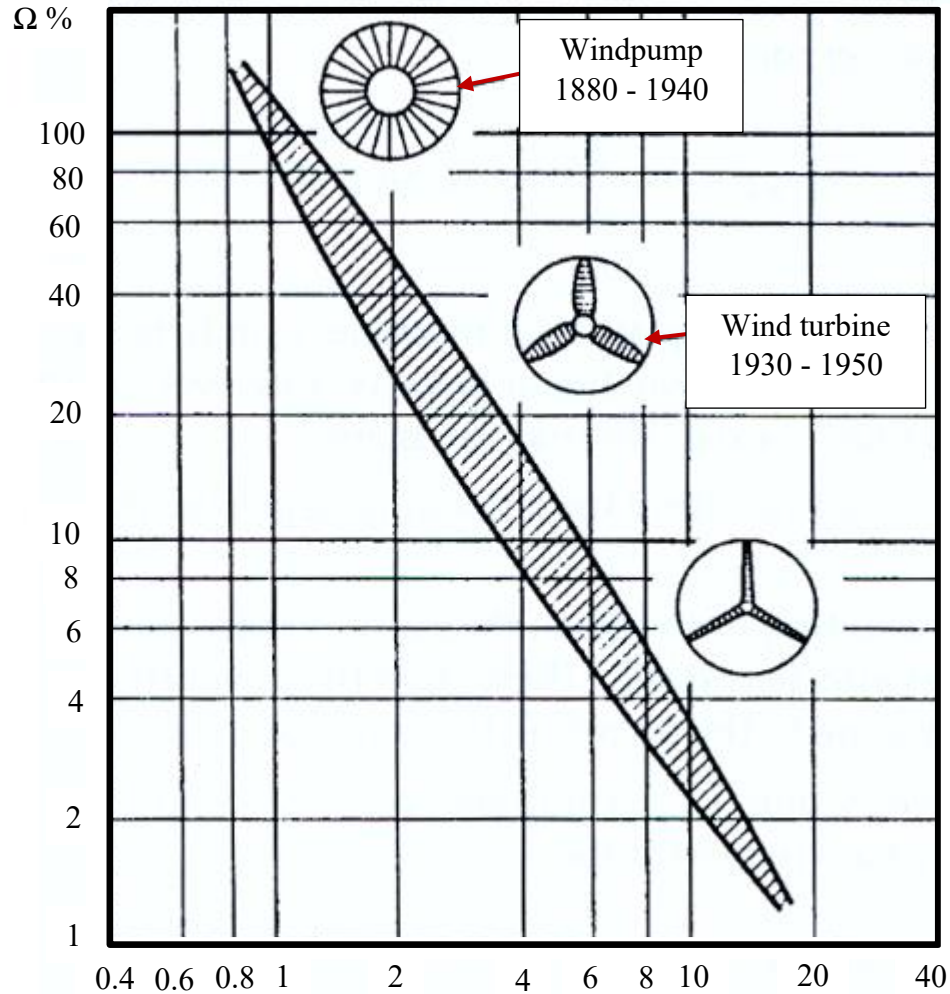
Figure 14. Comparison of the solidity of different wind rotors considering the tip speed ratio (Adapted from Ackermann, 2010).

Therefore, Equation (2.44) is used referring to Manwell et al. (2009) such that robustness is defined below:

$$S_R = \frac{1}{\pi R^2} \int_{R_h}^{R} C dr$$ (2.44)

The rotor speed, defined by the TSR, is crucial to its performance, as only one of its values provides maximum efficiency (Hau, 2013; Gasch & Twele, 2012; Hansen, 2017; Schmitz, 2020). This dimensionless parameter is closely related to the rotor's robustness, which varies depending on the size of the wind turbine rotor and its purpose (Gasch & Twele, 2012; Rosato, 2018).

Furthermore, due to the rotational principle of the wind turbine rotor, the flow over the blade surface is three-dimensional, with the root and tip regions strongly affected by vortices due to the complexity of the flows generated in these two regions (Wood, 2011; Branlard, 2011; Døssing; Madsen & Bak, 2012; Herráez et al., 2016). Resolving these issues can significantly improve blade productivity and minimize energy losses, where losses at just the blade tip can account for a nearly 10 % reduction in annual energy production (Branlard, 2011). On the other hand, the root region is characterized by higher solidity and pitch angle than the tip region, as this part of the blade is considered the most important contributor to ensuring the strength and stiffness of the blade structure and the resistance coefficient – system initialization at low wind speeds (Wood, 2011; Rosato, 2018).

However, even the roots of the rotor blades affect the improvement of wind turbine performance (Døssing et al., 2012). Due to these peculiarities, stalls are more likely to occur in the root region and propagate to the blade tips, causing a decrease in their performance. Thus, the early prevention of the expansion of this negative phenomenon remains a challenge, both in the flow direction and the blade extension direction.

Again, only the relevant and most important relationships are provided for the BEM theory. Details can be found in Manwell et al. (2009).

2.3 BLADE ELEMENT MOMENTUM (BEM)

The Blade Element Momentum (BEM), or Glauert Theory, is a model used to assess a turbine's performance, considering its mechanical and geometrical parameters and the characteristics of the interaction flow. This approach results from combining the Blade Element Theory and the Momentum Theory. The former concept was introduced by William Froude in 1878 to study the local behavior of turbines (Ledoux et al., 2020).

The results of these approaches can be combined into what is known as BEM, which is used to relate the blade shape to the rotor and its ability to extract energy from the wind. This approach assumes that the force on a blade element is solely responsible for the change in the

momentum of air passing through the annulus swept by the blade element. It is emphasized that this methodology assumes that the profiles consist of radial elements that do not interact with each other, and lift and drag can be obtained from two-dimensional data of aerodynamic profiles, as shown in Figure 15 (Alves, 2011; Fleck, 2017).

Figure 15 facilitates the visualization of the aerodynamic forces involved in the problem. The indicated forces can be decomposed and rewritten to have FN, the normal force, and FT, the tangential force to the blades' rotation plane.
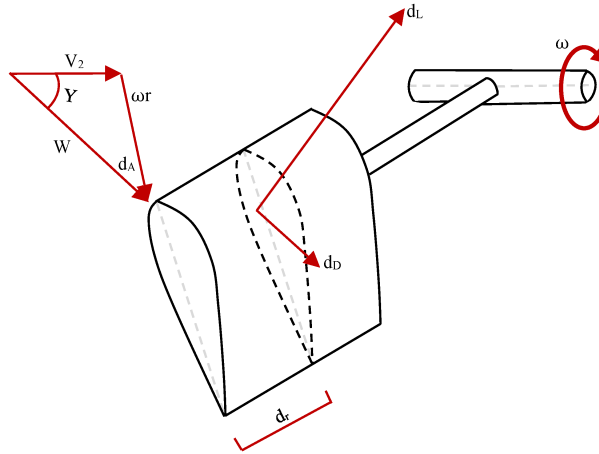
Figure 15. Representation of forces in the direction of the rope (Adapted from Hau, 2006).

According to Gasch and Twele (2011), applying this theory makes it possible to numerically model the blade's chord as a function of the radius, thus defining the local chord at each section r of the blade. In Eq. (2.45), the optimal Betz coefficient of power ($C_{pBetz} = 16/27 = 0.593$) is assigned.

$$C_r = \frac{1}{n} 2\pi R \frac{8}{9} \left(\frac{1}{C_L}\right) \frac{1}{\lambda \sqrt{\lambda^2 \left(r/R\right)^2 + 4/9}} \tag{2.45}$$

TSR (λ) concept states that the tip of a blade moves faster than its base, which requires the blade to be twisted along its length to maintain the correct angle. This twist angle is determined by the radius, local radius, angle of attack, and lambda, as shown in equation (2.46) according to Pinto (2013).

$$\beta(r) = \arctan\left(\frac{3r}{2R}\lambda\right) + \alpha_A \tag{2.46}$$

Therefore, the characteristics of the longitudinal profile of the blade are intrinsically related to the rotor diameter, the number of blades, the velocity at the blade tip, and the lift coefficient of the chosen airfoil. The twist angle, represented by (r), is the sum of the angle formed between the relative wind and the incident wind (γ) with the predetermined angle of attack, according to the

efficiency of the airfoil profile. Although the BEM theory is widely used in the design of optimized blades, it is expected to adjust the longitudinal profile of the blades after numerical modeling due to cost considerations, manufacturing processes, and resource optimization (Garré, 2015; Pires, 2010).

2.4 GENERAL AERODYNAMICS OF AN AIRFOIL

Airfoil designs, inspired by bird wings, were initially developed through trial and error and testing. Today, many airfoil profiles studied and developed by individuals or institutions have been standardized and published in catalogs. These catalogs include profile shapes, size ratios, and performance features. NACA, Göttingen, Wortmann, Althaus, Clark, and Zhukovsky are examples of well-known standard profile catalogs. The widely used NACA series can be derived using systematic equations (Aydin, 2023).

The graph in Figure 16 displays the primary parameters of an airfoil profile, including the mean camber line. This line connects the midpoints of the distance between the upper and lower surfaces of the airfoil. The chord, a straight line drawn between the leading and trailing edges, is also highlighted. The airfoil thickness can be determined by drawing a perpendicular line to the chord between the upper and lower surfaces. The camber line is the maximum perpendicular distance between the mean line and the chord.
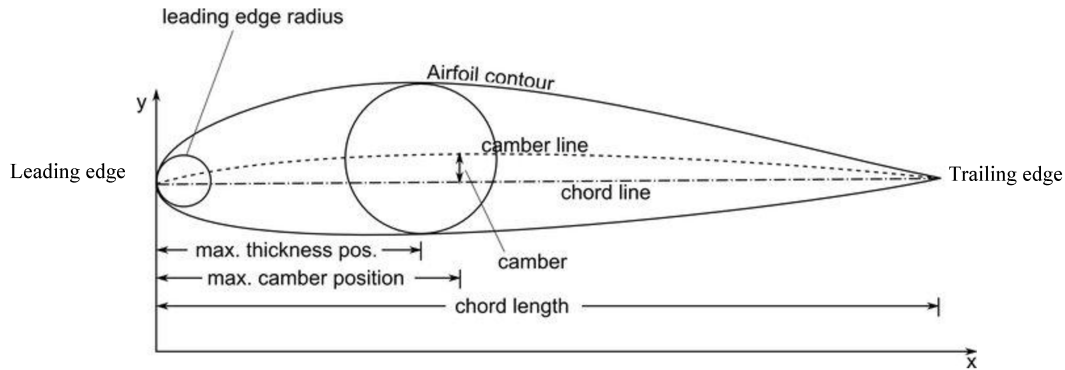
Figure 16. Parameter nomenclature of an aerodynamic profile (Adapted from Anderson, 2010).

The design of an HAWT blade depends on understanding the properties of airfoils. The most significant flow factor influencing airfoil behavior is viscosity, characterized by the Reynolds number of the airfoil/fluid combination. The Reynolds number Re is defined by:

$$\text{Re} = \frac{\rho \cdot u_{rel} \cdot L}{\mu} \tag{2.47}$$

where, *Re* is the Reynolds number (dimensionless); ρ is the fluid density (kg/m^3); is the relative velocity to the flow (m/s); μ is the dynamic viscosity of the fluid (Pa.s, N.s/m^2, kg/m.s); L is the characteristic linear dimension (m). This dimensionless coefficient is the primary factor characterizing the flow pattern, whether laminar or turbulent, and is defined as the ratio of the fluid's inertial force to its viscous force (Manwell et al., 2010).

Wind turbines are engineered to optimize their ability to produce energy by maximizing the ratio of lift to drag. This is done to extract as much power as possible while minimizing the stress placed on the structure. To enhance the efficiency of the structure, the blades of wind turbine rotors are designed with airfoils that decrease in thickness as they extend outward from the hub, with the thickest part of the blade being located at the hub and the thinnest part of the blade being located at the tips. Modern large-scale rotors typically operate in a Reynolds number range of 500,000 to 10 million, with predominantly laminar flow over the airfoil's upper surface (Guigèrre & Selig, 1997; Elizondo et al., 2009). Additionally, the accumulation of insects and dust on the airfoil profiles is avoided as surface roughness increases, and the extracted power can be reduced by up to 40 %. A stall control system is often implemented so that turbines can operate in more intense winds without damaging the generator due to increased power production (Manwell et al., 2009).

Another aspect that should be clarified is the nomenclature related to the flow passage over the airfoil. The flow of air over the airfoil creates a zone of high pressure on the lower surface (intrados) and a zone of low pressure on the upper surface (extrados) of the airfoil (Fig. 17). These zones generate an aerodynamic reaction that can be divided into lift (L) and pressure drag (D) in Cartesian coordinates.
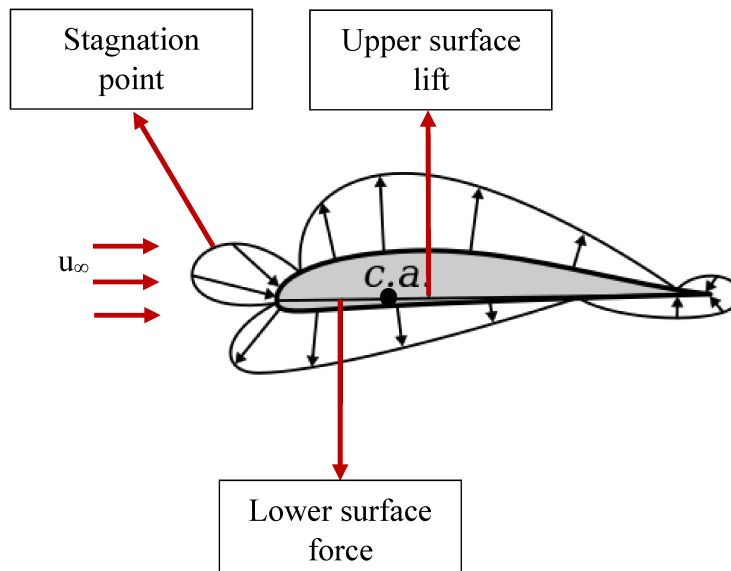
Figure 17. Positive and negative pressure profile around airfoil.

Additionally, the aerodynamic coefficients are closely related to Re. According to Corda (2017), wind turbines typically fall within the Reynolds number range between 10^5 and 10^6, which is considered a transitional flow. The region below $5 \cdot 10^5$ is introduced as the low Reynolds number flow regime, where small wind turbines typically operate (Giguère & Selig, 1997). Figure 18 illustrates the spectrum of airfoil applications with low Reynolds numbers.
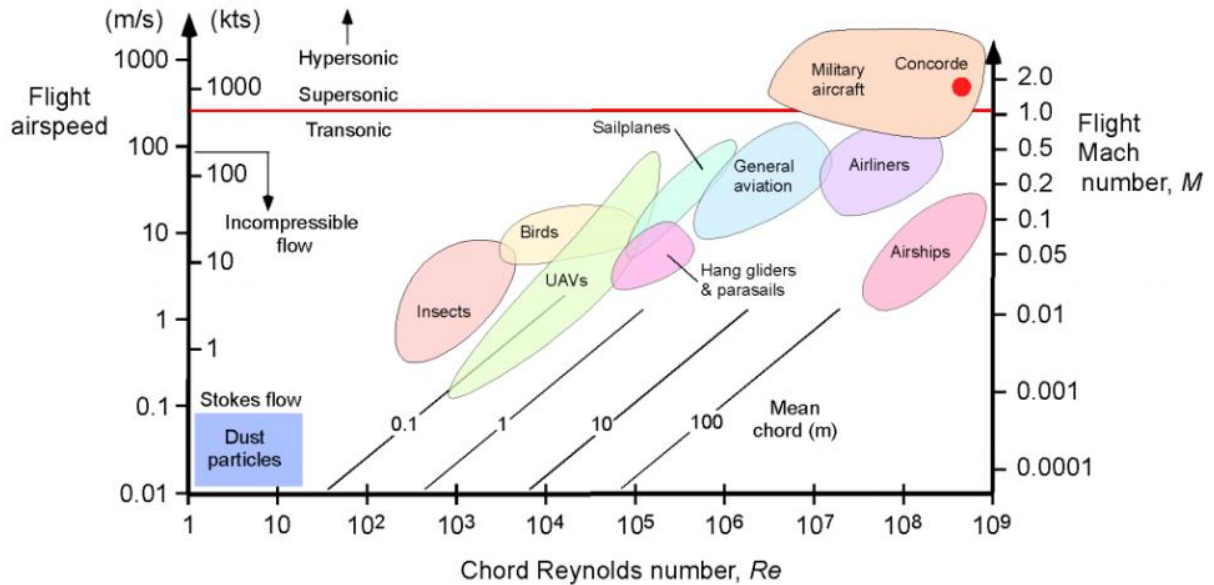
Figure 18. The range of typical applications of Reynolds numbers (Adapted from Lissaman, 1983).

Low Re airfoils are typically thinner than standard airfoils operating at higher Re (Giguère & Selig, 2008). The reduced thickness of these airfoils helps avoid higher suction pressures at the leading edge and adverse pressure gradients (APG) on the airfoil's upper surface, which can lead to flow separation (Lissaman, 1983). Conversely, the low APG helps to prevent flow separation and maintain laminar flow over the airfoil surface.

Selig and Giguère (1997) discuss the use of thin airfoils belonging to the SG60XX series family (SG6040-SG6043), particularly suitable for small wind turbine blades with C_L values in the range of $1.4 - 1.65$ para Re = $1e^5$ - $5e^6$. Thus, the SG6043 airfoil, depicted in Fig. 19, has been adopted as a suitable aerodynamic profile for wind power extraction, with experimental data on its aerodynamic parameters tabulated.
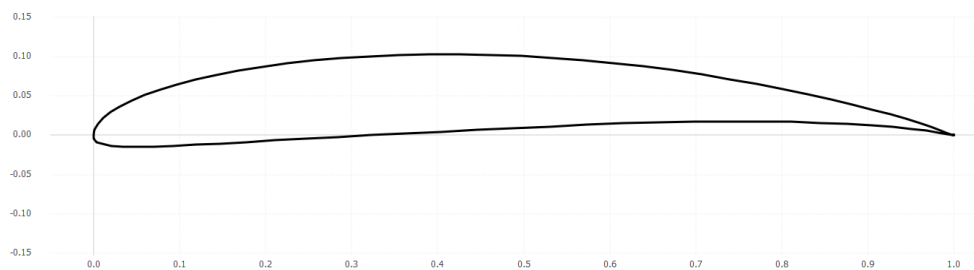
Figure 19. Representation of the SG6043 aerodynamic profile as a function of the chord.

While research on conventional airfoils continues, there is ongoing work on new designs inspired by biological wings and their applications in turbomachinery, including wind turbines (Aydin, 2023), which this research seeks to explore.

CHAPTER 3

3 MAPLE SEED AUTOROTATIONAL MECHANICS

Just like in the works of (Norberg, 1973; Azuma & Yasuda, 1989; Seter & Rosen, 1992; Rezgui et al., 2020; Holden et al., 2015; Bai & Chirarattananon, 2019; Rabault et al., 2019), this study compares the control volume of the maple seed to that of the actuator disk, which is a valid comparison for the energy extraction considerations here. However, it is also essential to understand the mechanics of seed dispersal by anemochory, known to be a common wind dispersal of diaspores, especially in dry and open conditions (Soons et al., 2004; Jara-Guerrero et al., 2011), as the case of the Brazilian Savanna, locally called the Cerrado, to which the object of this study belongs.

Seed dispersal by wind plays a significant role in the reproduction and preservation of plant species (Howe; Smallwood, 1982; Wilson, 1993), as dispersal is closely related to ecological scales of time and space. Some plants disperse seeds in long-distance flights to a suitable location, utilizing the opposite wind (Greene; Johnson, 1993; Minami & Azuma, 2003). Seeds from winged trees, such as maple and ash, spin to reduce the downward speed for long-distance wind dispersal: a phenomenon called autorotation flight of a winged seed. It is the primary mechanism behind the long-distance dispersal of many tree seeds (Augspurger, 1986). Autorotating seeds also have interesting applications in engineering, particularly in helicopter and flying vehicle design (Ulrich et al., 2006).

This set of complex characteristics indicates that the morphology of winged samaras, especially the wing shape, plays an essential role in fruit and seed dispersal, serving to increase the dispersal distance by reducing the descent speed after leaving the mother plant and keeping them in the air for a more extended period (Azuma & Yasuda, 1989; Minami & Azuma, 2003; Lentink, 2009; Varshney et al., 2011; Stevenson et al., 2015). Based on the morphology and aerodynamics of diaspores in the air, species are divided into seven categories, as shown in Tab. 1.

Many seeds have a single, flat wing, while some have multiple, curved wings that are folded (convex upwards) to reduce the outer cone or to make the wing tip horizontal. This is reasonable aerodynamically because the air loading is concentrated near the tip, and the heavy tip reduces the coning angle in flight and, therefore, increases the effective area of the disk ($S = \pi R^2$). At the same time, the base of the seed helps to provide a large drag area by which the horizontal force distribution is widely extended.

Table 1. Description of aerodynamic behavior of the groups of wind-dispersed diaspores and representative drawings of their morphology (Adapted from Augspurger, 1989; Liu et al., 2020).

Type	Aerodynamics in the air	Representative morphology
Floater	Floats downward in a vertical line	
Rolling autogyro	Rotates simultaneously around the seed's longitudinal axis and one end of the seed in a spiral	
Autogyro	Rotates tightly around the seed end of the seed	
Helicopter	Spins tightly around a vertical line	
Tumbler	Tumbles but not a consistent axis or rotates around a vertical line	
Undulator	Glides and undulates, but not with cumulative forward motion (not continuous glider)	
Tumbler/Unclassified	Complex and variable behavior within and between diaspores; closer to autogyro and undulator than rolling autogyro.	

Although the wing loading (mg/S_w) is higher in all rotating seeds than in gliding seeds, such as Alsomitra macrocarpa, whose wing loading is about 0.5 N/m^2 (Azuma & Okuno, 1987), the disc loading (mg/S) is lower than the wing loading of all gliding seeds, except for the seed of the Santalaceae tree. The wing is typically narrow in chord, and its aspect ratio [$AR = l^2/(S_w/p)$] is nearly equal to or slightly higher than the $AR = 4.0$ of the gliding seed. The low solidity ($\sigma = S_w/S$) ensures good performance (Azuma &Yasuda, 1989).

Thus, the flight kinematics of samara seeds in free fall have been the subject of various studies (Norberg, 1973; McCutchen, 1977; Azuma & Yasuda, 1989; Rosen & Seter, 1991; Yasuda & Azuma, 1997; Nathan et al., 2002; Minami & Azuma, 2003; Varshney et al., 2011; Arranz et al., 2018). At first glance, the spinning motion appears to be closely related to the autorotation of a wind turbine. The wing lifts due to the seed's falling speed exert a torque to rotate the seed around the vertical axis (Varshney et al., 2011), following a helical trajectory (Ulrich et al., 2010; Carré et al., 2022), around its center of mass, as shown, inscribing a cone around the axis of fall. The shape of the cone will vary depending on the aerodynamic characteristics of the seed. A seed with minimal lift properties inscribes a cone with steep sides, while a seed with strong lift properties inscribes a nearly flat cone (Storm, 2021).

According to Lentink et al. (2009), autorotating seeds can spin automatically because their center of gravity, determined by the position of the nut, is located at the base of the wing-shaped seed. This creates a delicate balance between gravity (seed weight), inertia, and aerodynamic forces (Skews, 1991; Smith, 1970). They can be divided into two categories according to the location of their center of gravity. When located ahead of the seed's aerodynamic center, the seed exhibits a gliding translation without rotation (Azuma & Okuno, 1987; Nathan et al., 2002; Nathan, 2006).

This occurs during autorotation because the linear and angular accelerations of the samara seed are zero. Therefore, in the constant vertical flight of an autorotating seed, the vertical component of the aerodynamic force and the weight of the seed are balanced (Norberg, 1973). In Fig. 20b, C_D and C_L represent the resulting centrifugal forces acting on both sides of the rotation

axis. The rotation axis approximately coincides with the center of mass of the seed, so the resulting centrifugal forces on both sides are equal.

According to Holden (2016), the lift force on the wing of the samara seed is shown by the vector diagram on the suction side of the wing surface in terms of W, which is the weight of the seed. This diagram shows that the vertical component of the lift force on the seed must be equal to the weight of the seed for there to be no linear acceleration. The cone angle of the seed, β, is the control mechanism to balance the weight and the vertical component of lift. The other distances in Fig. 20b represent the moment arms of the various forces around the rotation axis.

The cone angle gives the samara seed a lift advantage. If the Betz limit is considered, the samara seed can have a more extensive lift surface area for the same projected area normal to the flow direction by adding a cone angle (β). This angle is an optimized quantity, as a high cone angle close to 90° would result in a loss of lift compared to a rotor with the same normal swept area. In the studies conducted by Azuma and Yasuda (1989), the cone angle varies from 15° to 30° for samaras. The pitching angle (θ), the angle between the flight trajectory plane and the wing chord (Fig. 20b), has its positive direction defined as the direction of the nose down in the present study. The pitch angle of the samara seeds is generally slight, ranging from 1° to 2° (Azuma & Yasuda, 1989). The flight trajectory plane makes an angle of $\tan^{-1}(VD\cos\beta\ /y\Omega)$ with the resulting relative wind, which is the vector sum of the rotation speed components ($VH = y\Omega$) and the descent speed ($VD\cos\beta$). This angle is represented by φ in Figure 20b. Therefore, the local angle of attack (α) at the wing section is φ - θ.

(a)   (b)
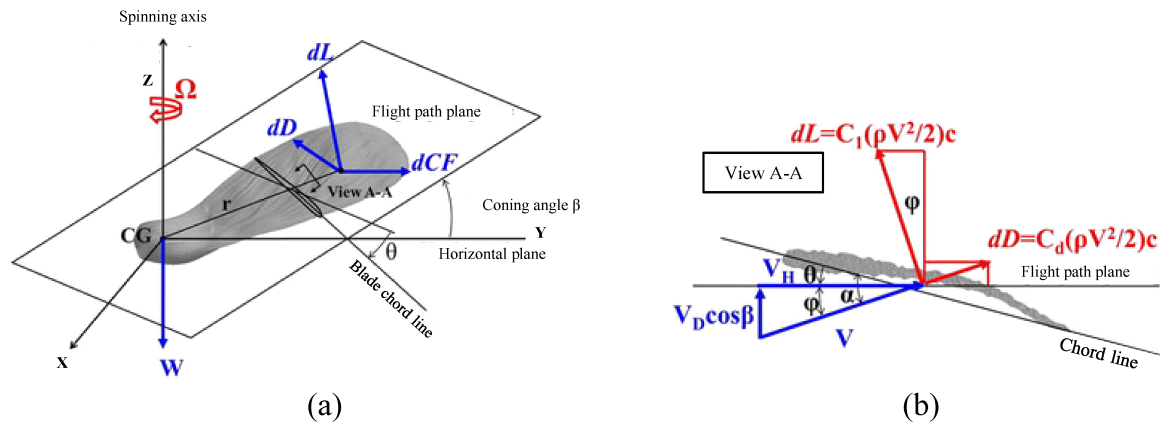
Figure 20. A diagram of the forces on the maple seed as it descends in autorotation (r – span coordinate; R – turn radius; W – weight of seed; dL – directional drag; dCF – centrifugal force acting on the section; β – coning angle; θ – pitch angle; Ω – spinning rate) (Adapted from Azuma & Yasuda, 1989).

The figure above shows that samara cross-sections are not smooth like typical aerodynamic airfoils. Instead, they are corrugated, featuring a concentration of ribs on the leading edge and a rough surface. These characteristics are also typical of cross-sections of insects and bird wings.

Depending on the species, this rotation is measured between 760 and 1430 RPM (or between 80 and 150 rad/s), with a vertical velocity of around 1 m/s (Norberg, 1973; Green, 1980) and a range of TSRs (1.5 < λ < 5.5) reported for samara seeds (Azuma & Yasuda, 1989). Additionally, like the Reynolds number, these parameters are the same magnitude as those observed for the operational conditions of centimeter-scale wind turbines at low wind speeds

(Gasnier et al., 2019). This is due to the rough surface caused by thick vascular bundles concentrated near the leading edge of the samara (Norberg, 1973), which enhance the aerodynamic performance of the seed at low Reynolds numbers (Re = $10^3 – 10^5$), consequently increasing the driving torque of the rotation axis. This range is much lower compared to helicopter rotors or propellers. This range is typical of birds or airplane models and, primarily, insect wings (Rosen & Seter, 1991; Yasuda & Azuma, 1997; Arranz et al., 2018; Green, 1980; Salcedo et al., 2013; Ortega-Jimenez; Kim; Dudley, 2019).

Autorotation is the primary mechanism behind their successful long-distance dispersion, although their wing loading maybe 450 % higher than that of sliding and spinning seeds, as found by D. Lentink (2009). This high aerodynamic performance may also have broad applications in engineering, particularly in helicopter design and new concepts for aerial vehicles (Siroshi, 2013). In this context, studying the flight mechanisms of samara seeds helps design efficient energy extraction rotor systems with stable outputs in unstable environments.

Thus, the slow descent and high lift come from the samara wing's ability to develop a flow mechanism known as the Leading-Edge Vortex (LEV) (Lentink et al., 2009; Birch & Dickinson, 2001), like the flow structures responsible for the high lift created by insect and bat wings (Aydin, 2023). The leading-edge vortex is a tornado-like vortex initiated from the tip of the samara wing and sits on its upper surface. This vortex generates more excellent circulation and consequently creates a region of low pressure above the wing, as shown in Fig. 21. Some researchers believe that this low pressure, in turn, results in 'additional lift' (Sane, 2003). Others suggest that the role of the LEV is to keep the flow attached to the wing, even at extreme angles of attack (α). Thus, an LEV has no stall, providing more excellent or enhanced lifting capabilities (Ford, 2013). This is especially useful for the samara, as its wing automatically rotates with high α angles, ranging from close to 75° near the root to around 20° at the tip (Seter & Rosen, 1992; Seter & Rosen, 2014).
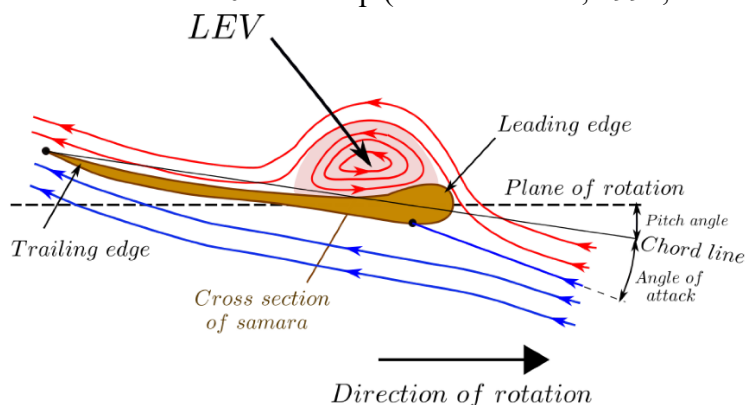
Figure 21. Two-dimensional schematics of the samara LEV with sectional streamlines (Adapted from Rezgui et al. 2020).

According to Norberg (1972), the aerodynamic force increases with the airfoil area and the square of the relative air speed. As the relative air speed of a samara increases distally, the blade area is better utilized away from the rotation center. Therefore, the blade chord should increase distally. On the other hand, there is the tip effect on the blade tip. The low pressure above the blade tends to be neutralized near the tip by the air moving around the tip from the high-pressure region below the blade, giving rise to a vortex at the blade tip accompanied by induced drag (Fig. 22). A blade with a broad tip may not be as practical as the blade's material could be better utilized to

increase the length or slightly enhance the overall breadth of the blade. This is perhaps why the blade's flat shape gradually narrows towards the tip.
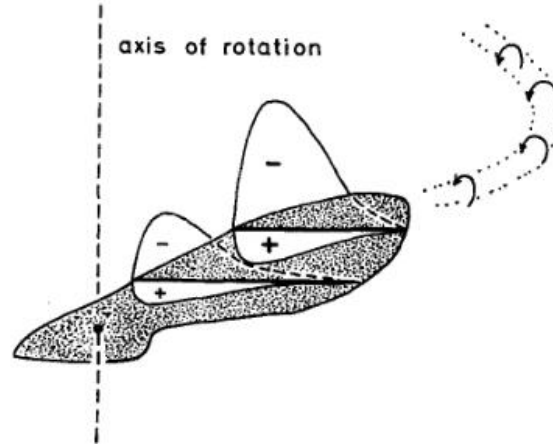
Figure 22. Diagram illustrating a trailing blade-tip vortex development by pressure equalization around the tip (Norberg, 1973).

Furthermore, Norberg (1973) establishes that a fluid column surrounds the descending maple seed relative to the still air. Figures 21a and 21b highlight the similarities in the analysis conducted for the actuator disk model (by Betz) and the control volume around a self-rotating samara. Thus, the BEM theory can be applied to calculate the induced velocity. According to this theory, the rotating wing is replaced by a disk. The radius of this disk is equal to the radius of rotation of the rotor tip. The details of the theory can be found in Glauert (1943). The induced flow through the disk is axisymmetric, meaning that the induced velocities are functions of the radial distance, r, from the disk's center.

According to Rosen and Seter (1991), if the sinking velocity of the disk is $(U_x)_{-\infty}$, then the axial velocity through the disk will be $(U_x)_\infty(1-a)$ (see Fig. 22b), where a is the induced axial velocity coefficient. As indicated above, "a" is generally a function of r. The fluid under the disk has no tangential (circumferential) velocity. After passing through the disk and applying an aerodynamic torque to the wing, the returning fluid (according to Newton's third law) develops rotation in the opposite direction. It is convenient to express this component as ωr (see Fig. 23a), where ω is the "angular velocity" of the fluid. It is still convenient to describe ω itself as:

$$\omega_r = 2\tilde{a}\Omega r \tag{3.1}$$

Ω is the angular velocity of the wing (see the positive direction in Fig. 23), while ã is the induced tangential velocity coefficient, which is generally a function of r. According to the moment theory, an annular element of the disk will be considered (see Fig. 23). This element has a radius of r and thickness of dr. The expressions for the vertical force dT, which is applied to the annular element by the fluid passing through it, are obtained by applying conservation laws of axial momentum, angular momentum, and energy. According to Glauert's general moment theory (1943), and analogous to Eq. (2.29):

$$dT = 4\pi\rho(U_x)_{-\infty}{}^2(1-a)aFrdr \tag{3.2}$$

<div align="center">(a)   (b)</div>
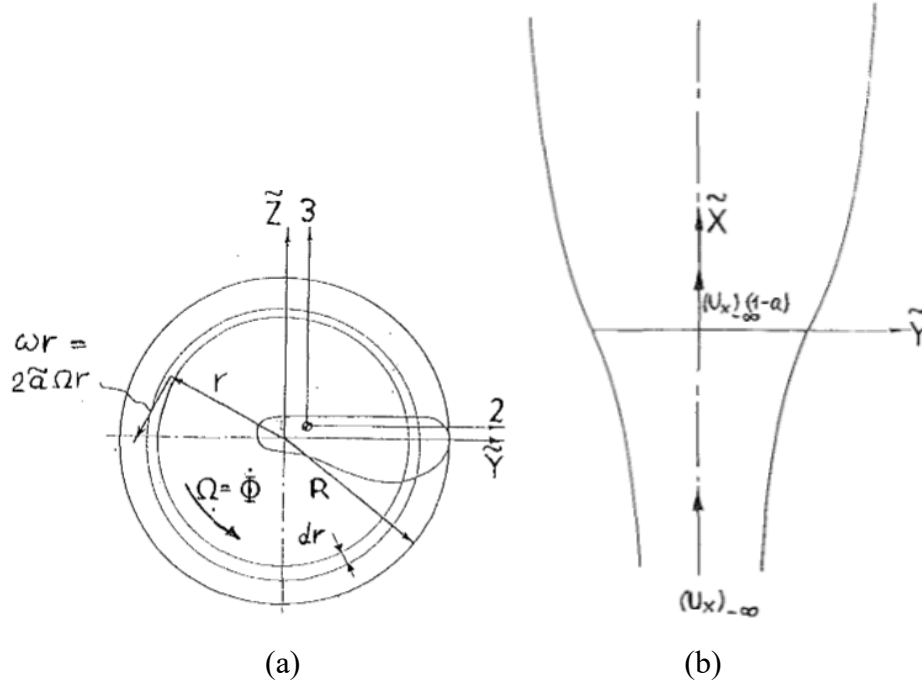
Figure 23. The actuator disk and induced velocities (Adapted from Rosen & Seter, 1991).

However, some researchers have argued that BEM may be inadequate for samara studies, as it cannot capture fully localized unstable effects and the wake influence on total forces (Rao et al., 2014; Zakaria et al., 2019). Additionally, one of the primary deficiencies of BEM models is that the calculated aerodynamic forces depend on sectional lift (C_L) and drag coefficients (C_D), and unfortunately, there is still ambiguity about which C_L and C_D expression method is most suitable for describing the samara LEV (Seter & Rosen, 1992; Rezgui et al., 2020).

For Rosen and Seter (1991), determining lift and drag coefficients in samara wings is challenging for three reasons: low Reynolds numbers, high local angles of attack, and surface roughness. Direct experiments would be ideal, but they are complex and require specific equipment. Therefore, these coefficients are estimated based on the literature's insect and bird wing data, compiled from various sources, resulting in some imprecision due to data variation. This approach is explored due to the need for more instrumentation availability and the complexity of the direct experiments.

As it was impossible to find a single source that could provide the entire spectrum of information, these charts (Fig. 24) represent a compilation of information from different sources. A few of these sources include Nachtigall (1981), Rees (1975), Vogel (1967), and Withers (1981). The imprecision associated with aerodynamic coefficients can be considerable.
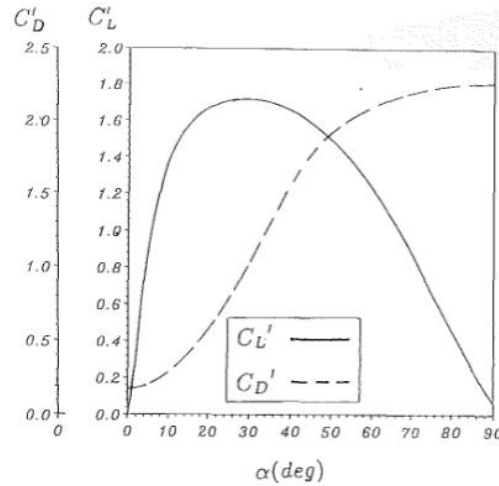
Figure 24. The lift and the drag coefficients are functions of the angles of attack (Rosen & Seter, 1991).

In this context, Azuma and Yasuda (1989) investigated the aerodynamic behavior of twenty species in a vertical wind tunnel, capturing their main characteristics, including C_D and C_L. In Figures 25a–c, a line close to the abscissa in the respective figures also shows the operational range of the attack angle along the respective species' span. In almost all species, it is considered that the wing operates at the maximum lift coefficient ($C_{L,max}$) over the entire wingspan. However, in some species considered high-performance, such as maple seeds, the wing's outer side (tip) operates in the assumed linear lift coefficient range, as commonly seen in Figure 25a.

Although the data are scattered over some intervals of a, $C_{L,max}$, and C_{D0} for a specific species, their average values are peculiar to the individual species, as shown in Fig. 24. The carp and the phoenix tree are given the highest lift coefficient $C_{L,max} \cong 1.8$ (Fig. 25b), and the lowest $C_{L,max} \cong 1.3$ (Fig. 25c), as their tip speeds are minimum and maximum, respectively, among the studied species. Similarly, the carp and the phoenix tree give the highest minimum drag coefficient, $CD0 \cong 0.2$, and the lowest $C_{D0} \cong 0.03$, respectively. As seen in Fig. 24, the maximum lift coefficient increases with the minimum drag coefficient but saturates at $C_{L,max} \cong 1.8$ (Azuma & Yasuda, 1989). A similarity is noted between the values in Fig. 24 and Fig. 25a–c.
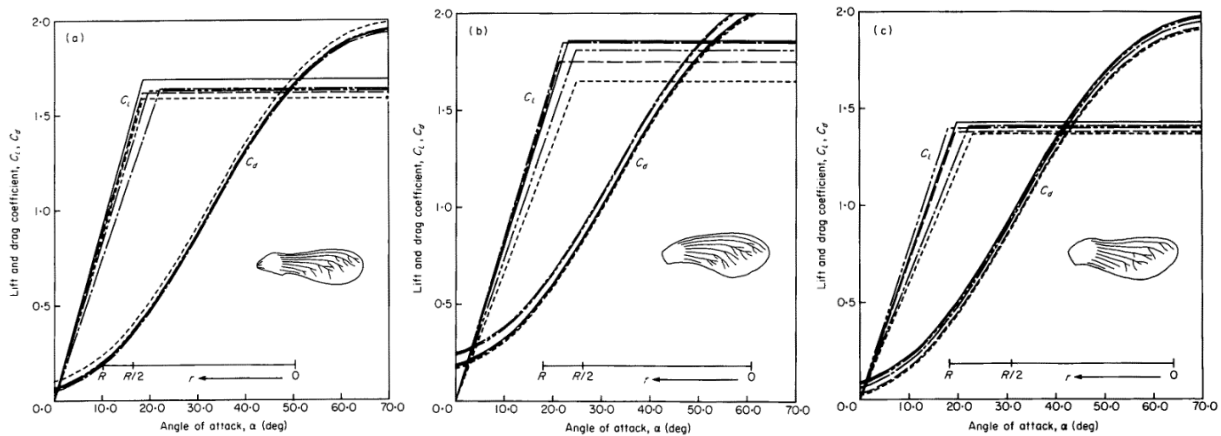
Figure 25. Two-dimension aerodynamic characteristics of airfoil section of rotary seeds. (a) *Acer diabolicum Blume*, (b) *Acer palmatum Thunb. var. Matsumurae Makino*, (c) *Acer palmatum Thunb.* (Azuma & Yasuda, 1989).

The aerodynamic and flow properties of the wing of a green maple seed were numerically investigated by Dang and Lai (2018) using CFD simulation software. The results of the lift coefficient showed that the green maple seed vane has a broader range of angles of attack, from 0° to 50°, without stalling. These blades were used in a small-scale horizontal-axis wind turbine. The best performance was achieved by the wind turbine with three blades, a swept area of 0.24 m², an angle of attack of 15°, and constant wind conditions of 5 m/s so that the highest wind/electrical energy conversion efficiency could be achieved, up to 37 %, in wind tunnel experiments.

Desenfans (2019) also suggests that standard gravitational constants and density (9.81 m/s² and 1.225 kg/m³) are appropriate since the maple seed is not launched from extreme heights. The seed is modeled as a NACA-2408 airfoil due to the similarity in thickness and curvature, although its actual thickness is smaller. The variation of the lift coefficient with the angle of attack depends on the Reynolds number. Adjustments may be necessary under extreme conditions.

For example, the Reynolds number, Eq. (2.47), can be empirically calculated assuming an ambient air temperature of 15° C. The number will depend on the distance to the center of rotation, so only the outermost part will be calculated, as it will provide the highest value. The resulting velocity will be the vector sum of the horizontal component caused by the rotation speed and the vertical component caused by the falling speed. To alleviate complexity, the Reynolds number is empirically calculated using values found in Varshney's publication (2011) as an example:

$$\text{Re} = \frac{\sqrt{(\omega R_{tot})^2 + v_z^2} \cdot L}{v} \tag{3.3}$$

$$\text{Re} = \frac{\sqrt{\left(77.9\frac{rad}{s} \cdot 0.029\frac{m}{s}\right)^2 + \left(0.94\frac{m}{s}\right)^2} \cdot 2.56 \cdot 10^{-4}\ N}{1.48 \cdot 10^{-5}\frac{m^2}{s}} = 2242.27$$

Due to the low velocity, the Reynolds number is significantly low, below the available data (50,000). This can affect accuracy. The drag coefficient can be estimated by assuming that the seed is a flat plate perpendicular to the airflow, resulting in a value of 1.98 for the drag coefficient (Sovran, 1978).

CHAPTER 4

4   BIOMIMETICS AS DESIGN INSPIRATION

Biomimetics aims to produce engineering systems that have characteristics, resemble, or function like living systems, particularly in cases where the performance and morphology of an organism exceed current mechanical technology. Exploring nature through the biomimetic or bioinspired approach seeks standard solutions from biology and engineering that enable greater efficiency and specialization (Vincent, 1990; Ralston & Swain, 2009). According to Fish (2006), by emulating biological characteristics in cases where organism performance exceeds manufactured devices, the performance of engineering systems can be enhanced through biomimicry. Additionally, engineers can leverage the various morphological and physiological specializations exhibited in biology for technology transfer and effectively reduce the time spent developing innovative technological solutions.

In general, conventional turbines, i.e., those optimized for a specific condition using the BEM theory, therefore, a blade shape that adapts to a wide range of TSRs has yet to be established. Classical turbines are designed to operate within a narrow zone centered on their ideal operating points, which vary with TSRs. This aerodynamic limitation leads to uncertainty in achieving desirable energy harvesting performance in a natural environment of turbulent wind, typically involving significant energy and economic losses (Ikeda, 2018).

In this context, to overcome this limitation, biomimetic design has emerged as an innovative approach to solving engineering challenges, drawing inspiration from the principles and strategies of nature. In wind turbines, biomimicry has been a source of inspiration for designing more efficient blades. Thus, new wind turbine designs have also come from animals and seeds from various locations worldwide, seeking some of nature's advantages. This chapter reviews research that has explored seed morphology in the design of biomimetic blades for wind turbines.

In analyzing existing research, it is essential to note that the goal is not to provide a comprehensive summary of all studies conducted to date. Instead, the approach will be selective, focusing specifically on points best highlighted for understanding and explaining the research. This will allow for a more accurate and targeted analysis, focusing on the most relevant elements that provide a solid context for the ongoing work without the need for a complete summary of all available research. Thus, the literature review will be strategic and geared towards the ongoing research objectives. Each section is named according to the scientific name of the seed that inspired the research (i.e., *Acer negundo*, *Acer platanoides*, *Dryobalanops aromatica*). At the same time, its subsections are identified by the type of analysis conducted (experimental and/or numerical) and the adaptation of its geometry for a specific type of turbine.

4.1 ACER NEGUNDO

4.1.1 Computational analysis of seed performance as a wind turbine

In the study by Holden et al. (2015) and Holden (2016), four *Acer Negundo* (*Boxelder Maple*) samaras native to the northern and midwestern regions of the United States were sent to a 3D engineering solutions company for computerized tomography scanning (Fig 26b). They produced watertight and high-fidelity parasolid models for CFD simulation. Figure 26 compares the 3D model (Fig. 26c) and a photograph of a seed of the same species (Fig. 26a).

| (a) | (b) | (c) |
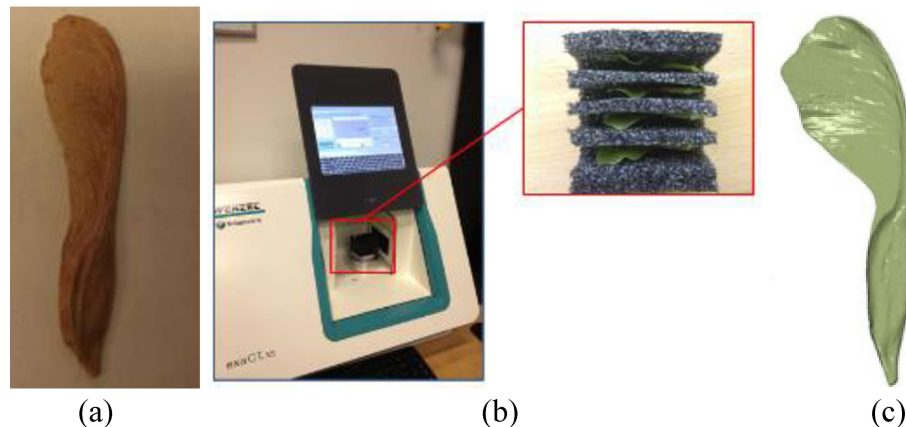
Figure 26. (a) Photograph of a seed of the same species, (b) Scanner, and (c) 3D solid part (Adapted from Holden, 2016).

In addition to the 3D geometry, it was also necessary to know the physical properties of the maple seed as it falls. For this purpose, a high-speed camera (3000 FPS) Phantom v7.3 was used in conjunction with a calibrated length scale in the camera frame to record the falling seeds and calculate quantities such as rotational speeds (824 ± 74 RPM) and vertical speeds (0.739 ± 0.045 m/s). Figure 27a shows a series of photos from the high-speed video. The measurement tool of Adobe Photoshop® was used to determine the cone angle from static images of the falling seed, as shown in Fig. 27b (approximately 16°).

| (a) | (b) |
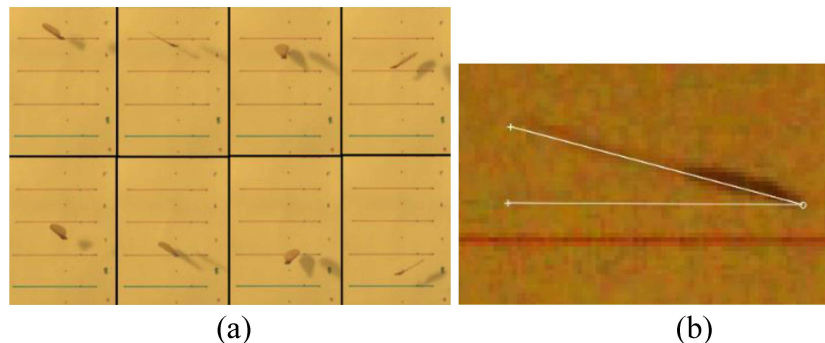
Figure 27. (a) Stills from high-speed video of falling maple seed (b) Still image of maple seed measured in Photoshop® for coning angle (Adapted from Holden, 2016).

The study utilized the STAR-CCM+® software from CD-Adapco, employing a 3D CAD interface, unstructured mesh, and flow solver. The simulation involved a single fixed maple seed rotating at an imposed rotation. A cylindrical domain was defined around the samara (Fig. 28a), with different boundaries and boundary conditions, including the seed as a wall, velocity inlet, and pressure outlets in the cylinder and far field. The resulting mesh had 820,649 cells in volume, with a denser mesh near the seed surfaces. Cut planes show the cell distribution near the seed surface in Figs. 28b and 28c.

(a) (b) (c)
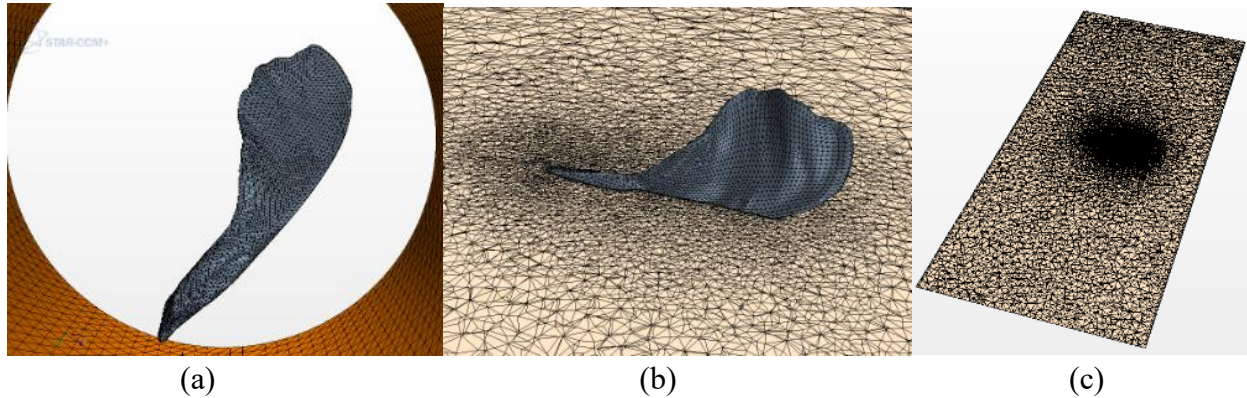
Figure 28. (a) The prism mesh layer on the seed surface and cylinder wall (b) A cut plane of the volume mesh as it grows out from the seed walls (c) a full cut plane of the volume mush in the same plane as Figure 28a(Adapted from Holden, 2016).

The simulation aimed to model the autorotation of a maple seed in free fall from a tree. This was accomplished by imposing an inlet velocity of 0.739 m/s and establishing a reference with an angular velocity of 824 RPM. Models and assumptions used included incompressible flow, Couette flow, K-ε turbulence model, steady flow, three-dimensional, two-layer y+ treatment, and an initial turbulence intensity of 1 %. Convergence was based on reducing residual values by 2-3 orders of magnitude.

After convergence, the analysis of aerodynamic performance and performance as a single-blade turbine was conducted, including the distribution of static pressure along the seed surface. This distribution highlights the concentration of higher pressure on the pressure side, as shown in Fig. 29. This pressure distribution is consistent with the geometry and mechanics of the fall of a maple seed. The more significant pressure difference, which is closer to the seed tip than the root, explains the conical rotation pattern of most seeds around their center of mass.
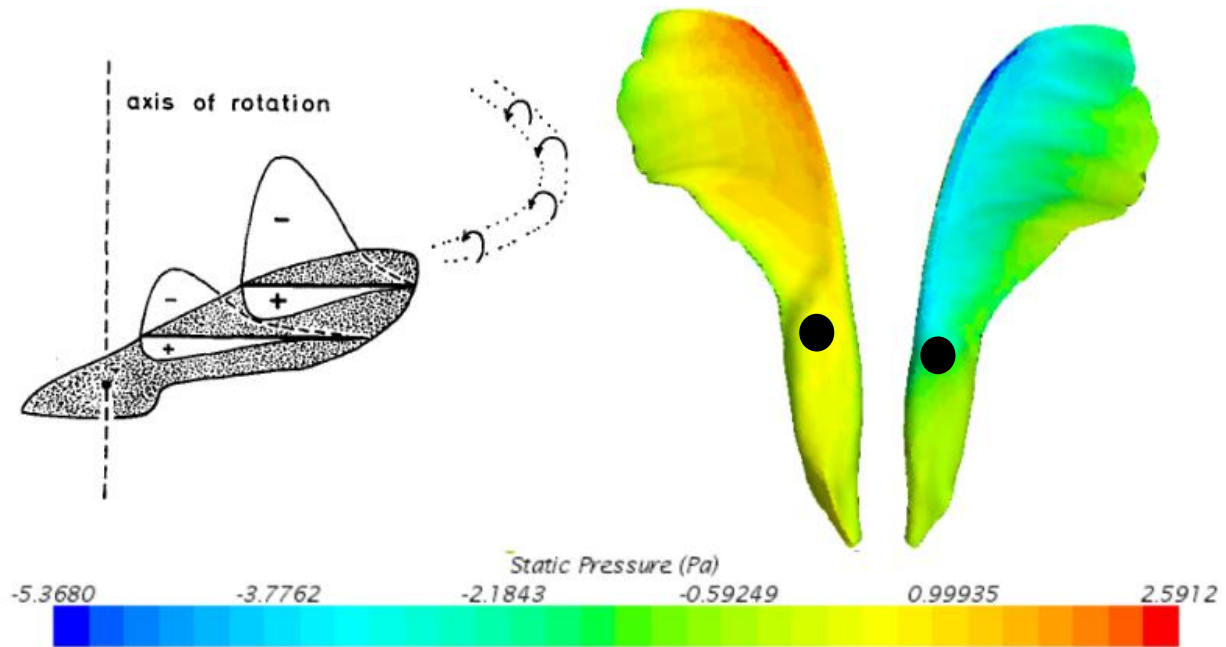
Figure 29. Noberg diagram (1973) (left), Static pressure on the pressure side (center) and suction side (right) of the seed. The black dots represent the axis of rotation (Adapted from Holden, 2016).

The pressure difference from the mid-chord to the trailing edge at the wing's center compared to the leading edge is almost negligible in autorotation. This explains why the maple seed can reach a steady state despite the lack of area in the wing, highlighting the importance of the tip fibers. Figure 30 shows streamline near the end of the maple seed, revealing the vortex shedding in the region of the trailing edge, approximately 75 % along the length.
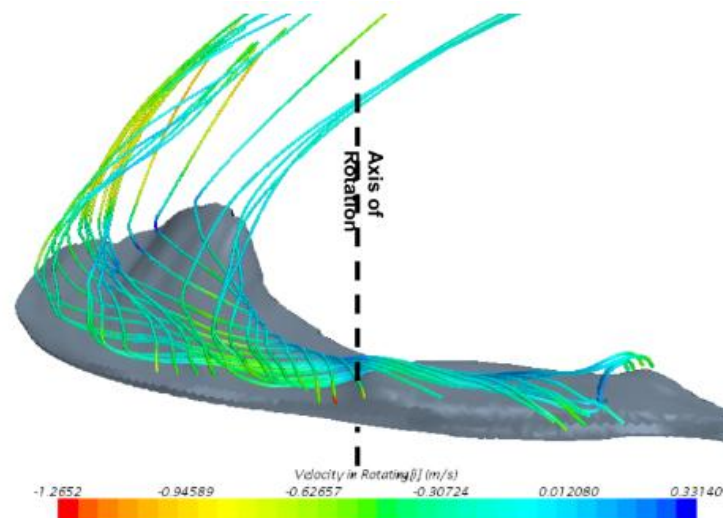
Figure 30. Relative velocity stream tubes at the blade tip (Adapted from Holden, 2016).

The absolute velocity streamlines are like those shown in Fig. 4, which is a promising outcome for studying the axial induction factor, measuring the energy extracted from the air. The circumferential average velocities across 13 concentric circles in Fig. 31 allow for calculating the

axial induction factor distribution for the maple seed. The average axial induction factor of the maple seed (Eq. 2.11), nearing the Betz limit, is significantly higher than the reference value by Sairam (a = 0.1637, 2013) for the National Renewable Energy Laboratory (NREL) Phase VI blade. Calculating C_P from this value, using Eq. (2.19), results in 0.59.
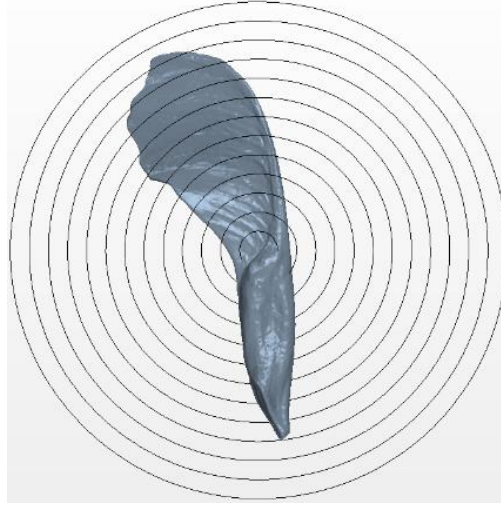
Figure 31. Locations of circumferential velocity averages at the plane just upstream of the rotor (Adapted from Holden, 2016).

Figures 32a and 32b reveal that the maple seed exhibits an axial induction factor profile like a wind turbine but with much higher values (lower velocities in the rotor plane). A surface integration is required to calculate the axial induction factor in the maple seed using STAR-CCM+® and determine the velocity u_R. The integration is performed on a plane parallel to the seed rather than perpendicular to the flow to obtain a more accurate integration of the velocity at a constant distance from the seed's surface.

(a)   (b)
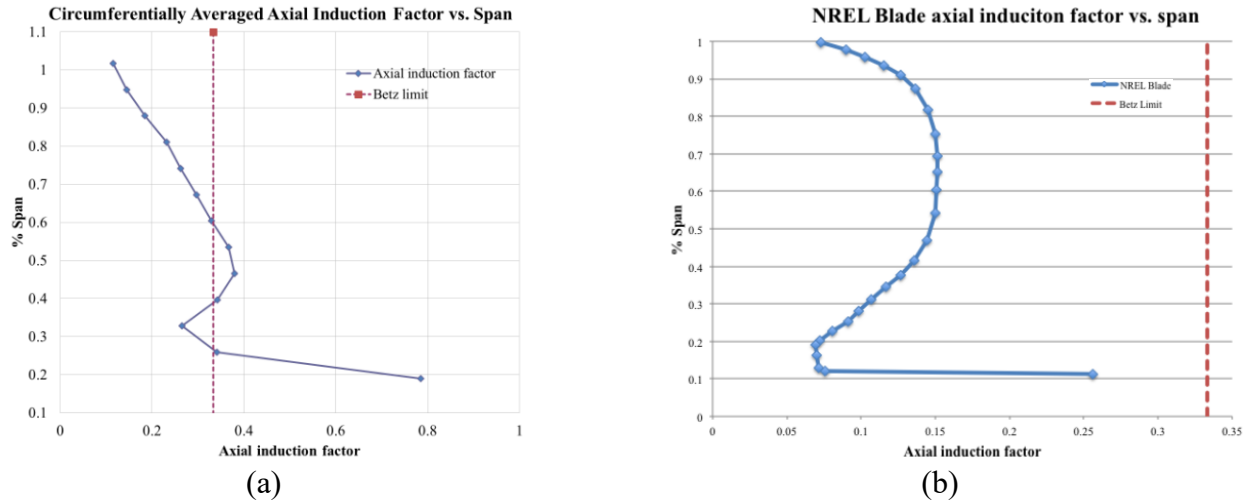
Figure 32. (a) Axial induction factor vs. maple seed span (Adapted from Holden, 2016) (b) Axial induction factor vs. span for original NREL blade (Manwell et al., 2002; Drela & Youngren, 2014).

The resultant axial force on the maple seed is considered for simulation. The seed remains fixed while the fluid moves, simulating the configuration of a seed in a vertical wind tunnel. The

goal is to match the resultant axial force with the weight of the seed (i.e., thrust = weight). However, a 36 % difference is observed between the resultant force (4.932 x 10^{-4} N) and the weight of a sample *of A. Negundo* (3.136 x 10^{-4} N). This is attributed to variations in the size and mass of the seeds, highlighting the need for precise weights of the scanned samples for effective simulation.

Following the maple seed's performance analysis, the next step involved reverse engineering the seed by creating a parametric model for scalability, further analysis, and design optimization. Due to its robustness, the 3-Dimensional Blade Geometry Builder (3DBGB) (Siddappaji, 2012) was used. This involved creating an airfoil section for the seed in the 3DBGB, designed to replicate the characteristics of the maple seed's surface (Fig. 33a). Twenty-four sections of varying chord lengths and stagger angles were used to define the 3D blade (Fig. 33b). The result mimics the most relevant geometric characteristics of the maple seed, including the staggered variation in span and the profile of the trailing edge.
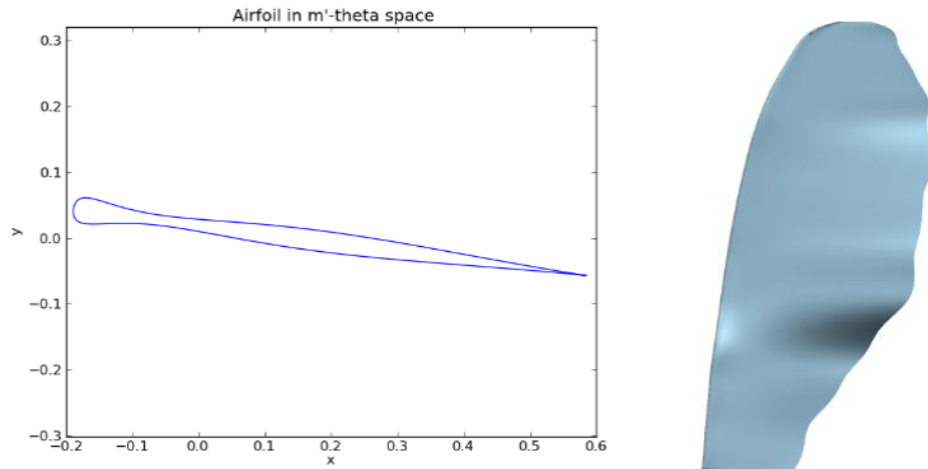
Figure 33. (a) 2D airfoil section created in 3DBGB, designed to mimic the 2D maple seed profile (b) 3D model of a wind turbine blade generated to mimic maple seed geometry (Holden, 2015).

A 2D aerodynamic analysis of the airfoil sections, as shown in Fig. 33a, was conducted using XFLR5®, which is a graphical user interface version of XFOIL®, across various spanwise sections defined at an angle of attack based on their respective stagger angles. The primary intention behind this was to observe the new airfoil sections' pressure distribution and the C_L's behavior versus the angle of attack. Figure 34a depicts the XFOIL® results for the C_{Pr} distribution along the airfoil. Figure 34b presents a plot of C_L versus α for a range of Reynolds Numbers.
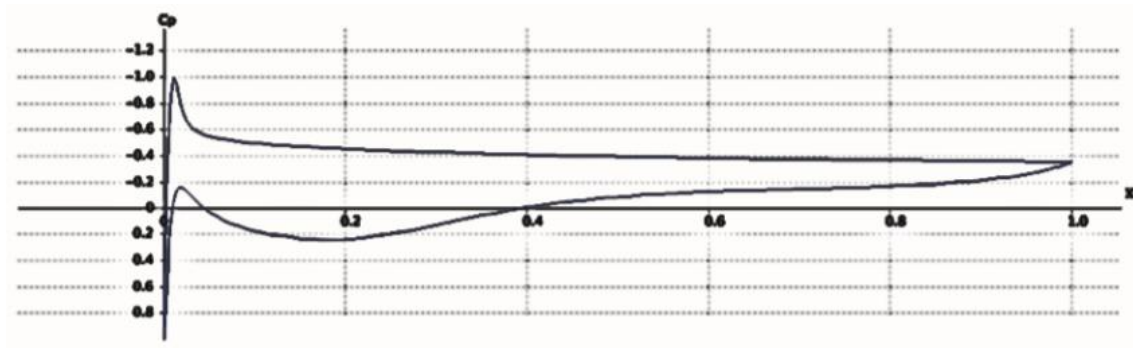
(a)
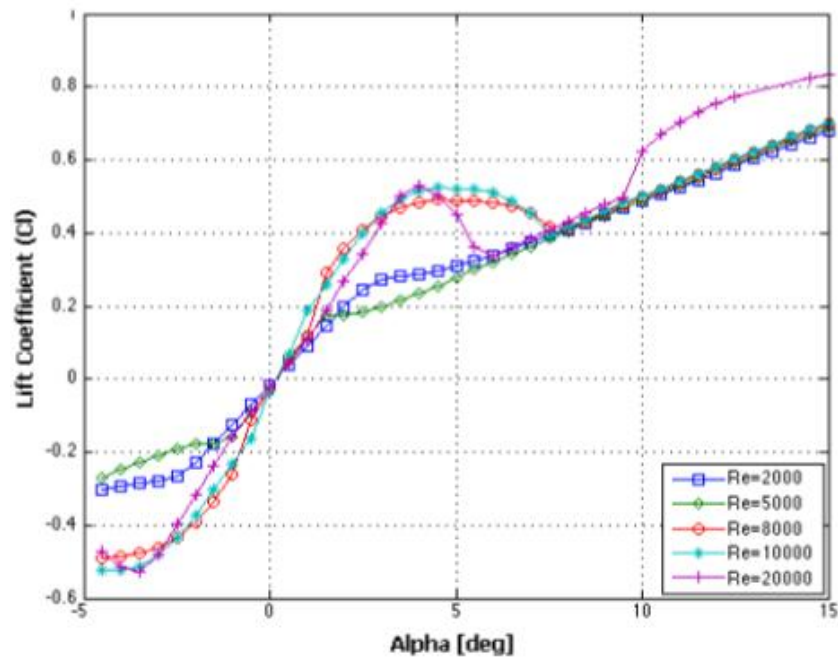
(b)

Figure 34. (a) C_{Pr} distribution for an airfoil section near the tip of the maple seed blade (b) C_L vs. alpha for Reynolds Number 2000 – 20000 (Holden, 2015)

The initial analysis of the reverse-engineered blade showed a different behavior compared to typical wind turbine blades with low Reynolds numbers and high angles of attack. This suggests that further investigation into the performance of this parametric design as a wind turbine blade is necessary. The reverse-engineering process was the first step toward having the capability to investigate. With the current geometry, design optimization can now be pursued. At these low Reynolds numbers, the integral boundary layer in XFOIL® and the k-ε turbulence model used in STAR-CCM+® lack detailed physics for this problem. LES, DES, and DNS simulations may provide more insights into physics, transition, and turbulence. However, the models used have helped explore the general characteristics of the maple seed.

4.2 Acer Platanoides

4.2.1 Experimental analysis of the performance of a multi-blade HAWT

Carré et al. (2022) investigates whether the autorotation of maple seeds is like the movement of turbine blades and determines if, in this configuration, they are as efficient as during free fall. Their research reports on designing and manufacturing a small-scale propeller and its experimental tests once assembled with an electromagnetic generator. For this purpose, they use, as a reference, the data from a 2021 study with 30 specimens of the maple species *Acer platanoides* (Fig. 35) from Norway by Nave et al. (2021), where the rotation speed of the samaras in free fall is 777 ± 264 RPM (81.4 ± 27.6 rad/s) and the descent speed is measured between 1.03 and 1.1 ± 0.32 m/s.
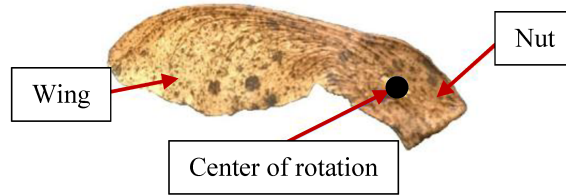
Figure 35. Side view of *Acer platanoides* seed sample (Adapted from Carré et al., 2022).

For their experiment, the wind speed in the tunnel, with a cross-sectional area of 400x600 mm^2, is therefore set at 1 m/s to achieve the same relative speed on the samaras. The wind tunnel generates wind speeds between 0 and 2.3 m/s, which are measured by a hot-wire anemometer (TSI 8465-300) with an accuracy of ± 0.01 m/s (Fig. 38). The rotation speed of the seeds is measured with a high-speed camera (2,000 FPS). For these tests, five samaras are pierced at the center of the nut and placed on a thin rod to create an artificial axis of rotation along their span, ranging from 20 to 31 mm. The results are detailed in Table 2. The comparison between free fall and restricted movement reveals that the maple samaras from Norway always exhibit higher rotation speeds with their fixed axis of rotation.

Additionally, another existing tunnel is used for higher speeds, between 3 and 8 m/s, to characterize the prototype over a broader range of airflow. This tunnel can generate winds between 3 and 45 m/s. The cross-sectional area of the vein is 23×23 cm^2 and 50 cm long.
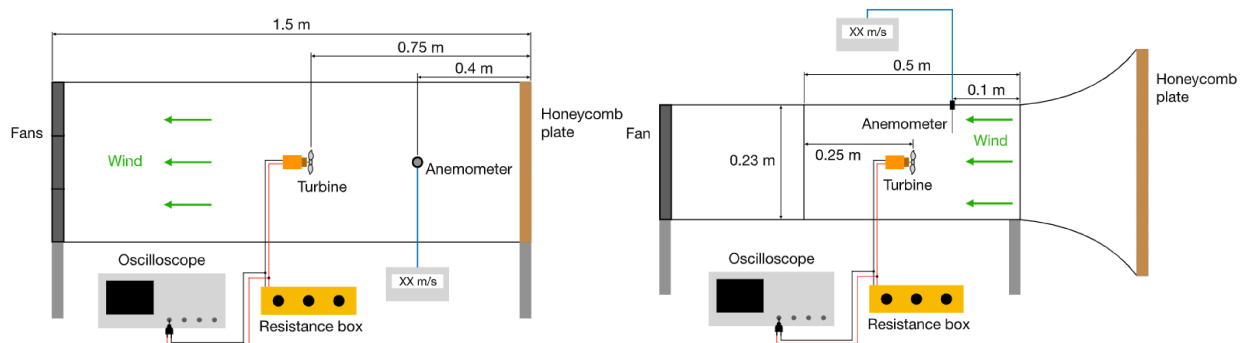
Figure 36. Schematics of (*a*) the first and (*b*) the second wind tunnel used for the experiments, with dimensions (Adapted from Carré et al., 2022).

Table 2. Rotation speeds for samaras with fixed axis (mean value ± standard deviation) (Adapted from Carré et al., 2022).

Rotation speed (RPM)		
Free fall (Nave et al., 2021)	777 ± 264	
This work	Measure 1	Measure 2
Samara 1	1442 ± 37	1337 ± 54
Samara 2	1690 ± 50	1738 ± 51
Samara 3	1337 ± 23	1356 ± 24
Samara 4	1576 ± 39	1557 ± 10
Samara 5	1814 ± 16	1843 ± 11

The increase varies from 72 % to 137 %, leading to values commonly observed in miniature turbine blades. This suggests that the samaras could have interesting aerodynamic properties like centimeter-scale blades. To obtain the best model for the design, Samara 5 was chosen to present the highest rotation speed with a fixed axis. The intention is to copy its shape as accurately as possible.

Subsequently, one face of samara no. 5 is scanned with an Altimet AltiSurf©520, a high-resolution scanner, to obtain the coordinates of approximately 3,000,000 points (Fig. 37a). The thickness of different parts of the seed–nut, leading edge, wing – is also measured. Then, the samara is built in CAD with the outer contour of the scan. The zone corresponding to the 4 mm radius nut is removed from the model to obtain the turbine blades, leaving only the wing (Fig. 37b). Blades are built by additive manufacturing with resin, with a minimum thickness of 0.4 mm. As a result, the blade's leading edge is also modified, resulting in a final thickness of 1 mm from an initial value of 0.5 mm. Figure 37c shows a four-blade propeller with imperfections from the supports and the removal stage.

(a)   (b)   (c)
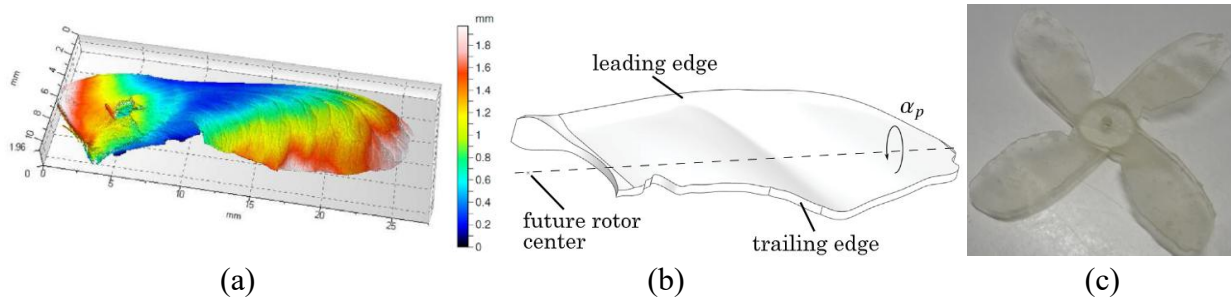
Figure 37. (a) Scan of the samara with colors representing the height of the points. (b) Global view of CAD reconstruction of a bioinspired blade for the propeller (c) Example of a propeller after fabrication, with imperfections due to the links with the supports (Adapted from Carré et al., 2022).

To create the bioinspired propeller, several wings are attached to an 8 mm diameter hub, corresponding to the size of the removed nut. Two angles of the blade can be altered: the pitch angle (α_p) and the cone angle (β). The rotation of the blade itself induces the α_p – and, therefore, impacts its angle of attack with the relative wind. It should be noted that this angle is constant from

the root to the tip of the blade. The β is the angle between the plane of rotation of the propeller and the axis of the blade; it is an angle that appears during the autorotation of the samara. Table 3 summarizes these specifications, and Fig. 38a shows the different parts in an exploded view of the CAD harvester with one of the propellers and one of the actual prototypes, Figure 38b. The generator used for this prototype is a homemade, coreless, permanent magnet micromachine with low-friction ceramic bearings used to convert rotation into electrical energy. This technology presents a low starting torque, which is interesting because it allows the propeller to rotate at low wind speeds.
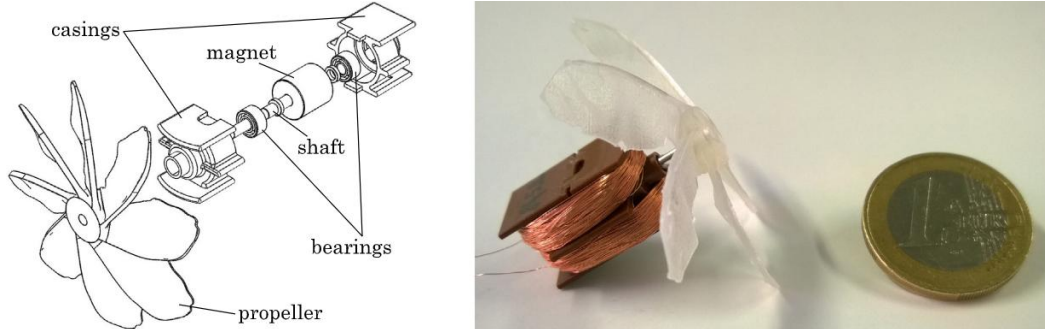
Figure 38. The bioinspired harvester: (a) CAD exploded representation ($Nb = 8$) and (b) real prototype ($Nb = 6$) next to a 1 euro coin for scale (Adapted from Carré et al., 2022).

Table 3. Summary of the bioinspired propellers and harvester specifications (Adapted from Carré et al., 2022).

Specification	Value
Rotor diameter	4.31, 4.39, 4.44 cm
Hub diameter	0.8 cm
Rotor area	15.2 cm^2
Number of blades	4, 6, 8
Pitch angle	8, 20, 30, 40, 50°
Coning angle	5, 10, 15°
Generator area	1.2 cm^2
Generator resistance	84.5 Ω
Harvester outer volume	38 cm^3

The performance of this 44 mm diameter HAWT is tested under wind speeds ranging from 1.2 to 8 m/s. The electrical output power measured under resistive load ranges from 41 µW to 81.7 mW, leading to an overall efficiency between 2.6 % (1.2 m/s) and 17.8 % (4 m/s) (Fig. 39a). In other words, the harvester presented here maintains satisfactory efficiency over a wide range of wind speeds. Additionally, confirming the choice of 8 blades, Fig. 39b shows the output power for propellers with 4, 6, and 8 blades, with $\alpha_p = 30°$ and $\beta = 5°$. This comparison can only be made for low air speeds, as the only propeller tested for $U_0 > 2.3$ m/s is optimal with $Nb = 8$.
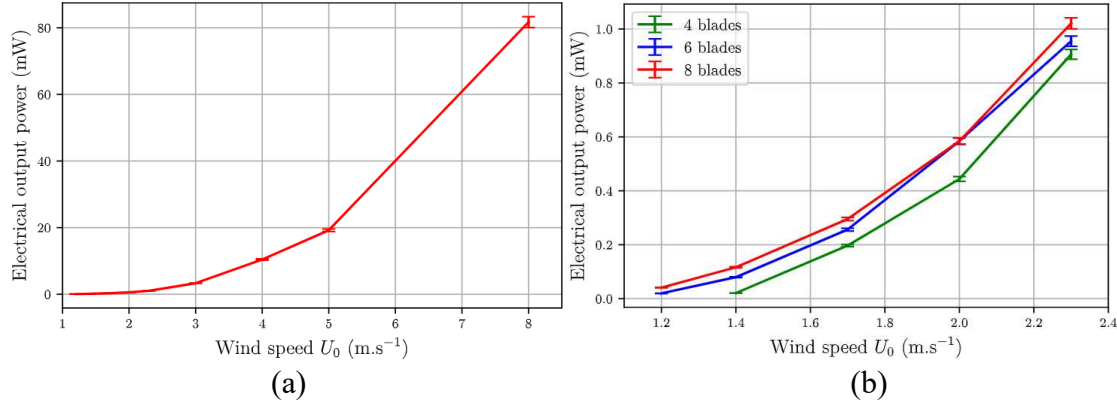
Figure 39. Maximum output power (*a*) for each wind speed tested for the optimal propeller and (*b*) for wind speeds between 1.2 and 2.3 m/s for propellers with 4, 6, and 8 blades, $\alpha_p = 30\circ$ and $\beta = 5\circ$ (Adapted from Carré et al., 2022).

The study evaluated the wind turbine performance of the TSR λ. This parameter allows fair comparisons between wind turbines, eliminating scale variations. The power coefficient C_P reached 28.4 %, demonstrating remarkable efficiency compared to other centimeter-scale turbines in the literature (Fig. 40), except for the 3.5 cm turbine by Gasnier et al. (2019). Furthermore, the turbine has one of the widest ranges of wind speeds for energy collection and successfully meets a minimum demand of 100 µW from winds at 1.4 m/s, highlighting its high performance over a broader range of wind speeds.
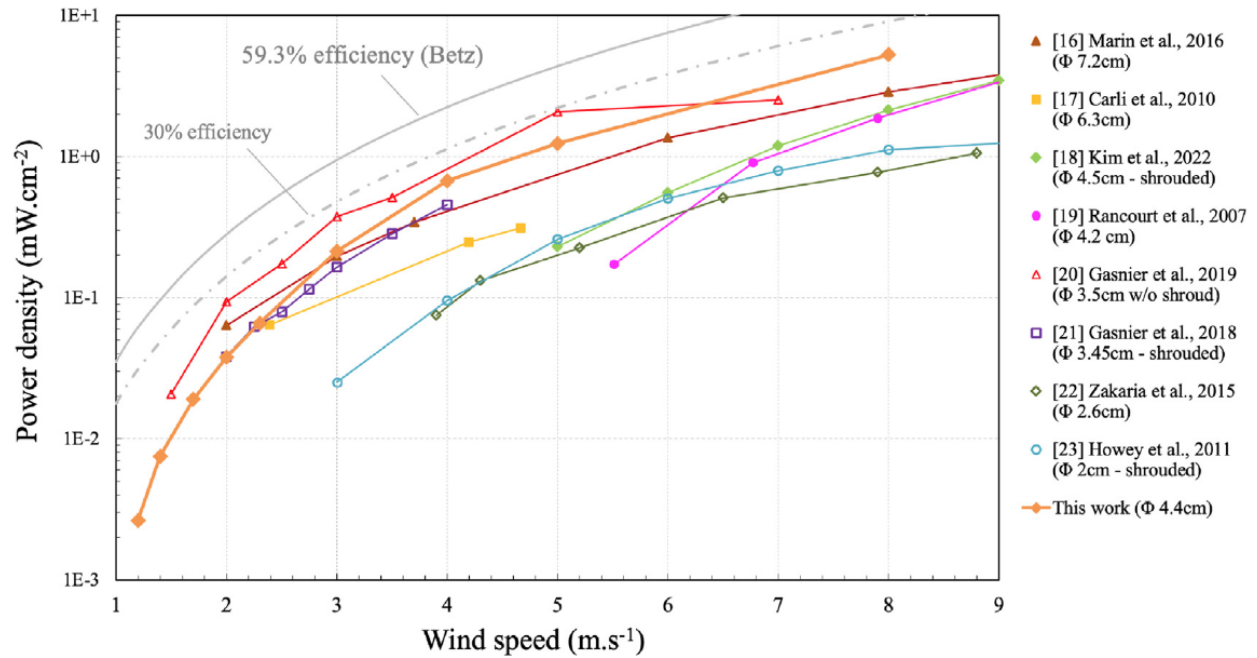
Figure 40. Power density comparison for centimeter-scale harvesters in the literature (diameter ≤ 7 cm) (Carré et al., 2022).

Carré et al. (2022) compared the C_P of a centimeter-scale wind turbine with large-scale turbines about the λ ratio (Fig. 41). The C_P curves exhibited a linear behavior at low λ, reaching a maximum value around $\lambda = 1.3 - 1.4$, and then decreasing. Although the C_P of the centimeter-scale turbine is lower at low λ, the maximum values approach those of large-scale counterparts, such as the American wind turbine by Hau (2006). However, the efficiency at low λ, representing low rotational speeds, is a disadvantage of the bioinspired propeller compared to conventional turbines: between 5 and 15 % versus 25 % - 30 %. Overall, the characteristics between the prototype and the large-scale turbine are similar, especially at high λ: between 24 and 29 % versus 31 %, but are achieved at high TSRs.
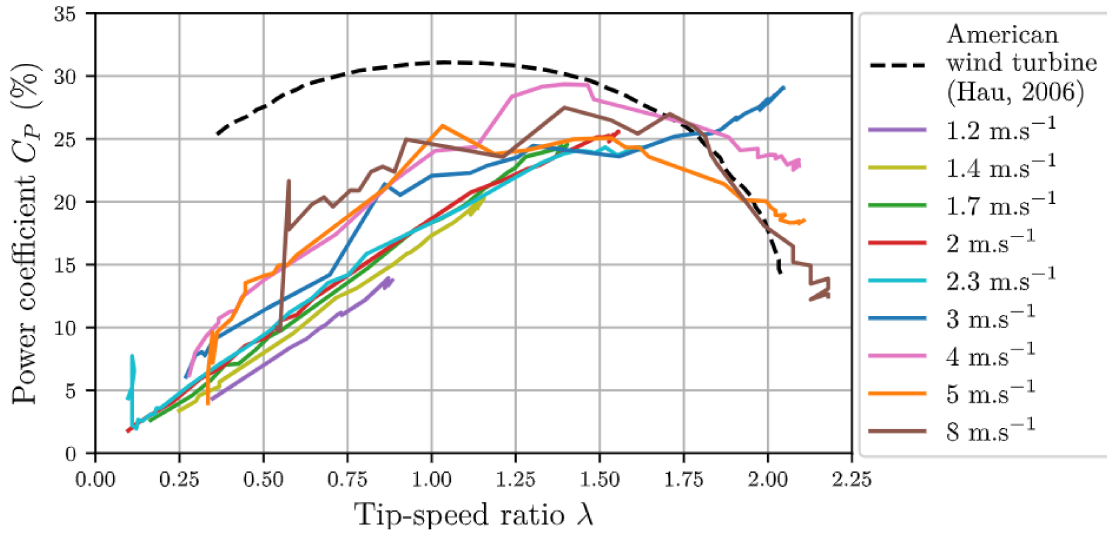
Figure 41. Comparison of power coefficient values between the bioinspired harvester and the American wind turbine (theoretical) (Hau, 2006) (Carré et al., 2022).

4.3 DRYOBALANOPS AROMATICA

4.3.1 Numerical analysis of the performance of a bioinspired HAWT blade

Chu and Chong (2017) studied the performance of a biomimetic rotor blade inspired by the seed of *Dryobalanops aromatica* (Fig. 42) using OpenFOAM® CFD software. The research aimed to propose a high-performance biomimetic wind turbine design, as the wind turbine and the Borneo camphor seed share a similar rotation mechanism. Due to the conical shape of the Borneo camphor seed, it can align itself to face the oncoming relative wind during the fall, generating torque around the seed's axis of rotation and initiating autorotation. This autorotation expands the "wings" radially outward, increasing the rotor size, enhancing lift and drag forces, and slowing down the winged seed's descent (Chu; Lam; Peng, 2022).

To generate the blade's 3D design, different photos of the seed were taken from various angles. Then, the design mimicked the edges and intermediate sections of the wing sections extracted from the photos using the GetData Graph Digitizer® (Federov, 2002).

Figure 42. (a) Side view and (b) bottom view of *Dryobalanops aromatica* seed sample (Adapted from Chu, 2018).

Finally, the geometric model had a scale of 0.9 m in diameter and 1 mm in thickness. Chu and Chong (2017) varied the thickness of the biomimetic blades to have the same volume as the reference HAWT ($8.85×10^{-5}$ m^3) by Krogstad and Lund (2012), which uses the S826 airfoil, aiming to investigate in terms of cost-effectiveness and compare with a conical and twisted blade. Another investigation was made by reducing the solidity of the original HAWT biomimetic blades (Fig. 43a) to match the solidity of the University of Malaysia benchmark HAWT (Fig. 43b). By Eq. (1.44), the solidities were 0.09355 and 0.31816, respectively, for the reference HAWT and original biomimetic HAWT. The scale factor to model the reduced solidity biomimetic HAWT was 0.29402 in the chord and streamwise directions. The hub diameter, rotor diameter, and even nacelle length of the reference HAWT (Fig. 43c) were kept the same in all three cases. The reason for reducing the original biomimetic HAWT solidity in the reduced solidity biomimetic HAWT is to investigate the effect on its performance when the chord length of the HAWT blade is reduced.
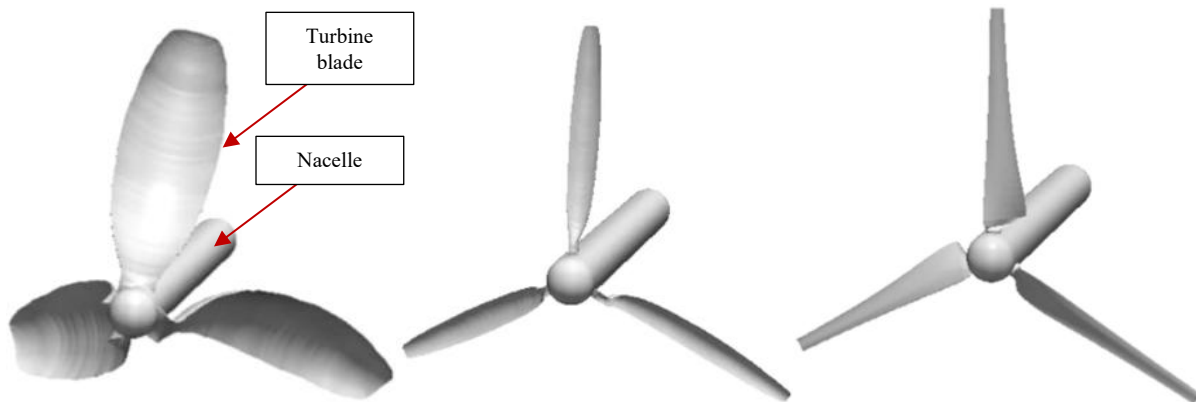
Figure 43. 3D model of the (a) biomimetic, (b) scaled biomimetic (Chu & Chong, 2017), and (c) tapered and twisted blades wind turbine (Krogstad & Lund, 2012).

The numerical scheme, solution, and algorithm control settings were based on the OpenFOAM® user guide (2015). The SST k-ω turbulence model (Menter, 1994) was used to predict flow boundary layers, including laminar and transitional flow at moderate flow pressure gradients (Menter, 2003) when surface meshes are refined to the non-dimensional wall distance y+ <5, as recommended by FLUENT®. Furthermore, despite some limitations, the SST k-ω could provide comparable predictions of flow pressure coefficients passing through a cylinder at low Re

of 1000 and 3900, as shown in Patel (2010). Mesh slice sections at r/R = 0.5 (where r is the radial distance along the blade length measured from the axis of rotation while R is the rotor radius) of the proposed biomimetic and Krogstad and Lund (2012) wind turbine blades are shown in Fig. 44a, 44b, 44c, while the mesh domains are shown in Fig. 44d, 44e, 44f.
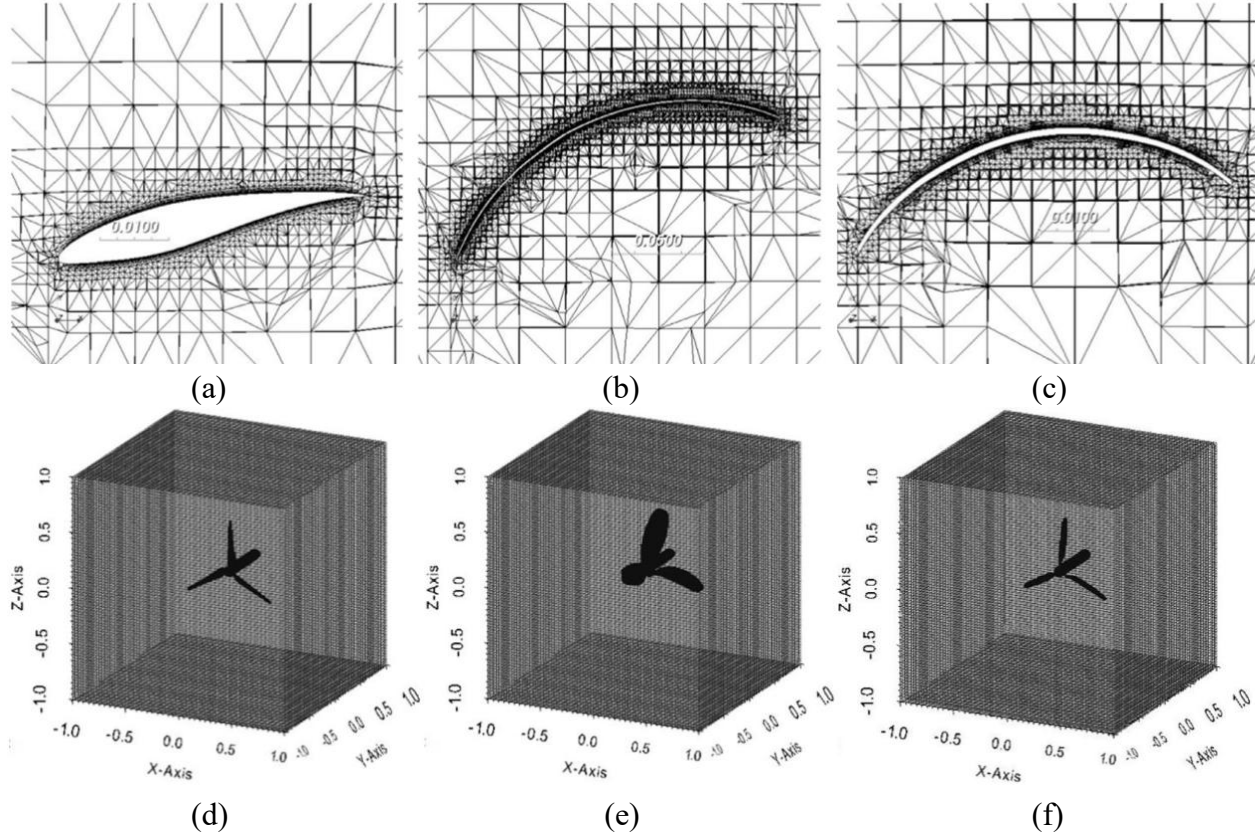
Figure 44. Mesh slice sections at r/R = 0.5 for (a) Krogstad and Lund (2012), (b) biomimetic and (c) scaled biomimetic wind turbine cases with their mesh domains (d), (e) and (f) respectively (Adapted from Chu, 2018).

The simulation results (Fig. 45a and 45b) show that the predicted maximum C_P of the reference HAWT (C_P = 0.464) is 16.75% higher than the biomimetic HAWT (C_P = 0.386) and is 27.2 % higher than the reduced solidity biomimetic HAWT, where C_P is 0.338. The C_T at ideal TSRs for reference HAWT is 8 % and 1.5 % lower than the original and reduced solidity versions of the biomimetic HAWT, respectively. Figure 45 presents the predicted C_P and C_T results of the mentioned HAWTs at u_∞ = 10 m/s, where Exp denotes experimental data, S1 denotes fine mesh, and y+1 denotes mesh with y+ < 1.
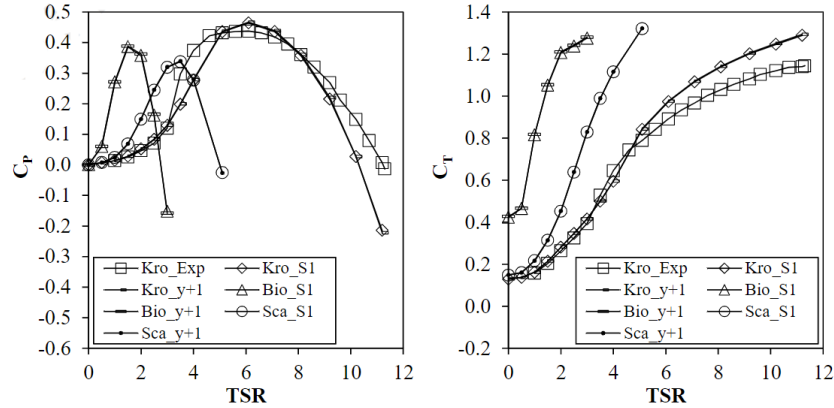
Figure 45. C_P and C_T against TSR graphs of Krogstad and Lund (2012), the proposed biomimetic and scaled biomimetic wind turbines at U∞ = 10 m/s, where Exp denotes experimental data, S1 denotes fine mesh, y+1 denoted y+ < 1 (Adapted from Chu, 2018).

The pitch and cone angle, which was 42°, were the two standards involved in the biomimetic enhancement of the blade. The induced torque for the proposed biomimetic wind turbine in the initial phase, when the TSR was 0, was 2 Nm, which was 772 % higher than classical wind turbines (Fig. 46). Thus, the bioinspired wind turbine could outperform classical wind turbines in terms of automatic start and performance in low wind speed conditions (Krogstad & Lund, 2012). The centrifugal force on the blade was predicted to be excessively high. Therefore, the model proved to be economical, producing high torque and having the ability to operate in low wind speed conditions.
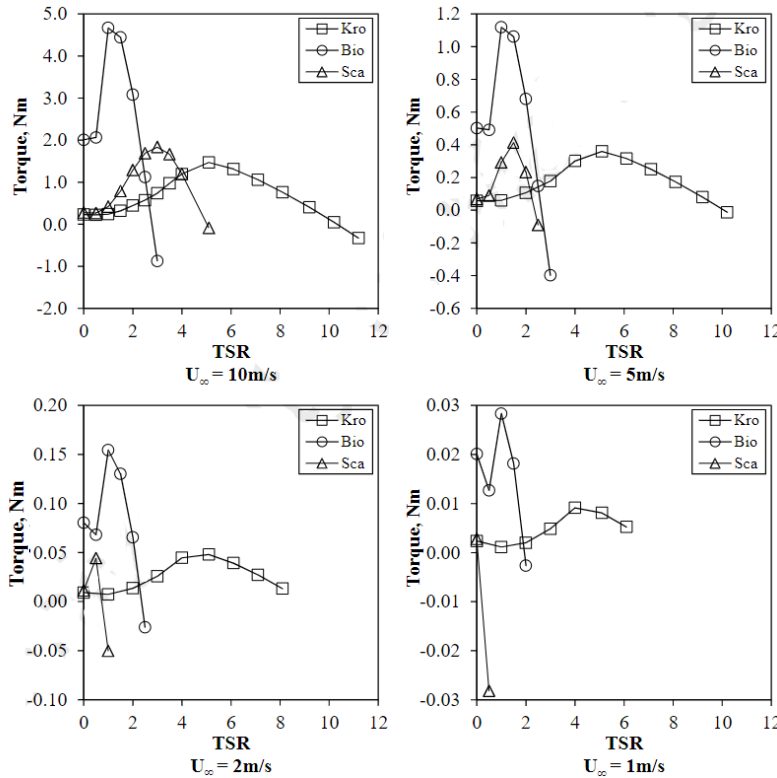
Figure 46. Torque against TSR graphs of all turbines at different free stream velocities ranged from 1 m/s to 10 m/s (Adapted from Chu, 2018).

The analysis compared the performance of reference HAWT turbines with original and reduced solidity biomimetic ones, using Cp calculated by OpenFOAM®. The original biomimetic HAWT has a cut-in speed of 2 m/s, lower than that of the reference HAWT, and the reduced solidity biomimetic, both at four m/s. The reference HAWT outperforms the original biomimetic by 6.6 % and the reduced solidity by 32.3 % in nominal power. Optimization is necessary to compete with the reference HAWT, whose cutout speed is 25 m/s, typical for HAWTs. The cut-out wind speeds of the mentioned turbines were set at 25 m/s, the typical cut-out wind speed of HAWTs, as seen in Fig. 47.
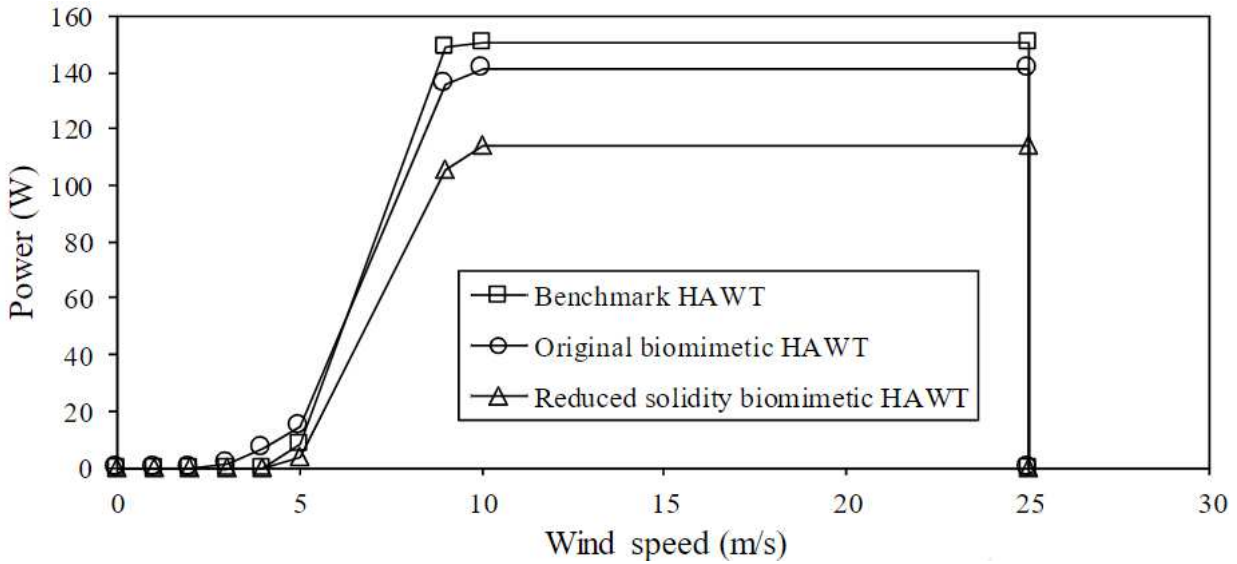
Figure 47. Wind power output of the benchmark, original, and reduced solidity biomimetic HAWTs (Adapted from Chu, 2018).

Other studies have been conducted involving wind and hydraulic turbines inspired by the camphor seed from Borneo. Chu et al. (2022) at the University of Malaysia applied CFD to predict the performance of biomimetic wind turbine models, focusing on the seed's wings' natural geometry. 3D scanning, using an ATOS scanner with a 0.2 mm spacing, captured the natural shape of the seed's wing in stereolithography (STL) format (Fig. 48a, Fig. 48b), which was processed in ANSYS SpaceClaim® software.

An enlarged wing featuring delicate curves and features was isolated and sized to accommodate a 0.2 m diameter hub and a 1 m diameter rotor. Cross-sectional views of the enlarged wing model are shown in Fig. 48. This study differs from previous research that did not represent the natural geometry of the Borneo camphor seed wing.
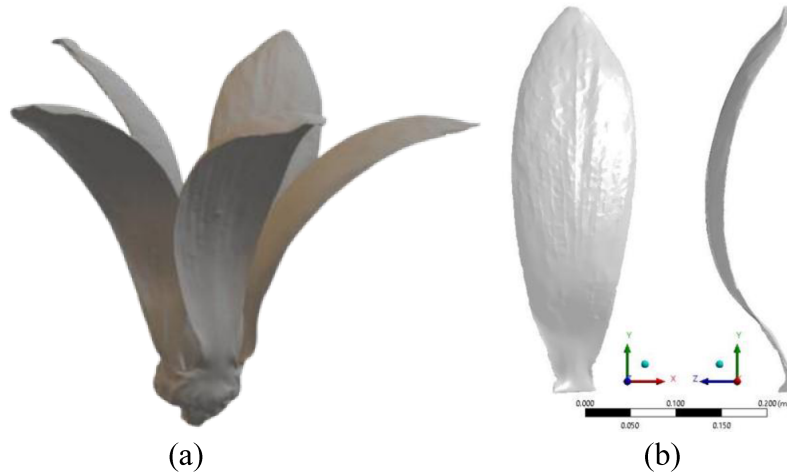
Figure 48. (a) 3D-scanned model of the Borneo camphor seeds sample (b) Views of the convex surface (left) and side (right) of a scaled-up wing model (Adapted from Chu et al., 2022).

All wing sections (Fig. 49) were thin, except near the hub (r/R=0.2), with a variation in chord length from short to long (r/R=0.2 to r/R=1), being short at the most extreme sections and longer at the intermediate ones. Unlike conventional blades with teardrop-shaped sections, the wing had curvatures along its span, as shown in Fig. 49. These unique characteristics allowed for more economical manufacturing methods, such as plastic molding or sheet metal. The use of vacuum molding, for example, was a viable option for manufacturing the biomimetic blades of the proposed wind turbine.
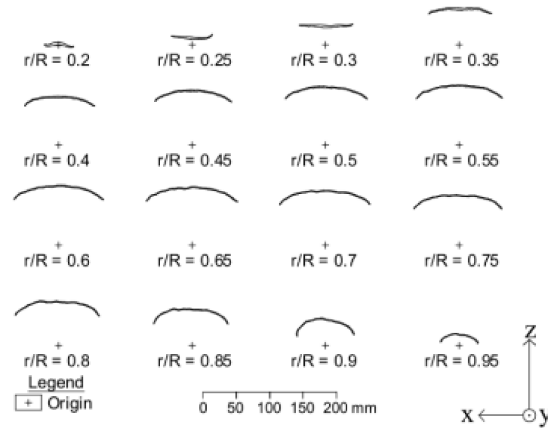
Figure 49. Cross-sections of the scaled-up wing model. Where r means radial distance and R means radius (Chu et al., 2022).

All parameters related to the wing layout are illustrated in Fig. 50. P is the location of the blade root where the bending axis passes, θ_r is the bending angle, αr is the bending axis angle, R is the rotor radius, Rh is the hub radius, and r is the radial distance measured from the origin.
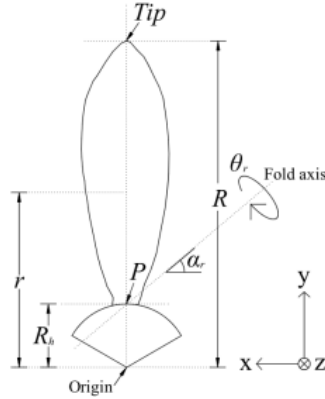
Figure 50. Sketch showing the wing layout attached to the hub with its associated parameters (Chu et al., 2022).

The ANSYS Fluent® software used the Multiple Reference Frame (MRF) model, precisely the multiple reference frame, to model the airflow around the rotating biomimetic turbine. The Semi-Implicit Method for Pressure-Linked Equations (SIMPLE) algorithm was used to solve the fluid flow equations. The SST k-ω turbulence model was chosen for wind turbine simulation. Only one-third of the turbine was modeled to save computational time, with an interface boundary between the stator and rotor domains. The CFD domain was divided into the stator and rotor domains (Fig. 51). The stator domain consists of the circular sector arc surface wall boundary and periodic wall boundary at the radius surfaces. The rotor domain is where the wind turbine blade and hub are located. An interface boundary was located between the stator and rotor domain boundaries, separating the two domains. The overall domain dimension was like Chu et al., 2021.
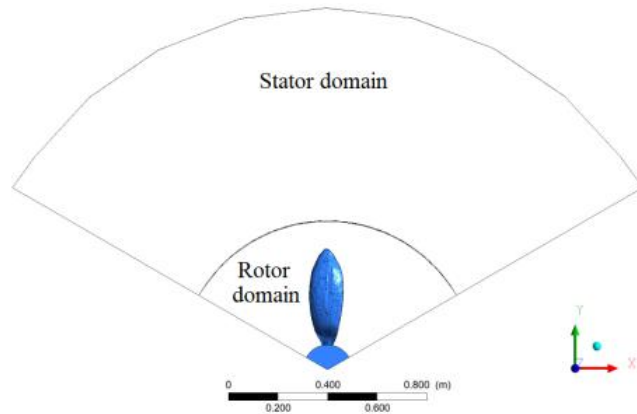
Figure 51. The section view of the CFD model domain shows the wing, hub, stator, and rotor (Chu et al., 2022).

Boundary conditions included a wind speed of 10 m/s, 0.3 5% turbulence intensity, air density of 1.225 kg/m³, and kinematic viscosity of $1.46 \times 10\text{-}5$ m²/s. A reference wind turbine model like that of (Chu et al., 2021) was used, with a rotor diameter of 1 m, SD8000 airfoil, zero-degree pitch angle, and no twist in the blade sections. Using polygonal cells for the remaining mesh in the rotor and stator domains improved convergence and reduced computational time. The prism cell type was used on all surfaces of the wind turbine blades, while the polygonal cell type was used for the rest of the meshes in the rotor and stator domains. The rationale for adopting

polygonal meshes is that they improve convergence and reduce computational time. The mesh layout of the biomimetic wing section at r = 0.43 m is shown in Fig. 52.
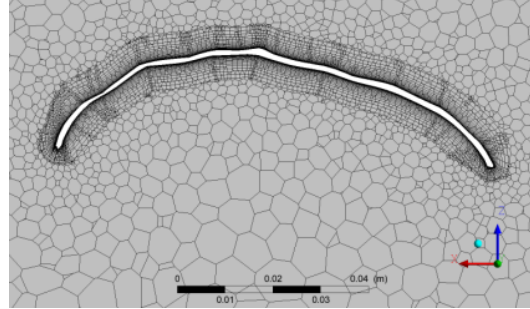
Figure 52. Mesh layout of the wing section at r = 0.43 m (Chu et al., 2022).

A mesh dependency test was conducted to verify the accuracy of the CFD simulation. Mesh sizes of 0.001 m, 0.07 m, and 0.36 m for the turbine blade, rotor domain, and stator domain showed convergence and results nearly matching the experimental data. These mesh properties were used in the biomimetic wind turbine cases, assuming they would produce accurate results that shared the same conditions. All biomimetic cases exhibited C_P vs. TSR curves in the shape of an inverted "U". As shown in Table 4, nine different configurations of αr and θr were tested, with a range of 15° to 45°; it is essential to note that after "folding" the rotor radiuses were reduced. The results (Fig. 53) show that the highest C_P was 0.3861 for the biomimetic wind turbine model, which is 20.14 % higher than that of a reference case when the folding axis and folding angles are both 30°. The C_T value increased with TSR in low folding angle configurations. For example, Case 1 achieved the highest C_T, while Case 9 had the lowest.

Table 4. Summary of $C_{P,Peak}$, starting torque, and C_T at $C_{P,Peak}$ for all wind turbine cases (Adapted from Chu et al., 2022).

Case	α_r(°)	θ_r(°)	Rotor radius, R (m)	$C_{P,Peak}$	Torque (N.m)	C_T at $C_{P,Peak}$
1	15	15	0.4873	0.2914	0.2945	1.1146
2	30	15	0.4898	0.3384	0.5477	1.1146
3	45	15	0.4932	0.3538	0.7694	1.0390
4	15	30	0.4502	0.3861	0.5200	1.1182
5	30	30	0.4604	0.3403	0.9889	0.9434
6	45	30	0.4740	0.3781	1.4024	0.7583
7	15	45	0.3918	0.3181	0.6898	1.0140
8	30	45	0.4152	0.3153	1.3106	0.6397
9	45	45	0.4453	0.2288	1.8671	0.4346
Benchmark (CFD Case) (Lee; Shiah; Bai, 2015)	25	0	0.5	0.3214	0.0901	1.3533
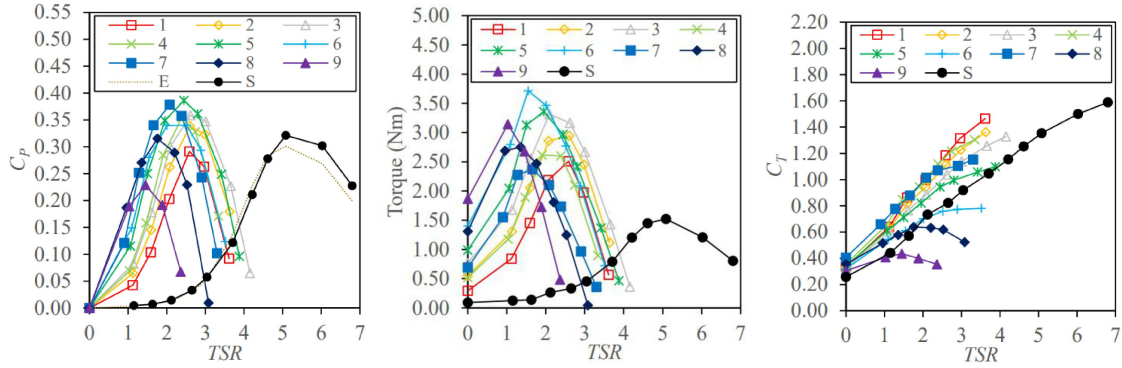
Figure 53. CFD results are plotted as (a) C_P versus TSR, (b) torque versus TSR, and (c) C_T versus TSR graphs of biomimetic wind turbine cases. E is experimental data from Lee, Shia, and Bai (2016), while S is simulation results of the benchmark case (Adapted from Chu et al., 2022).

4.4 PETREA VOLUBILIS – CHORRILLO

4.4.1 Experimental analysis of the performance of bioinspired blades as a piston pump

An experimental approach adapting Chorrillo (*Petrea volubilis*), also known as the queen's wreath or Machiguá flower found in Córdoba – Colombia, as a wind turbine rotor design was first undertaken by Vergara (2010). This seed is composed of five equiangular petals, shown in Figure 54a, and these petals are considered blades of a wind turbine during simulation. For this bioinspired model, its solidity averages 28.13 %, indicating that this rotor has an intermediate solidity. Its use in wind pumps is suitable, as shown in Fig. 14, as it is close to the solidity of lightweight wind pumps.

A specimen of the inflorescence was subjected to point cloud scanning and processing through a PS-3300 laser scanner. Then, noise reduction was performed using a proprietary algorithm from the device manufacturer. This resulted in a point cloud of the plant petal surfaces, which was subsequently polygonalized in Rhinoceros software, producing a file that could be used in CAD software. Figure 54b shows the scanning result, and Figure 54c shows the point cloud and surface creation.

(a)   (b)   (c)
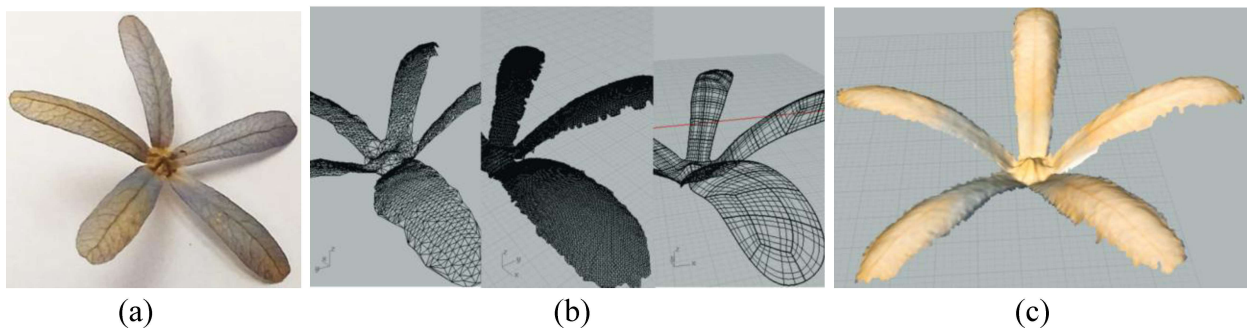
Figure 54. (a) Inflorescence of Petrea Volubilis seed, so-called Queen's Wreath (b – c) Scanning of the seed (Adapted from Vergara, 2010).

The manipulation of the CAD model enabled the generation of a file containing the geometry of a petal (future blade of the rotor) to be manufactured using a polyester resin mold (Fig. 55a and 55b). The printed petal was 26 cm long and was made at this scale to maximize the rotor's utilization of the airflow area in the wind tunnel, whose diameter was approximately 66 cm.

| (a) | (b) | (c) |
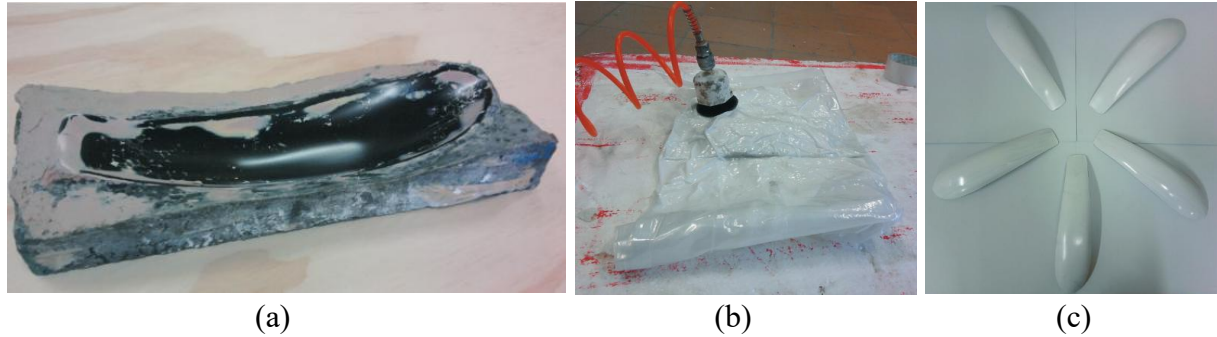
Figure 55. Manufacturing process (a) Polyester resin matrix (B) Vacuum generation (c) End petals (Adapted from Vergara, 2010).

The chosen pump type is the piston pump due to its simple design, ability to operate at high discharge pressure, low flow rates, and close to 90 % efficiency (Kreith, 1999). The design values from Table 5 are considered to determine the pump size.

Table 5. Drawing data for pump size (Adapted from Vergara, 2010).

C_{Pmax}	D [m]	λ	i	H [m]	η_{vol}	$V_{diseño}$ [m/s]
0.3	0,6	2	7	2	0.9	3

The piston pump operates with a pair of check valves located at its inlet and outlet. These valves prevent fluid exchange between the suction and discharge lines and allow the pump to self-prime without intervention. The installed tubing is made of PVC and has a diameter of 3/8 inch. The assembled unit and the pump can be seen in Fig. 56.
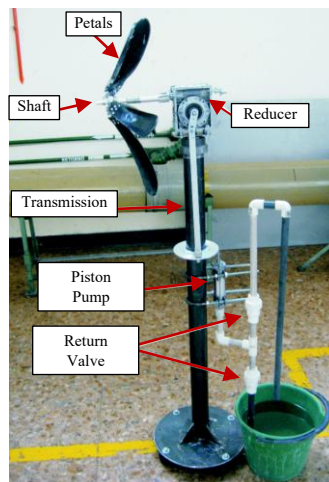
Figure 56. The pump is coupled to the rotor assembly and transmission system (Adapted from Vergara, 2010).

The equation used in the design considers power, pressure in the circuit, rotations, and piston rod diameter. To determine the size of the pistons, a speed range of 150 RPM to 1000 RPM was considered at different wind speeds. The shaft power was based on the power available in the wind stream for these speeds, with a maximum performance of 0.6. The system pressure varied from 10 to 150 psi for appropriate readings on the available pressure gauges. To minimize friction during movement, a friction coefficient of 0.2 between steel and bronze was estimated, with 0.05 m between the point of force application and the center of the shaft. Based on these parameters, the size of the piston rod was determined.

Table 6. Piston rod size considers the extremes of the pressure range and torque moment (Adapted from Vergara, 2010).

V [m/s]	P_{wind} [Watts]	Pmec with $C_P = 0.6$ [Watts]	ω [rad/s]	Pressure [psi]	Dp [m]	Drag moment [N.m]
9	97.65	58.59	104,72	150	0.00587	0.56
3.5	5.74	3.44	15.71	10	0.01421	0.22

As seen in Tab. 6, the diameter of the piston rod is between 6 mm and 14 mm, but the pressure width and, therefore, the torque moment it generates must be determined.

4.4.2 Experimental and numerical analysis of the performance of bioinspired blades such as HAWT

Gaitan-Aroca et al. (2020) conducted experiments and numerical analyses of a bioinspired HAWT using the CFD software OpenFoam®. Five fiberglass blades covered with white Geal Coat were used in the experiment. The rotor diameter was 0.6 meters, and the rotation speed varied from 180 to 1100 RPM with an upstream velocity range of 4 to 14 m/s in a free rotation range (without the brake applied). The pitch angle of the blades was variable and controlled by bevel gears. Air density, temperature, and humidity were measured with high-precision sensors.

A torque meter with 0.2 % accuracy calculated friction losses from the supports, and a tachometer with 0.1 RPM resolution monitored the rotation. To measure density, a barometric pressure/humidity/temperature sensor device was used, with a barometer with a resolution of 0.1 hPa and a relative humidity sensor; this barometer has an accuracy of 4 %, and the temperature sensor has an accuracy of 0.8 °C. Additionally, a Foucault brake with an operating range of up to 1800 RPM and a hot-wire anemometer sensor with a resolution of 0.01 m/s to measure upstream wind speed and temperature were used in the experiments. The complete setup of the test rig can be seen in Fig. 57. Numerical analysis and experimental results are compared for C_P and C_T, comparing the experimental results presented with those of Castañeda et al. (2010), who were the first to develop these experiments with this new rotor design.
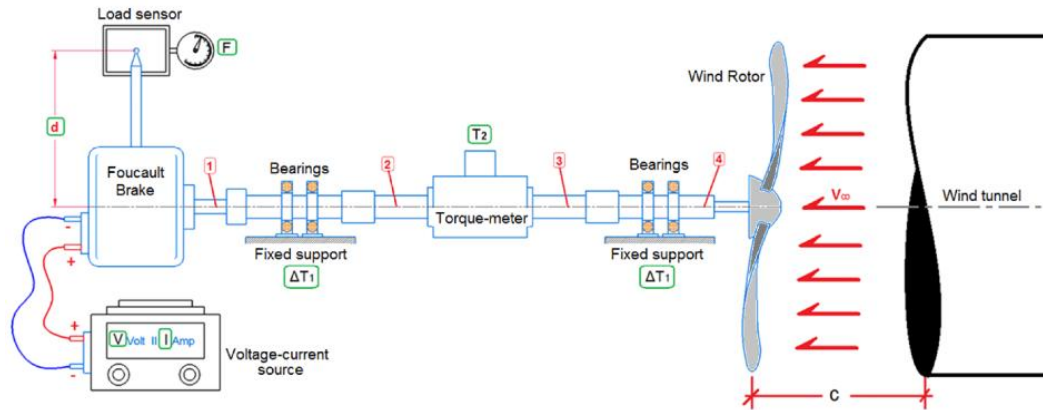
Figure 57. Layout diagram of the test bench (Gaitan-Aroca et al., 2020)

To validate the simulation results, a comparison was made with previous studies conducted by Castañeda (2010) and Wahanik (2015), which utilized both experimental and computational analyses. The experiments involved a hydraulic brake system, while the CFD analysis employed the RANS turbulence model based on Ansys Fluent® software. The simulations were conducted across a range of wind speeds from 1.5 to 15 m/s and a rotation speed of 312.5 RPM. The findings revealed a strong correlation between the simulations and experimental data, indicating that the optimal operational range for this rotor lies between 4.5 and 6 m/s.

During the simulation, an Arbitrary Mesh Interface (AMI) rotated and bounded an internal cylinder. This allowed the flow behavior to be captured, and the wind turbine's power potential evaluated to obtain a detailed visualization of vortex generation downstream of the rotor. The simulation domain was cylindrical, with two fixed meshes, and another was associated with the rotating area. The domain had global dimensions of 4R forward, 7R backward, and 5R lateral relative to the rotor radius (R). The configuration of the domain was defined as indicated in Figure 58 (Wang et al., 2012; Lanzafame et al., 2012).
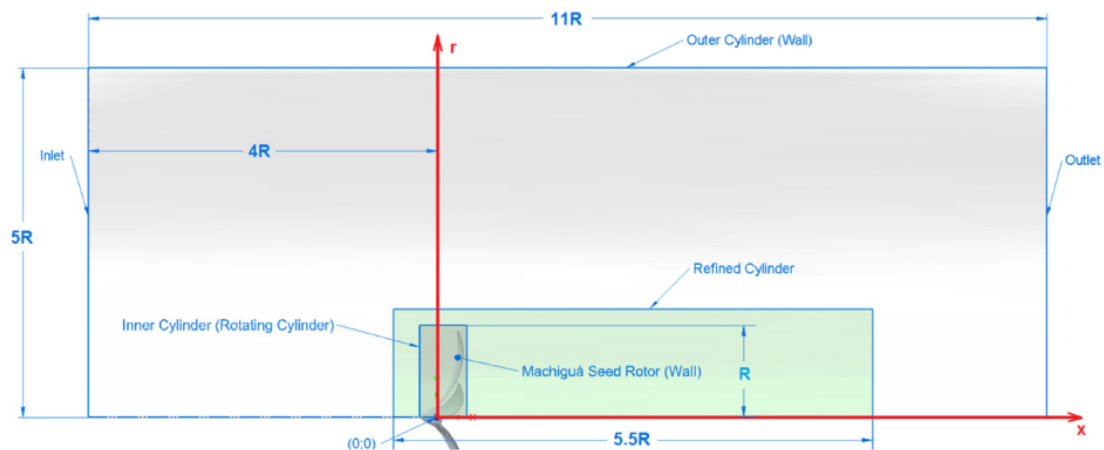
Figure 58. In the Computational Domain Scheme (units in meters), the symmetry line does not mean the symmetry limit (Gaitan-Aroca et al., 2020).

The size of the first cell of the rotor wall (y) was considered 0.04 mm. Six cells were placed over the rotor from the boundary layer, and an expansion rate of 1.1 was applied to these boundary cells (Lanzafame, 2012). The outer cylinder was not considered a wall tension function of the mesh. The complete mesh is shown in Fig. 59a and 59b.

(a)   (b)
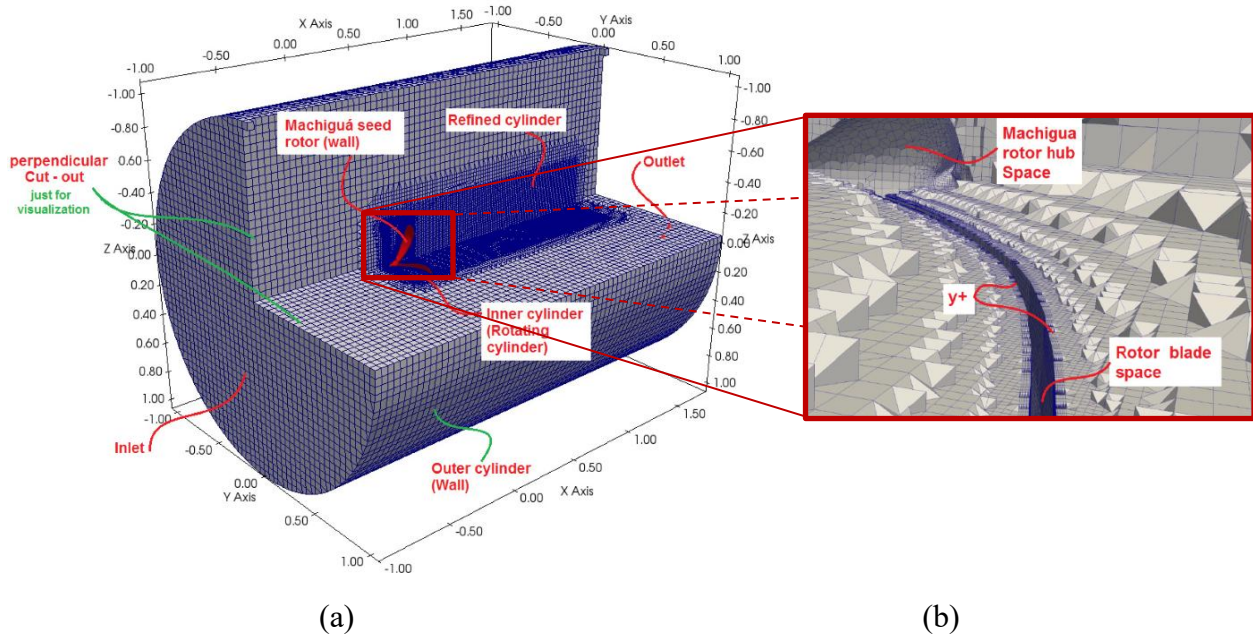
Figure 59. (a) Computational Domain of the Machiguá wind rotor (b) Details of the mesh configuration (Adapted from Gaitan-Aroca et al., 2020).

The torque results were based on a variable pitch angle of the blade from 15 to 35°. The results are shown in Figures 60a and 60b; a total of nine variable blade pitch angles were tested, and a different behavior was observed along with the results:

(a)   (b)
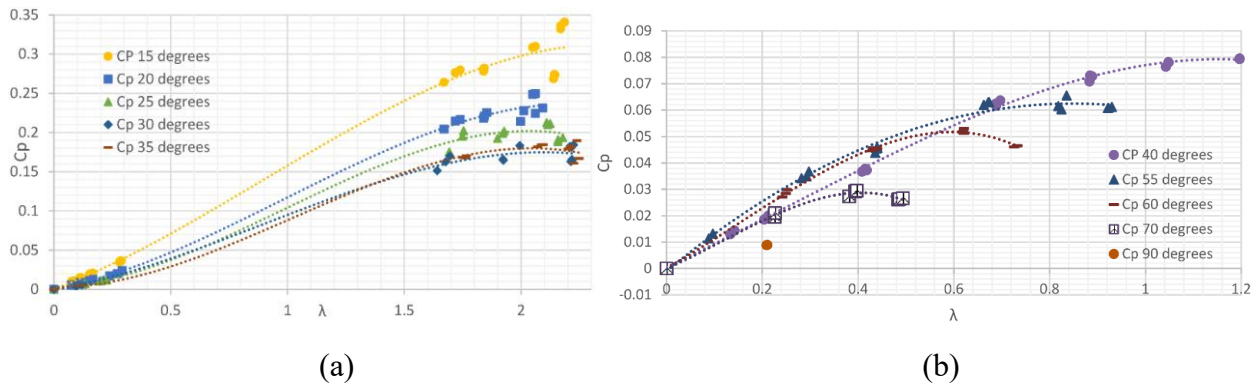
Figure 60. Cp Vs λ for different blade inclination angles. (a) from 15° to 35°. (b) from 40° to 90°. Wind *turbine P. volubilis* (Gaitan-Aroca et al., 2020).

The C_P values varied significantly with the blade pitch angle. The maximum value, around 0.32, was achieved with a blade pitch angle of 15°, remaining similar in C_P for angles between 15° and 35° at $\lambda \approx 2$. However, larger angles, from 40° to 70°, showed a considerably lower C_P. The $C_{P,max}$ decreases as the blade pitch angle increases. There were no measurements in the λ range of

0.3 to 1.6 due to a rapid change in angular velocity relative to a slight change in wind speed. This behavior is illustrated in Figure 61, which presents two distinct sections: before and after a critical point. In the first section, the angular velocity increases almost linearly with torque, with a rate of change of 1/10 for torque and 1/16.5 for angular velocity. The second section shows a sudden shift, with initial slopes of 1/6 for torque and 1/4.5 for angular velocity. Comparing the slopes for angular velocity (1/16.5 before point A and 1/4.5 after point B), it is notable that this sudden behavior affects the C_P curve, making no measured point in the related λ range.
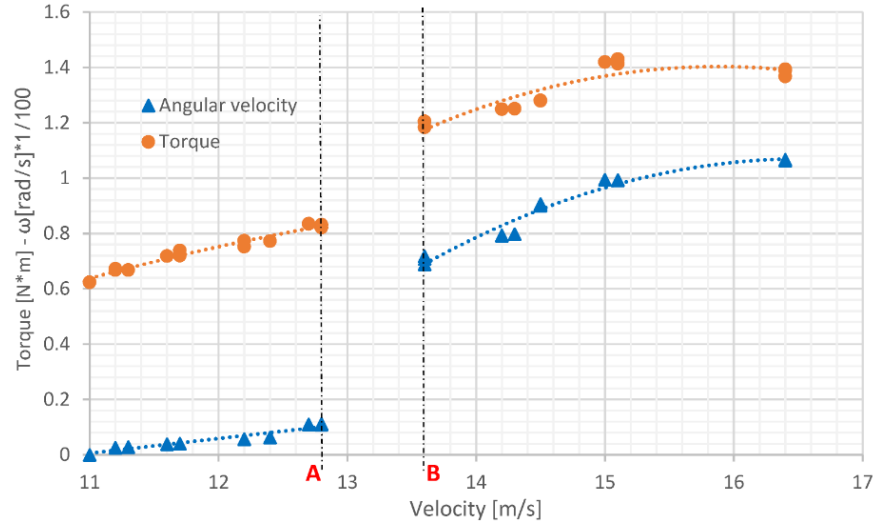
Figure 61. Torque vs Upstream Speed and Angular Speed vs Upstream Speed for a blade inclination angle of 15° (Gaitan-Aroca et al., 2020).

For the Cp curve, it is observed that $C_{P\,max}$ is obtained for a rotor blade pitch angle of 15°, which is the angle analyzed in CFD. Figure 62a shows how the extracted energy has a variable increasing rate as the airflow velocity increases. Figure 62b shows C_P values vs. TSR. Three relevant aspects can be analyzed from these figures:

(a) (b)
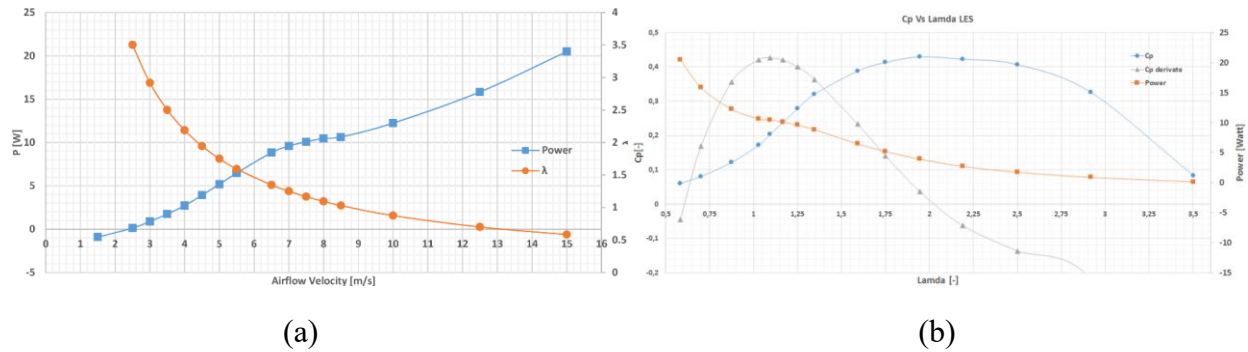
Figure 62. (a) Torque and λ vs airflow speed for machigua seeds. (b) Cp vs λ and power vs λ for Machigua rotor. An inclination angle of 15° (Gaitan-Aroca et al., 2020).

The initial power grows from 1.5 m/s to 5.5 m/s, Fig. 62a, with the maximum C_P at 4 m/s (TSR of 1.94) reaching $C_P = 0.429$, Fig. 62b. A transition range occurs from 6.5 m/s to 8 m/s, with the maximum slope of the Cp curve corresponding to TSR from 1.03 to 1.25. The range of 8.5 m/s to 15 m/s, the C_P curve starts at TSR from 0.58 to 1.03. The estimated initial wind speed for the *P*.

volubilis rotor is 2.5 m/s. Comparing the power curve and C_P curve predicted by CFD, the bioinspired HAWT reaches its maximum power faster for lower initial speeds. The C_T vs. λ curve shown in Fig. 63 has its maximum value at 1.59 λ with C_T at 0.065, not necessarily corresponding to the maximum value of C_P vs. λ. The maximum torque value is 0.626 at λ, equal to 0.58, while its minimum is 0.04 at λ, equal to 3.5. The $C_{T,max}$ curve has a C_p equal to 0.387, 9.79 % lower than the maximum C_P value, aligning with the standards of new wind turbines that require a $C_{T,max}$ below 0.2.
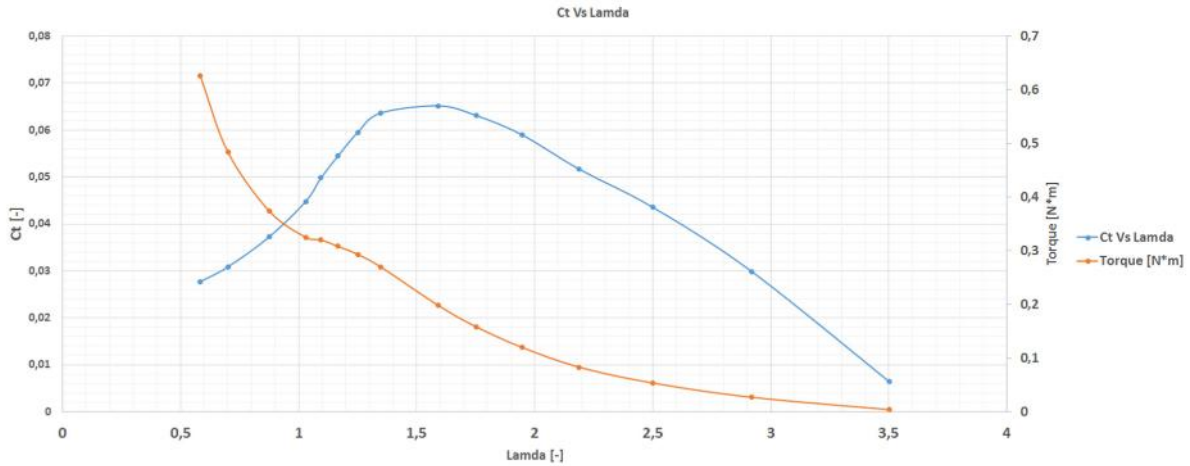
Figure 63. C_T vs TRS for Machigua seed. Inclination angle of 15° (Gaitan-Aroca et al., 2020).

The simulation results predicted the fluidodynamic performance of the *P. Volubilis* rotor on scale. Wahanik (2015) compares the computational (LES) results with previous experiments by Castañeda (2010, experimental) and CFD (Fig. 64). The results also include a comparison with another three-blade biomimetic rotor with pitch angle, the *D. aromata* seed, studied by Chu and Chong (2017), section 4.3.
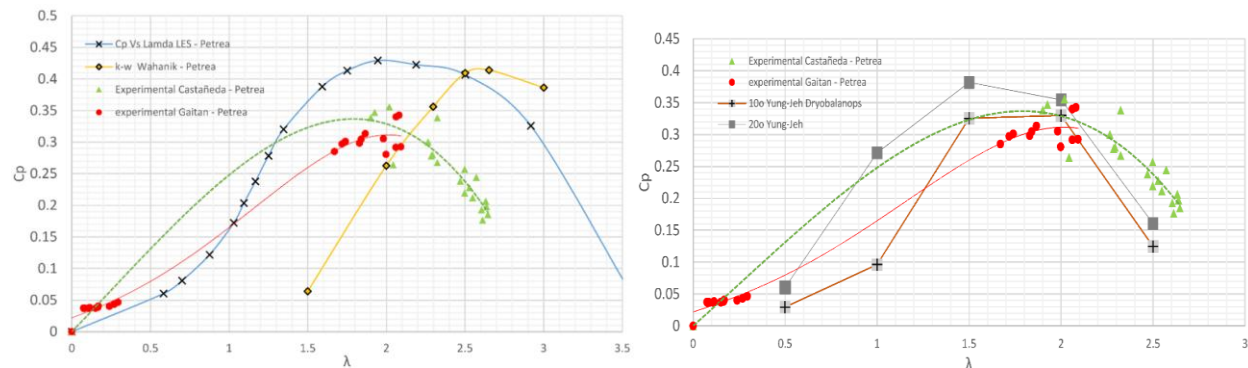
Figure 64. (a) C_P vs TSR. Tilt angle = 15°. P. volubilis seed rotor (b) Experimental results for Petrea seeds and D. aromatica 3-bladed biomimetic rotor (10° and 15° blade inclination) (Gaitan-Aroca et al., 2020).

The simulation results show that the Machigua biomimetic wind turbine rotor reached a maximum C_P value of 0.429 at λ of 1.94. The experimental results (both from Castañeda and this study) and the LES simulation results have maximum C_P in the range of λ from 1.7 to 2.6. However, there is a difference of 21 % between them. Comparison with Wahanik's results shows

similar $C_{P,max}$ with a difference of 3.54 %, but with different λ values. The *D. aromatica* rotor, a comparative biomimetic rotor, exhibited similar maximum C_P values for pitch angles of 10° and 20°, with average differences of 7.42 %. The maximum C_P value for *D. aromatica* occurred at λ = 1.5, while for *P. volubilis*, it was λ = 2. For power (Fig. 65), the CFD and experimental results coincide between 4.58 m/s (4.04 Watt) and 5.06 m/s (5.47 Watt), with differences of 2.78 % and 5.3 %, respectively, increasing with increasing wind speed, reaching a difference of 10.41 % at 7.5 m/s. There is a difference in the rate of power change in the speed range of 5.38 $<v_\infty<$ 7.44, where the CFD results have a rate of change of 1.65 compared to Castañeda's experimentation and 1.95 for the CFD results.
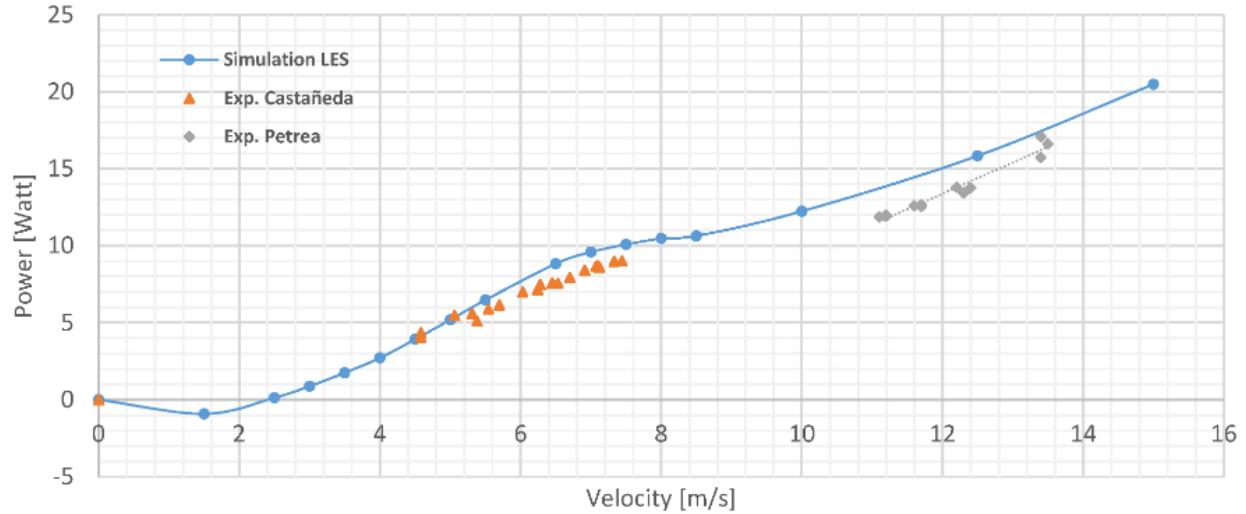
Figure 65. Power vs free flow velocity for P. volubilis turbine seeds. Inclination angle 15° (Gaitan-Aroca et al., 2020).

This study compared experiments and CFD analyses for the *P. volubilis* rotor. The experiments revealed that a blade pitch angle of 15° provides maximum performance. At the same time, CFD analyses with an LES model indicated that the Machigua rotor has potential at lower upstream speeds, significantly above 2.5 m/s (0 Watts). However, there was a 21 % difference, with a maximum C_P value of 0.35 in the range of 1.94 < λ < 2.7, between the C_P values predicted by CFD and the experimental values due to disturbances caused by the measurement device used in the experimentation.

The *D. aromatica* rotor was also compared, exhibiting characteristics like P. volubilis, especially for blade pitch angles of 10° and 20°. The maximum C_P differences for *D. aromatica* were 7.42 % lower for *P. volubilis* at the 10° angle and 16.1 % lower for the 20° angle. This suggests the Machigua rotor has potential like similar rotors at lower upstream speeds. Therefore, this study points to future investigations aimed at optimizing the cross-sectional shape of the blade, potentially improving the lift-to-drag ratio using NACA airfoils.

4.5 TRIPLARIS AMERICANA

4.5.1 Experimental analysis of the performance of bioinspired blades such as HAWT

Herrera et al. (2018) from the Pontifical Bolivarian University led the structural design and manufacturing process of a small-scale HAWT blade inspired by the geometry of the *Triplaris americana* seed (Fig. 66a), common in the Colombian flora. The study aims to optimize C_P at low wind speeds, as wind conditions in most of Colombia and the Andean regions are shallow, making energy production from wind inefficient, as no commercial turbines are designed to operate under these conditions. Initially, the research focuses on determining the free-fall velocity of 50 seeds (1.5 m/s) and their corresponding angular velocity (1,500 RPM) measured with a tachometer. In a later stage, the study presented the qualification of the airfoil along its span and the curvature of the seed (Fig. 66b) to understand and unveil the aerodynamic behavior of the seed and extrapolate such behavior to larger geometries.

(a)   (b)
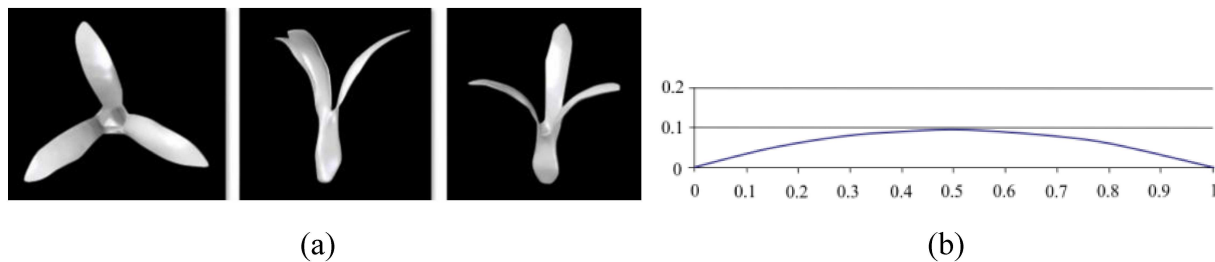
Figure 66. (a) 3D model of Triplaris Americana seed (b) Speed airfoil average (Herrera et al., 2018).

To validate the simulation method used in the aerodynamic study, a numerical validation was conducted (Correa-Álvarez et al., 2016) using experimental data from the NREL Phase IV wind turbine and comparing such data with CFD results. Although the NREL Phase IV wind turbine consists of two blades, the periodicity tools in the CFD software were sufficient to simulate only one blade, thus requiring a lower computational cost. Like the biomimetic blade, the blade was simulated under the same CFD parameters at a wind speed of 13 m/s with an air density of 1.225 kg/m³ and a pressure of 101,325 Pa. Additionally, the blade thickness was adjusted variably to preserve the balance between aerodynamic and inertial loads, increasing at the root section and decreasing at the tip section, as evidenced in Fig. 67.

Figure 67. 3D model of a Bio-inspired wind turbine (Herrera et al., 2018).

Herrera et al. (2018) developed blades with a diameter of 3.8 meters and tested them at a wind speed of 12.5 m/s, the rated speed for maximum power production. The blades' torque was calculated, producing a power of 5.1 kW. The performance coefficient (C_P) was then calculated within a speed range of 3 m/s to 13 m/s, considering a wake rotation of 2.5 m/s, as shown in Figure 68a. The power curves were calculated (Fig. 68b) for different wind turbine diameters (1 – 5 m) and wind speeds; this graph helps estimate the dimensions and operational conditions necessary to meet specific energy production requirements.

(a) (b)
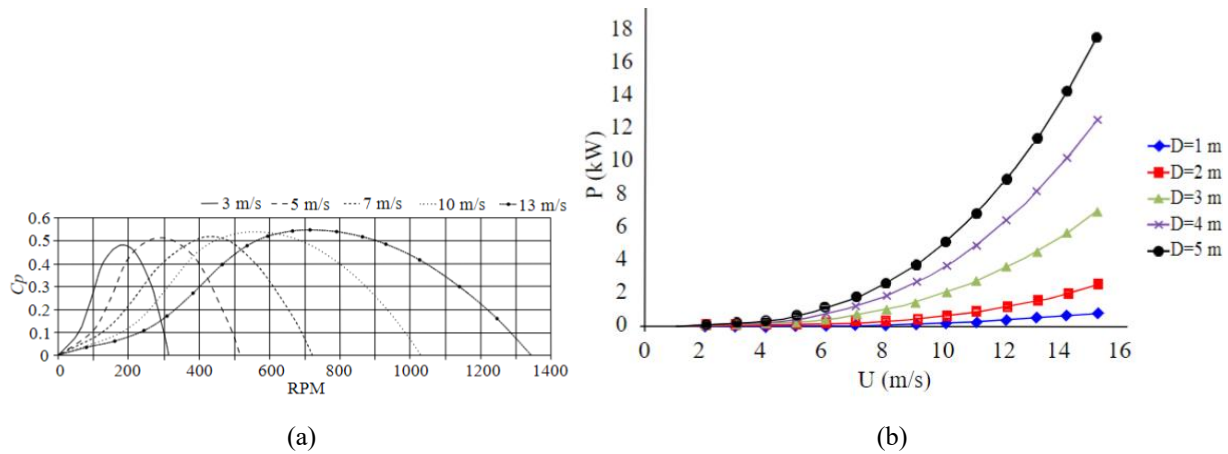
Figure 68. (a) C_P performance at various wind turbines (b) Power performance (Herrera et al., 2018).

Finally, a wind turbine prototype was manufactured to characterize the energy conversion efficiency. The model, made of carbon fiber-reinforced polymer, was assembled on a specially designed device on a bench to be moved across a wide area with near-control of stationary wind conditions (Fig. 69a). A peak in C_P close to 0.55 was achieved during the tests, demonstrating good energy conversion efficiency under natural conditions (Fig. 69b).

(a)   (b)
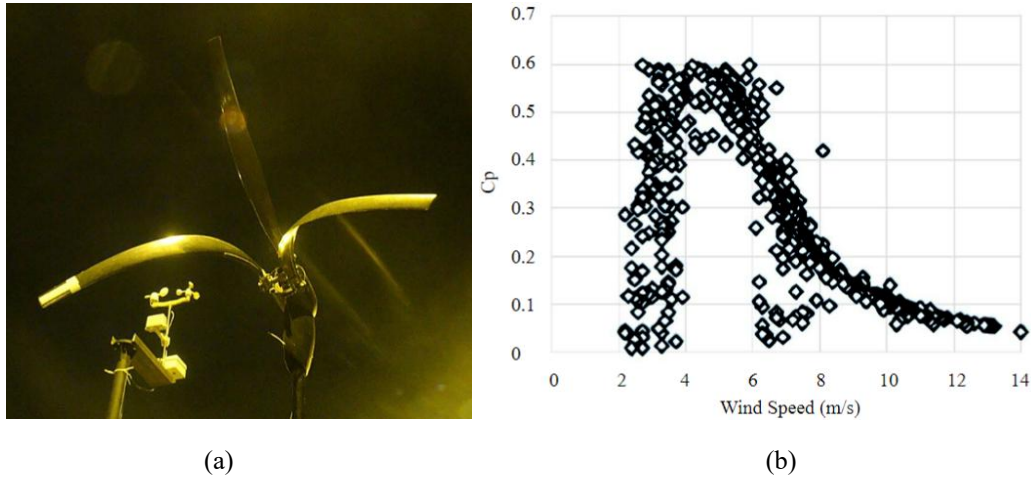
Figure 69. (a) Wind turbine test under real operational conditions (b) Experimental C_P (Herrera et al., 2018).

Different wind speeds were used during the tests (7 m/s to 25 m/s), with an average error between the experimental data and the CFD results of 4.4 %. These results demonstrate an excellent correspondence between the reported experimental data and the CFD, indicating that the simulation method is valid for conducting an aerodynamic simulation of the bioinspired wind turbine.

CHAPTER 5

5 COMPUTATIONAL ANALYSIS OF PLANE ROTORS WITH APPLICATION IN WIND GENERATORS

Computational analysis plays a vital role in designing and optimizing wind turbines. Ensuring the efficiency and reliability of these systems requires accurate predictions of the aerodynamic performance of the rotors. CFD techniques are commonly used for simulation and detailed analysis in various fields. This chapter provides a literature review of turbulence models, discusses their characteristics and limitations, and highlights relevant works in this area. It establishes the importance of the study and provides a basis for comparison of the results.

5.1 INTRODUCTION TO WIND TURBINES

The action of the turbine on the flow induces a disturbance in the region downstream of the rotor, characterized by intense turbulent mixing, helical motions, and a complex system of vortices. In turbomachinery, this region is called the wake. Much of this complexity arises from the adverse pressure gradient in the rotor plane, which contributes to the instability of boundary layers along the blades. Additionally, a spiral vortex structure is shed from the blade tips and rotor root, producing large vortex structures persist long in the flow (Silva et al., 2016).

According to Jha et al. (2015), a typical wind turbine wake can be divided into three central regions, as shown in Fig. 70:

(i)   **Near wake:** Characterized by the expansion of the wake with a further associated decrease in the mean flow velocity in the axial direction and an adverse pressure gradient due to complex vortex structures. According to Ainslie (1998), the wake widens, and the centerline velocity decreases until it reaches its minimum (when the pressure in the wake is like the ambient pressure) at around $1 - 2D$.

(ii) **Intermediate wake:** A mixing layer (shear layer) develops inside and outside the model tube. This region is also characterized by the instability of tip vortices and their merging into larger-scale structures. The end of the intermediate wake is defined as the distance downstream from the wind turbine at which the mixing layer has reached the rotor centerline. Generally, this occurs at least five to six rotor diameters downstream. In this region, turbulent diffusion begins with the interaction between the wake and undisturbed flow. The wake tip vortices then gradually lose their identity, and turbulent mixing concentrates into a shear layer, forming an annulus at the wake boundary. As a result, turbulence begins to decay (Brand, 2011; Eecen; Bot, 2013). In this region, fluid mixing dominates the wake

flow, with high turbulence in the boundary layer caused by blade tip vortices mixing with the higher speed ambient flow, generating a shear layer that expands outward and inward until reaching the centerline at around 2 - 5D (UYSAL, 2014).

(iii) **Far wake:** In this region, clustered blade vortex structures break down into progressively finer scales of non-homogeneous turbulence starting at around 5D. After this process is completed, the wake can be considered fully developed, and the recovery of velocity deficit in the center decays at a rate depending on ambient turbulence (Ainslie, 1988). Figure 70 illustrates the velocity deficit trend in the wake region, which is maximum just behind the rotor in the near wake region, decays with mixing, and reaches its minimum value in the far wake region (Sanderse, 2009; Ainslie, 1988; Crespo et al., 1999).

Figure 70 illustrates the velocity deficit trend in the wake region, which is maximum just behind the rotor in the near wake region, decays with mixing, and reaches its minimum value in the far wake region (Sanderse, 2009; Ainslie, 1988; Crespo et al., 1999).
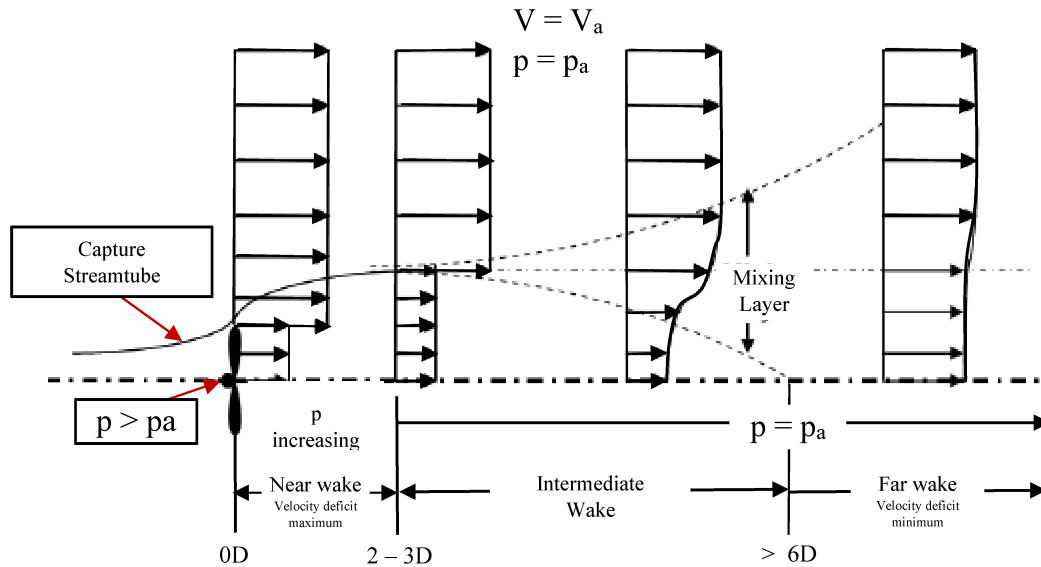
Figure 70. Schematic wake flow, D – Diameter (Adapted from Hau, 2013; Lissaman, 1979).

5.2 Turbulence Modeling in Computational Fluid Dynamics

Using computational simulation in engineering projects allows for system verification before they are even built. This drastically reduces costs associated with testing, potential failures, accidents, or inefficiencies of the mechanism, optimization, etc. Although the principles for obtaining numerical solutions have been known for over a century, it was only with the development of modern computers that numerical methods could be applied on a large scale to solve the equations of fluid mechanics, thus giving rise to the area of study known as CFD.

According to Hansraj (2019), this tool allows for the development of new methods and configurations relatively quickly and at a lower cost than experimental activities. However, the accuracy of the results depends on the models and methods employed. Therefore, commercial CFD software solutions such as EllipSys3D, Fluent, CFX, etc., have gained popularity among engineers in simulating the physical characteristics of fluid flow around turbine blades.

CFD is the analysis, through computational methods, of systems involving fluid flow, heat transfer, and associated phenomena, such as airflow analysis, through computational simulations (Versteeg & Malalasekera, 1995). The advancement of computer data processing capabilities has allowed for numerical modeling of fluid dynamic processes and heat transfer through computational modeling. Due to their high complexity, most industrial cases of interest still need analytical solutions based on the conservation equations of mass, momentum, and heat. The development of computational tools capable of describing fluid flow has allowed researchers to simulate these situations before real-world performance evaluation.

One of the most common reasons is to learn about the wake created by the wind turbine, which is used to study wind turbine interactions. Figure 71 shows the results of an example of CFD simulation of the entire upwind assembly of the HAWT within Lynch's doctoral thesis (2011). This model was likely used to determine whether a wind turbine would succeed at a given location, given wind speed and geographical conditions. Wind turbines are often analyzed using CFD models to determine wake flow patterns (Samuell, 2017).
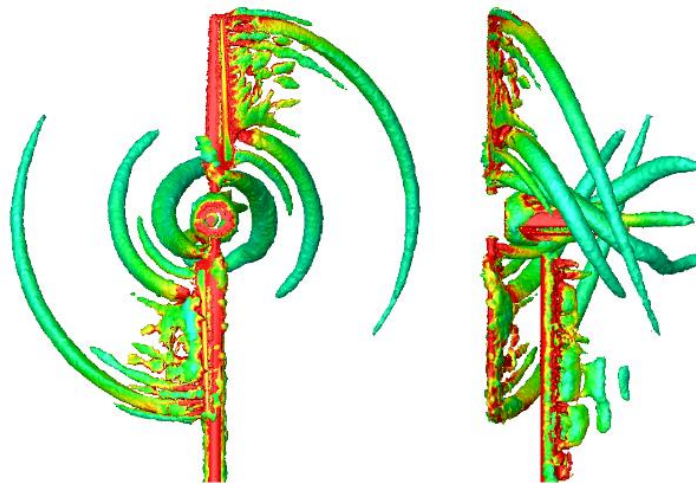
Figure 71. Vorticity of the NREL Phase VI, illustrated utilizing the Q-criterion isosurfaces for a value of 0.1. URANS computation of Lynch (2011) at 15 m/s.

It is also possible to obtain more accurate energy predictions for a wind turbine by modeling it with CFD. This can be done by examining the average wind speeds that a turbine experiences above and below the hub, as well as wind shear and turbulence, and a CFD model, can significantly assist in this type of study (Lawrence Livermore National Laboratory, 2014). Computational models are also used to optimize blade design. There are many different blade designs for turbines, and factors such as the airfoil used along the blade, airfoil chord length, twist angle, and tip geometry can be varied to optimize the design and maximize efficiency. Instead of manufacturing and testing a new blade every time a small change is made, the alteration can be

made in the model, and the resulting wake can be analyzed. Therefore, the optimization process is significantly faster and less costly.

The early uses of CFD in wind turbine performance analysis were in predicting the properties of two-dimensional airfoils. However, the increased computing power has been used at all scales, from the airfoil boundary layer to the atmospheric boundary layer (Summer; Watters, Manson, 2010).

According to Hansraj (2019), CFD is based on solving systems of differential equations governing fluid flow using approximate numerical methods and represents a particular fluid system. This is done by solving one or multiple differential equations and employing algebraic expressions to solve the unknown function by substituting existing derivatives. For cases where an analytical solution is not reached, a numerical approximation of the differential equation is performed, where the solution will be found for a given discrete number of points. The discretization of the solution implies a specific error, which can be minimized by using a more significant number of points. To calculate the infinitesimal value of the independent variables, an analytical method capable of solving such equations and presenting the solution in closed form is required (Patankar, 1980). All codes contain three main steps: (i) pre-processing, (ii) processing, and (iii) post-processing. Each of these steps is briefly outlined as seen in Fig. 72 below:
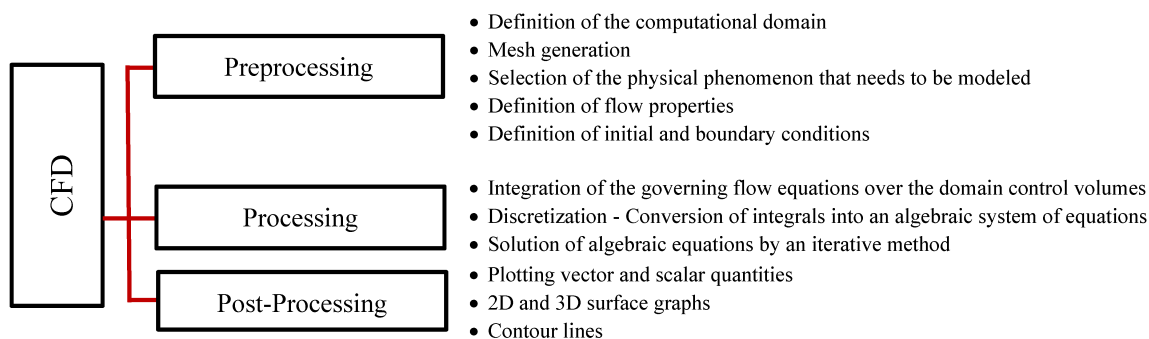
Figure 72. Summary of the elements required for a CFD simulation (Adapted from Versteeg & Malalasekera, 2007).

Pre-processing involves preparing and defining the input data for a given problem according to the actions outlined in Fig. 72. The level of mesh refinement employed will define both the accuracy of the obtained result and the computational cost of the problem. Processing is achieved by applying numerical methods that discretize and solve the flow equations. Post-processing is the stage of extracting and analyzing results through visualization, using the results obtained in the previous stage.

5.3 Governing Equations

The software uses the general Navier-Stokes equations to study turbulent flows. These equations are derived from the conservation principles of mass, momentum, and energy, including the influence of heat transfer, magnetic fields, etc.

Recently, Thé and Yu (2017) extensively reviewed and discussed the Reynolds Averaged Navier-Stokes (RANS) and hybrid RANS-LES (HRLM) methods, as well as their applications to wind turbine aerodynamics under complex flow conditions. Additionally, O'Brien et al. (2017) provided a comprehensive review of CFD codes available for wind turbine wake predictions. Here, three-dimensional, incompressible Reynolds-averaged Navier-Stokes equations are employed for fluid flow simulations. Thus, the governing equations of the flow are the continuity equations, presented in tensor notation and in a reference frame with constant velocity, which can be described as follows:

$$\frac{\partial u_i}{\partial x_i} = 0 \tag{5.1}$$

where, x_i and u_i are the coordinates of the Cartesian reference frame and the velocity components, respectively. The principle of conservation of momentum leads to the Navier-Stokes equations or the momentum transport equations, which, in the case of a reference frame with constant velocity, are given by Eq. (5.2).

$$\frac{\rho\,\partial(u_i)}{\partial t} + \frac{\rho\,\partial(u_i u_j)}{\partial x_j} = \frac{\partial \tau_{ij}}{\partial x_i} - \frac{\partial P}{\partial x_i} \tag{5.2}$$

where u_i and u_j are the velocity fields in the principal directions, P is the pressure field, t is the time, τ is the viscous stress tensor, and ρ is the mass density.

Since the fluid is Newtonian, a linear relationship exists between the rate-of-strain tensor, as shown in Eq. (5.3), and the viscous stress tensor given by Eq. (5.4).

$$S_{ij} = \frac{1}{2}\left(\frac{\partial u_i}{\partial x_j} + \frac{\partial u_j}{\partial x_i}\right) \tag{5.3}$$

$$\tau_{ij} = 2\mu S_{ij} \tag{5.4}$$

Equation (5.1) represents the principle of mass conservation, and Eq. (5.2) represents the momentum conservation principle. It is a closed system in three dimensions, with four variables and four equations.

The mass conservation equation and the linear momentum conservation equation are partial differential equations forming part of the equations governing fluid flows. However, they only have analytical solutions in particular cases, and thus, numerical methods are necessary to obtain solutions for more complex cases, such as turbulent flows.

According to Summer, Watters, and Masson (2010), the nature of turbulent flows is such that their exact solution is impossible, especially at high Reynolds numbers. However, in many cases, only the effects of turbulence on the mean flow are modeled. Although the use of extensive eddy simulations for wind energy applications is slowly increasing, most models are based on incompressible, transient, and isothermal models based on the conservation laws of physical systems: the continuity (mass conservation) and Navier-Stokes (momentum theorem) equations (Kays; Crawford, 1993).

The Navier-Stokes equations are the governing equations of fluid mechanics and are used to characterize a flow using different flow parameters such as pressure, density, and velocity. However, due to the complexity of the equations, they can only be solved by making several assumptions about the flow to simplify them to a point where they can be solved (Schluter, 2014; Samuell, 2017). This formulation is helpful in many aspects of CFD; however, it also introduces unknown stress terms that must be approximated through turbulence modeling. This modeling has some deficiencies, but can be implemented successfully with the right CFD tools and a precise understanding of flow conditions when setting up the simulation. The equations below show the incompressible form of the Navier-Stokes equations:

$$\rho \frac{D\vec{V}}{Dt} = -\nabla p + p\vec{g} + \mu \nabla^2 \vec{V} \tag{5.5}$$

where, ∇ is the pressure gradient, $\vec{g}$ is the gravitational force, and $\vec{V}$ is the diffusion term. The basic form of the energy equation is given in Eq. (5.6), where K is the thermal conductivity.

$$u\frac{\partial T}{\partial x} + v\frac{\partial T}{\partial y} = K\left(\frac{\partial^2 T}{\partial x^2} + \frac{\partial^2 T}{\partial y^2}\right) \tag{5.6}$$

Furthermore, by neglecting viscous forces, the simpler resulting equations are known as the Euler equations. More on the numerical formulation of RANS equations for CFD applications is widely available in the literature (Wilcox, 1998; Anderson Jr., 2010; Pletcher et al., 2012). Lastly, two dimensionless quantities are essential for a better understanding of the flow:

- Mach number ($Ma = \frac{V}{c}$), is the ratio of a characteristic flow velocity V to the speed of sound c;

- The Reynolds number ($Re = \frac{VL}{\upsilon}$), is a measure of (mass × acceleration) divided by viscous forces in the 'main flow' (to be defined below).

For low Mach number flows (typically 0.2 – 0.25 based on the blade tip speed), density can be approximated as constant, and the conservation of energy law becomes uncoupled from the remaining equations. Then, the first four equations, conservation of mass and momentum, form a sufficient set for the velocity vector field and the pressure (scalar).

The Reynolds number (based on the blade rotation speed at a given radius and using local chord as the characteristic length scale) does not vary much along the blade, and large turbines (say in the 2 MW class) have values of 6×10^6 and higher. This means viscous forces cannot cause accelerations in the main flow, and pressure forces must be responsible. However, this is not true in regions directly adjacent to solid surfaces (the blades), where thin boundary layers form due to viscous forces, which are of the same importance as pressure forces. This is due to substantial velocity gradients in these regions, the velocity varying from zero at the surface to the value of the order of magnitude of the "outer" flow directly outside the boundary layer. The same occurs in the blade boundary layers and regions of high vorticity, resulting from viscous forces. Therefore, for the calculation of the flow field adjacent to the blade surface, viscous effects must be considered in some way (SNEL, 2003).

According to Çengel and Cimbala (2007) and Durst (2008), CFD can easily handle laminar flows. However, it becomes impossible to solve turbulent flows in cases of real engineering applications without using turbulence models. Furthermore, a turbulence model is a computational procedure to approximate the system of equations of average flow so that it is possible to calculate a wide variety of problems. Resolving the turbulence caused by turbulence in detail is unnecessary for most engineering applications. Only the effects of turbulence are considered in the mean flow. For a turbulence model to be usable for a CFD code, it must be helpful for a wide range of applications, have good accuracy, and be economical and straightforward to perform calculations (Versteeg; Malalasekera, 1995; Menter, 2011; Celik, 1999).

Currently, there is a wide range of turbulence models available; however, three significant types of turbulence models are used in CFD: Direct Numerical Simulation (DNS), Large Eddy Simulation (LES), and Reynolds-averaged Navier–Stokes (RANS). However, despite much research in turbulence, a turbulence model can only be appropriately applied to some types of flow. Because of this, the choice of turbulence models to use depends on the physical characteristics of the flow, the type of problem to be solved, the desired level of accuracy, the available computational resources, and the amount of time available for the simulation.

The Navier-Stokes equations can accurately simulate a wide range of engineering problems, including turbulent flows, even though small and large scales of turbulence have different physical characteristics. However, it is necessary to solve all degrees of freedom of the flow, estimated to be proportional to $Re^{9/4}$. This technique is called DNS and is the most natural technique for solving turbulent flow. In DNS, the Navier-Stokes equations are discretized directly and solved numerically. The grid must be fine enough to solve the minor scales of motion, resulting in a complete, three-dimensional, transient turbulent flow field, free of any modeling, possessing

only the errors of numerical approximation (Silveira Neto, 1998). This technique is restricted to low or moderate Reynolds number flows, considering the current available computational resources, due to the high mesh resolution required for the complete resolution of the problem. With these requirements, this technique has a high computational cost (Wilcox, 1993).

The LES approach intends to separate the small structures from the large scales through a spatial filtering process in the Navier-Stokes equations, where the numerical method directly resolves the large scales, which are considered eddies containing energy. Sub-grid scale models are used for small scales. The strategy of this modeling is that the large eddies, affected by boundary conditions and carrying most of the Reynolds stresses, must be computed simultaneously with the small scales of turbulence, since they are the weakest and contribute less to the Reynolds stresses. As a result, they are easier to model and consequently have an intermediate demand for computational resources (Rodi, 2006; Costa, 2018).

Finally, among the different methods that can be used to model the flow around a wind turbine properly, the most widely used is the RANS turbulence model (Samuell, 2017). This methodology can be obtained through a set of averages of the Navier-Stokes equations and continuity. The critical element of RANS modeling is the representation of Reynolds or turbulent stresses that describe the effects of turbulent pressure and velocity fluctuations. In this technique, Costa (2018) defines Reynolds averaging as a particular case of filtering and is used to simplify sub-grid modeling. Thus, the turbulence modeling component is high, leading to a lower demand for computational resources for equation calculation.

An essential aspect of turbulence modeling that should be evaluated when choosing a model is the computational effort required to obtain solutions from numerical turbulence methods. This computational cost is usually expressed in time units, where computational resources are used to solve equations of numerical methods and provide a flow solution. Computational cost is related to the technical level of computational resources.

Thus, the time required to solve a system of equations tends to decrease in more advanced equipment with higher processing power. Although each turbulence model has its demands in terms of computational cost, the consumption of these resources varies significantly depending on the characteristics of the model. It can be observed that the higher the demand for turbulence modeling for a particular model, the lower the computational cost of its processing. Figure 73 illustrates the positioning, classification, and association of sets of turbulence models with their respective computational costs and accuracy levels regarding the degree of turbulence modeling required.
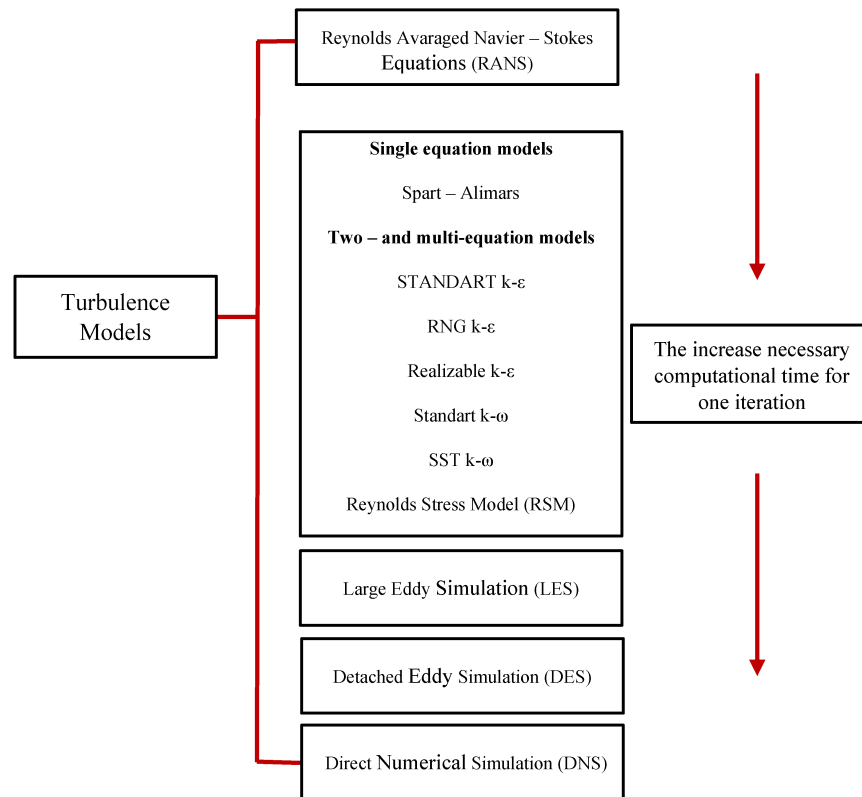
Figure 73. Turbulence models in terms of computational effort and level of accuracy (Adapted from Jaszczur & Młynarczykowska, 2020).

Although LES requires less computational power compared to DNS, it is still considered to be computationally expensive. The need for highly refined grids to resolve the scales and short-time steps in simulating transient flows results in long simulations with large volumes of information obtained. Moving on to RANS is the model where Reynold's averaging approximates the Navier-Stokes equations, and the flow field is decomposed into mean and fluctuating components (Hansraj, 2019).

5.4 Techniques for Rotational Movement

In CFD calculations of wind turbine aerodynamics, the flow domain involves rotating blades and stationary outer boundaries. To address this, three main approaches implemented in current commercial CFD solvers can be used to simulate fan rotation: the MRF model, which will be used in this study, and the Rigid Body Motion (RBM) model. With increased computational power, more advanced models like MRF are becoming more common in these areas (Dogruoz; Shankaran, 2017).

The MRF method, often referred to as a frozen rotor approach (ANSYS, 2013), is a steady-state approximation that includes various additional rotational terms in the governing equations expressed in the rotating zone (Ma et al., 2017; Shojaeefar et al., 2012; CFD SUPPORT, 2016).

The Navier-Stokes equations are solved in a rotating frame that rotates with the blade. Mathematically, the transformation from a stationary structure to a rotating structure can be achieved by two different methods. The first transformation method can be obtained through momentum equations expressed in terms of velocity relative to the moving frame of reference. The second method is obtained using velocities in the absolute frame of reference in the momentum equations (Liu & Hill, 2000). Several other methods, such as moving mesh, can model moving components.

Thus, utilizing this type of approximation and approach and transferring the velocities entering a user-defined region around the blades to a moving reference frame is achieved by Eq. (5.7):

$$\vec{v}_{MRF} = \vec{v} - \vec{\omega} \times \vec{r} \qquad\qquad (5.7)$$

where, $\vec{v}$ is the velocity in the global (stationary) reference, $\vec{\omega}$ is the rotational vector, and $\vec{r}$ is the position vector in the rotation field.

Therefore, the MRF method is often referred to as a frozen rotor approach (ANSYS, 2013) because it is a steady-state approximation that includes various additional rotational terms in the governing equations expressed in the rotating zone (Ma et al., 2017; Shojaeefard et al., 2012; CFD support, 2016). It is suitable for weak rotor-stator interaction but generally should be avoided in a transient simulation such as DES of wind turbine aerodynamics.

An important limitation of this approach is that the MRF domain defined by the user needs to be rotationally symmetric and should not contain stationary or non-rotationally symmetric parts (Dogruoz & Shankaran, 2017). Moreover, it is suitable for weak rotor-stator interaction but generally should be avoided in a transient simulation such as DES of wind turbine aerodynamics. The MRF approach is especially unsuitable for simulating flow around a Vertical Axis Wind Turbine (VAWT) (Balduzzi et al., 2016; Ferreira et al., 2010), and it isn't easy to apply for wind turbines surrounded by non-axisymmetric geometry (Rolland et al., 2013). Furthermore, the MRF model includes fan blade geometry and does not require any experimental data.

Therefore, the moving mesh approach is preferred in wind turbine applications, although it is more computationally expensive. This methodology can still be classified into sliding mesh and overset grid methods (Chimera or composite). Figure 74 illustrates the difference between the Chimera and sliding mesh methods. The Chimera grid approach involves a rotating cylinder overlaid on a stationary mesh. In contrast, the sliding mesh employs a rotating cylindrical mesh sliding along the interface separating the dynamic from the stationary subdomains (Abdulqadir et al., 2017), i.e., a computational domain can be discretized using either a Cartesian coordinate system or a generalized coordinate system (Maliska, 2012).
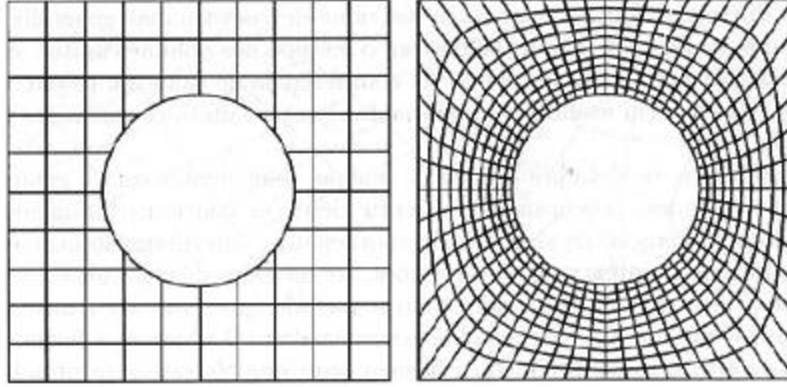
Figure 74. The representative diagram of the overset grid (left) and (right) sliding mesh method (Maliska, 2012, p. 199).

Each approach has its advantages and disadvantages. The Chimera mesh is easier to create but computationally more demanding than the sliding mesh. Both the sliding mesh method (Balduzzi et al., 2016; Kabir & Ng, 2017; Lin et al., 2016; Mohamed, 2016; McLaren et al., 2012; Wang et al., 2016; Cai et al., 2016; Lloyd et al., 2014; Lanzafame et al., 2014) and the overset grid approach (Li et al., 2012; Li et al., 2015; Zahle et al., 2009) have found numerous applications in wind turbines. The sliding mesh methodology is moderately more popular and is recommended in this work.

5.5 COMPUTATIONAL DOMAIN

The time interval used for the simulation is given by Equation (5.8):

$$\Delta t \leq \frac{\Delta x_i \, (\text{min})}{v_0} \tag{5.8}$$

where Δx_i (min) is the smallest dimension of an element in the mesh, v_0 is an average reference speed and the average time by Eq. (5.9).

$$\bar{T} = \frac{L}{v_0} \tag{5.9}$$

where L is the length of the mesh. Thus, Eq. (5.10) will give the number of iterations.

$$n = \frac{\bar{T}}{\Delta t} \tag{5.10}$$

5.5.1 Convergence criteria

As mentioned, CFD simulations are conducted by iteratively solving each mesh cell's mass and momentum conservation equations. These iterations must be repeated until the results best respect the principle of conservation in all cells. The calculation residue indicates this, for example, the difference between the mass and momentum entering and leaving each cell. The residue from all cells is combined into a single statistic (RMS – Root Mean Square), which indicates the simulation's convergence level.

Additionally, to a certain extent, the solution obtained will depend on the resolution of the grid (i.e., how many cells are in the domain). This means that a finer grid will change the results. When a solution sees no further changes beyond an accepted tolerance, it is considered "converged on the grid." When a grid is refined for convergence, the necessary flow conditions are captured according to the problem configuration. The solver's convergence to a global solution is primarily determined by the mass flow into and out of the domain and by the residual values between iterations for the main flow quantities (momentum and energy). The residual values are an aggregation of the balance of motion equations in a cell at iterations i and i + 1. The aggregation is often the maximum or global average. The behavior of residues over the solver's runtime provides information on how accurately the problem has been set up and whether a stable and steady solution is being achieved (Holden, 2015). This research used the convergence criterion that Cost (2004) and Ansys® (2009) recommended. These references advise that the RMS obtained in the simulation should be equal to or less than 10^{-4}.

CHAPTER 6

6 METHODOLOGY

The project is based on bibliographic research, focusing on readings of design procedures, dissertations, books, and publications aimed at acquiring technical competence regarding the aerodynamic design of rotors and their conception for project execution. This chapter aims to provide an overview of the experimental setups, the proposed model, and the experimental procedure carried out in this study. A detailed description of the experimental configurations, including materials, equipment, and control variables, will be presented.

To begin with, the relationship between the morphology and aerodynamics of the studied samara is investigated through a free-fall test using a method like that of Nathan et al. (1996) and Liu et al. (2020). With experimental data in hand, CFD simulations were developed to explore this issue from the perspective of turbomachinery, testing the performance of this parametric design as a wind turbine blade, like Holden (2015) and Sohn (2016).

Thus, as shown in Chapter 2, in Figs. 7 and 8, the conditions of the rotor in autorotation are intrinsically related to those of a windmill. In the autorotation state, the configuration of the rotor blades is optimized to provide maximum axial resistance to the wind while the output torque moment is kept at zero. Moderately positive tilt angles are ideal for autorotation, while negative tilt angles are more appropriate for the windmill state. This concept offers the prospect of adapting the natural design of the blades to transition between autorotation and windmill states, allowing for an efficient transition from thrust producer to torque producer. The ability to adjust the blade geometry in response to specific operational conditions presents a promising strategy for optimizing turbine performance in different situations, aligning with fundamental principles of aerodynamics and autorotation (Gessow, 1952).

Thus, based on a sample of the samara wing of *Peixotoa tomentosa*, a bioinspired blade with reduced solidity is developed to match the reference HAWT. The reason for reducing solidity is to predict the effect on its performance when the chord length of the HAWT blade is reduced, similar to Chu (2018). The following sections further explain the design and modeling methods mentioned.

Finally, the process of developing a reference blade to determine operating conditions and have a final comparison, which is used for validating computational simulations and analyzing the effects of using bioinspired geometry, is carried out. Once the operating conditions are defined, an initial geometry generated by the blade element method and Selig/Guigere profiles are created and named as a reference. Figure 75 summarizes the methodology of the work in a general way.
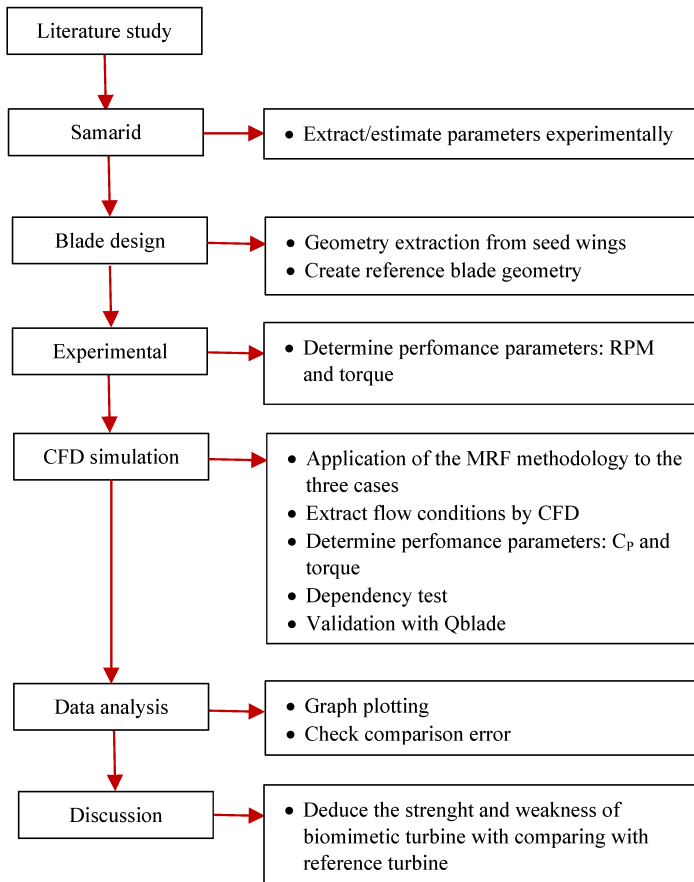
Figure 75. Summary diagram of the work methodology.

6.1 Collection and Scanning

6.1.1 Study area and plant species

The collection of samaras took place between August and September 2022 at the Ecological Reserve of Clube Caça e Pesca Itororó de Uberlândia, located in Minas Gerais, southeastern Brazil (18°59'00" S, 48°17'45" W), as part of the research entitled "Environmental variables drive phenological events of anemochorous plants and increase the potential for dispersal of diaspores: a new wind-based approach" (Novaes et al., 2020), conducted by InBio (Instituto de Biologia – Institute of Biology) in collaboration with CPAERO.

The reserve covers an area of 127 hectares, encompassing various phytophysiognomies characteristic of the Brazilian Cerrado (Appolinario & Schiavini, 2002). Samaras were collected in the Cerrado sensu stricto vegetation (Oliveira-Filho & Ratter, 2002), characterized by grasses, shrubs, and trees (Vilela et al., 2017). The climate of the region is marked by a dry season in winter (April to September) and a rainy season in summer (October to March), according to daily data

from the climatological station of the Federal University of Uberlândia (Velasque & Del-Claro, 2016).
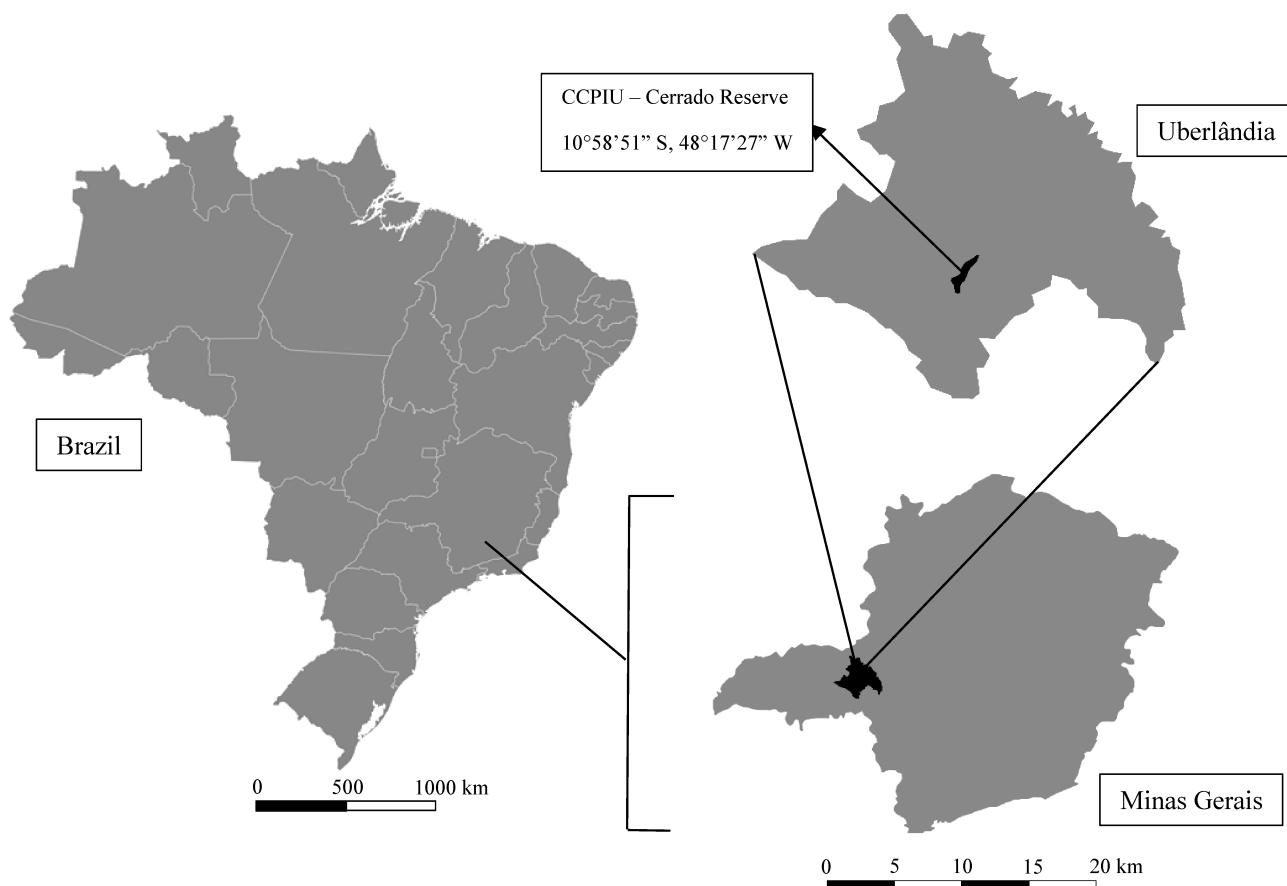
Figure 76. Localization of the ecological reserve of Clube Caça e Pesca Itororó near the urban area of Uberlândia city, in Minas Gerais, central Brazil.

6.1.2 Selection of Samarids and Characteristic Measurements

Initially, three common anemochorous species in the Brazilian Cerrado were selected: *tomentosa* A. Juss. and *Banisteriopsis malifolia* (Nees & Mart.) B. Gates (Malpighiaceae), and *Qualea grandiflora Mart.* (Vochysiaceae). The first two are shrub species up to 2 m tall, while the latter is a tree species measuring up to 5 m (Novaes et al., 2020). These focal species have a high Importance Value Index (IVI) in the Brazilian Cerrado, being part of the two most abundant families in different phytophysiognomies (Felfili & Da Silva, 1993; Bridgewater et al., 2004). Figure 77 illustrates the main characteristics of the collected plants and diaspores. Sixty intact mature samaras (N = 20 per species) were collected from four mother trees of each species. They

were taken to the Experimental Aerodynamics Laboratory (LAEX), where they were air-dried in a shaded and dry environment and stored until the experiments were conducted.
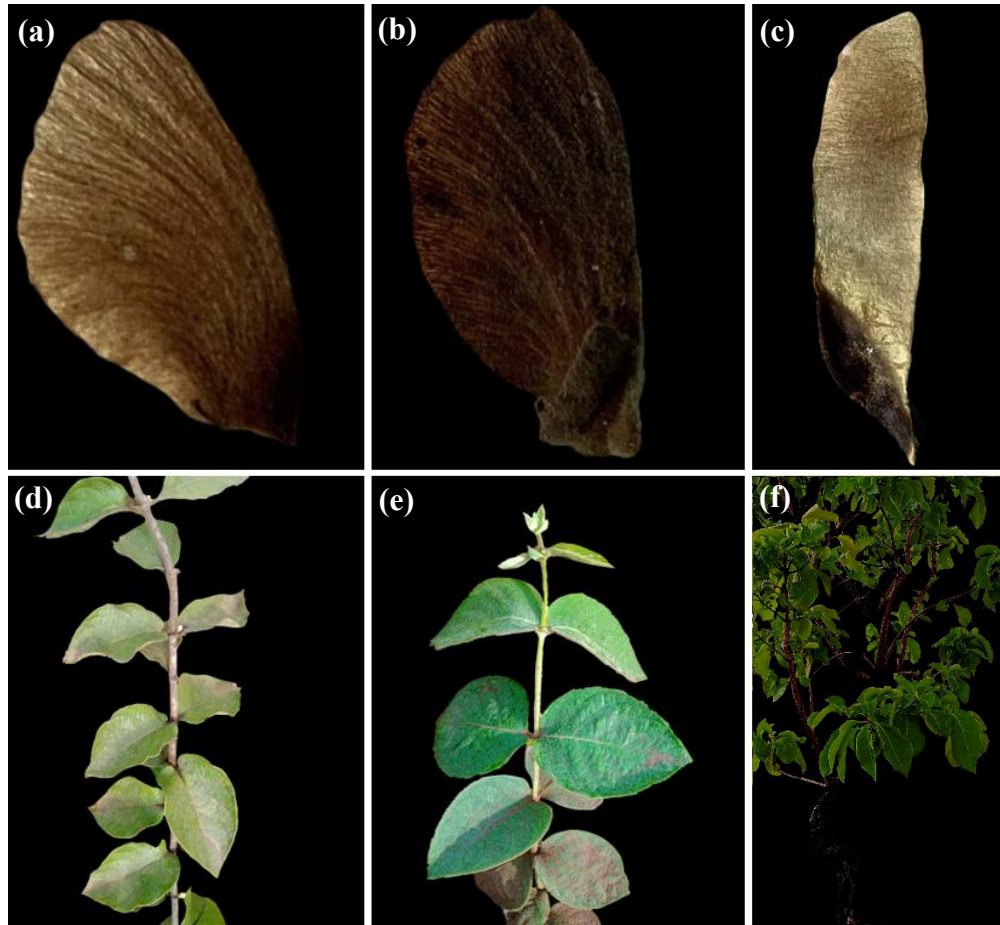
Figure 77. Samarids and their respective mother plants of *Banisteriopsis laevifolia* (a, d), *Peixotoa tomentosa* (b, e) and *Qualea grandiflora* (c, f).

To determine the natural free-fall properties of the samaras, each one was released in a still-air environment using a releaser at the top of the 250 cm tall apparatus, as shown in Figure 80. The tests were conducted in a laboratory without active ventilation interference to minimize air currents that could disrupt the measurements. Each of the twenty samaras was released once, totaling twenty drops. Finally, a square grid scale was drawn on a panel attached to the release rod to facilitate the measurement of the samaras' positions during the falls.

An iPhone 14 Pro Max camera (Apple, Cupertino, CA, USA) with a 12MP f/1.78 lens was used to record video data at 120 frames/s with a resolution of 2556x1779 pixels, sufficient to characterize the rotational motion of each seed. The flight characteristics of the samaras in steady state, including descent speed, angular velocity, wing loading, projected area, and conicity, were analyzed using a video analysis method similar to that described by Nathan et al. (1996) and Liu et al. (2020), utilizing a metric scale (± 2 cm) placed in the background. The camera recorded the vertical motion of the samara, allowing the measurement of time (counting frames) from the

moment the samara crossed the grid's starting point until it touched the releaser's "floor." In the configuration described here, this distance was 1 m. Finally, to estimate the parameters studied in this work, it was assumed that the parental types did not differ in the average release height (Guries & Nordheim, 1984).
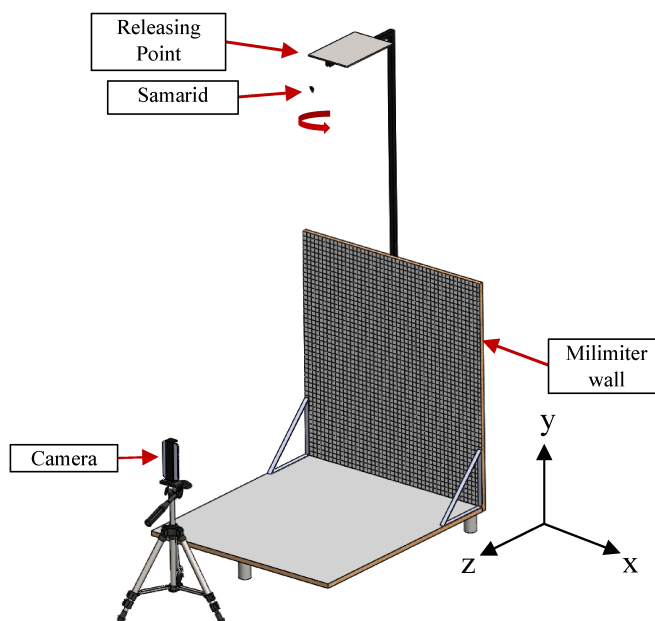
Figure 78. Configuração experimental para medir a cinemática dos samarídeos.

The terminal velocity of the samaras was statistically calculated by averaging the descent speeds of the samaras when the conicity angle became constant, estimating V_t as the mean speed in the video (Gómez-Noguez et al., 2017). Overlaying frames from each samara's release footage measured the conicity angle β. To calculate the projected area (S_p) of the samara, each was measured on millimeter paper on a flat table, and photographs were taken with a digital camera approximately 10 cm above the table. Subsequently, the photographs were transferred to a computer, and measurement data were obtained using Solidworks® software (Dassault, Paris, France, v. 2021). Two images captured in the same phase were selected and sequentially recorded for each seed to quantify the rotation rate. The elapsed time to complete one full rotation was calculated based on the number of frames between these two images.

The mass of all samaras was weighed on an analytical balance of 220g (Shimadzu, Kyoto, Japan) (0.0001 g) before the launches. The samples' span, chord, and area were measured using enlarged photographs. Wing loading is an essential indicator for comparing diaspores of different weights and sizes (Augspurger, 1986; Matlack, 1987; Andersen, 1993; Norberg, 1973), and it can be calculated as the ratio of the samara's mass to the projected area. For this purpose, descent videos were transferred to a computer to obtain the sequence of frames of the falling process of each seed with Adobe Photoshop® (CS 6, Adobe Systems Inc, San Jose, USA), as in the study by (Gan et al., 2022).

6.1.3 Airfoil extraction of the samarid

A sample of the species under study was chosen and subjected to 3D scanning performed by a metrology company using a structured light 3D scanner for computed tomography (see ANNEX D), as illustrated in Figure 79a. After scanning, the real-scale STL file containing the geometry with high-fidelity digitization was processed in SolidWorks® software, excluding the protruding region of the seed (nut/embryo protected by a harsh and dense seed coat).

Based on this information, 30 equidistant sections from the wing root to the wing tip were obtained, as shown in Figure 79b, reproducing the thickness distribution observed in the cross-sectional models of the 3D samara, in this case, the *P. tomentosa*. The resulting blade mimics the most relevant geometric characteristics of the maple seed, including the variation in amplitude scale and the profile of the trailing edge (Fig. 79c), thus making it possible to adapt it for a HAWT blade subsequently, as will be shown in section 7.2. Figure 79 compares the seed, the 3D model, and airfoil sections.

The analyzed 3D model of the samara exhibits concentrated vascular bundles along the leading edge, providing resistance to bending and torsion. The flat shape of the seed features a conical tip with a maximum chord at two-thirds of the root span. The tip section is thick, with a rough surface due to large vessels, while the trailing edge is thin. Morphological characteristics include an upward curvature, a rough surface near the leading edge, and an eccentric center of gravity at the root, considered to improve aerodynamic performance at low Reynolds numbers (Re $\leq 10^3$), thereby increasing the driving torque of the rotation shaft, as reported by Norberg (1973) and Yasuda and Azuma (1997).

(a) Once scanning is complete, an STL file is generated. → (b) 30 airfoil sections were generated from the STL file to create a solid surface. → (c) From the sections it is possible to adapt or simplify it.
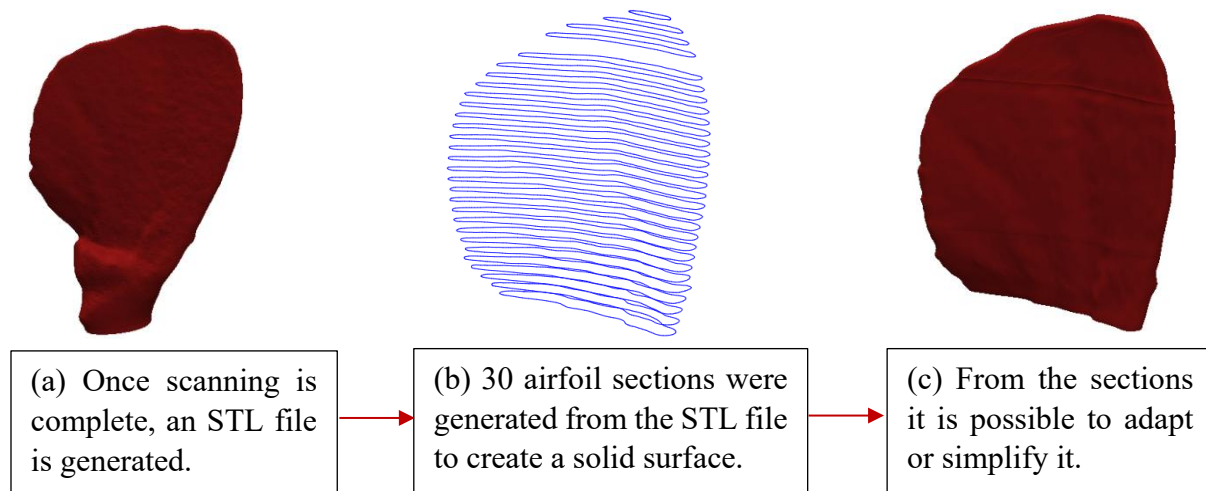
Figure 79. Step-by-step workflow (a) scanning and (b – c) post-processing the raw point clouds of data Reverse modeling.

Small wind turbines operate at low Reynolds numbers, as the laminar boundary layer is sensitive to unfavorable conditions such as adjustable pressure gradients, flow separation, and stall, which can quickly occur. Although samaras exhibit excellent aerodynamics during free fall, the

aerodynamics of each wing section differ. The design of wind turbine blades requires the selection of the most aerodynamic airfoil. Based on the results of airfoil extraction and combined with the samara's autorotation speeds, the simulation's wind velocity will be defined by the free fall test described in section 6.1.2.

6.2 DEVELOPMENT OF REFERENCE TURBINE BLADES

The software QBlade® v2.0.5.2, under the General Public License, is used for wind turbine analysis and design, enabling the prediction of its performance. The software utilizes the Blade Element Momentum (BEM) method, explained in section 2.1, for wind turbine simulation and is integrated with the XFOIL® airfoil design and analysis tool. Preference is given to turbines that do not operate at high speeds. Suppose the flow velocity values are too high. In that case, some parts of the turbine begin to operate in a transonic regime and introduce convergence issues in the software, which deviates from the objective of this study. Thus, a HAWT with SG6043 airfoil and a rotor diameter of 1.2 m was designed, subject to performance analysis by QBlade® and further analysis in Ansys Fluent R22®, as explained in section 7. Simulations in Qblade were conducted on the turbine blade at a velocity of 6 m/s, with a TSR range from 1 to 12.

Subsequently, the airfoil's lift and drag coefficient curves will be obtained and examined using QBlade®. Later, the software will define the chord and twist distribution along the blade's length using the Schmitz theory. Finally, the CP vs. TSR curve will be derived.

The blade's length will be subdivided into ten sections, each characterized by specific chord and twist dimensions. This procedure aims to develop a CAD model, instrumentalizing numerical aerodynamic analysis, as discussed in section 6.3, and experimental analysis of the blade, as explained in section 6.4.

6.3 CFD MODELING AND SIMULATION

In this work, analyses of the blades in steady-state conditions of one-third of the simplified rotor are performed, i.e., due to the processing capacity limitation of the available computer, assuming the intrinsic characteristic of rotational periodicity of the domain, the simulation will be extended to three blades, following the recommendations of Lachance-Barrett (2017), optimizing the computational cost to run the case. Several other works have used this turbine representation, and it has been argued that excluding the tower and the nacelle does not significantly influence the results (Zhu et al., 2017; Ebrahimi & Mardani, 2018; Reddy et al., 2019). The domain will be complete in the seed case, as it does not have this characteristic. Additionally, the MRF approach is used for all cases, i.e., a fixed domain and a rotational one inside it, to obtain higher accuracy results (Zhu et al., 2017) and ensure a steady-state solution.

The domain has intermediate dimensions compared to those found in the literature. Since those dimensions were validated with experimental results, it is reasonable to assume that similar, though not smaller, dimensions would also be satisfactory. The CFD domain was divided into the fixed and rotor/seed domains (rotational domain). The fixed domain consists of the wall boundary at the surface of the circular sector arc, and the periodic boundary walls at the radius surfaces are located. An interface boundary was located between the stator and rotor domain boundaries, separating the two domains. A solid part for the flow solver must represent the fluid volume. Therefore, the rest of the domain was created, and a Boolean subtraction was performed on the entire domain, leaving a cavity with surfaces representing the seed of the edge.

The coordinate system implemented for all cases was such that the positive x-axis was in the left-hand direction, the positive y-axis was in the upward vertical direction, and the positive z-axis was in the flow direction. In the case of both blades, the origin of the coordinate system was located at the center of the cube/nut so that the z-axis was the rotation axis, with the blade rotating counterclockwise. In the case of the seed, it is not perpendicular to the flow direction but placed at a cone angle θ (Fig. 80), obtained in preliminary tests, as well as the rotation rate (clockwise) and descent velocity. The inlet position was conventionally set opposite to that configured for the blade case, as in Sohn (2016).
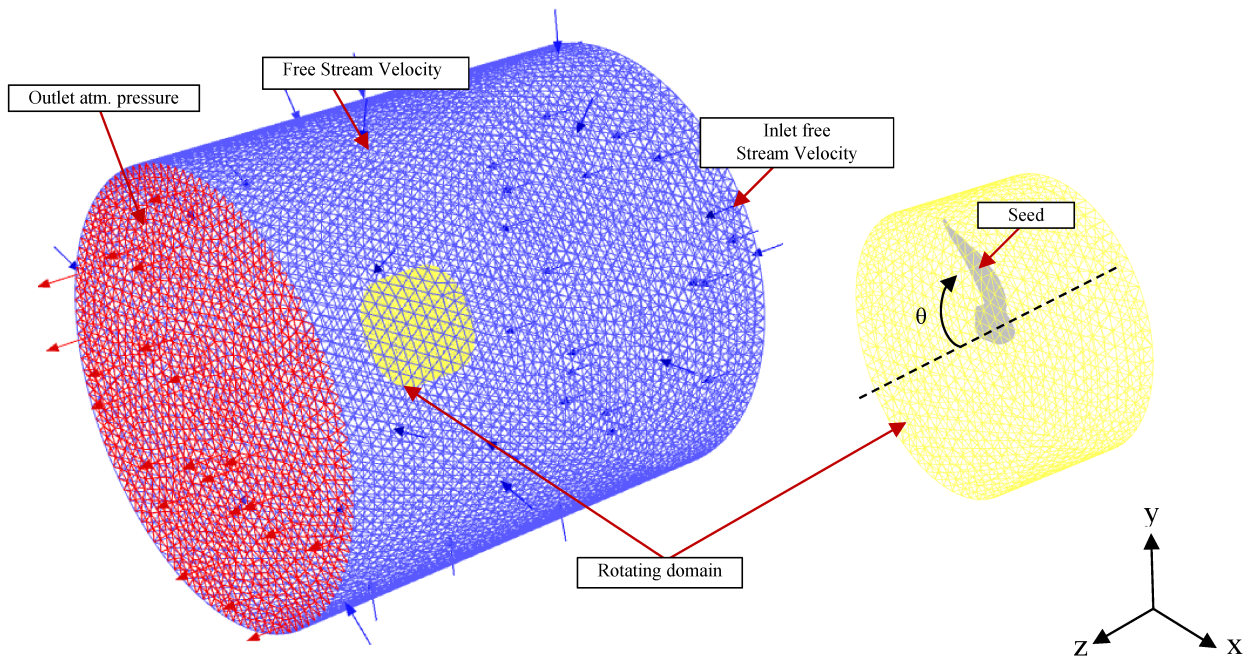
Figure 80. (a) Static domain and rotating domain around a HAWT model (b) Blade.

Basically, for all three cases (seed, biomimetic blade, and reference blade), the computational domain cylinder at the upstream inlet is in front of the seed/blade at four times the blade radius (4R), and its diameter was three times the blade diameter (3R). It was located on 7R behind the rotor blade on the downstream side with a computational domain cylinder diameter of 10R. The rotating domain has a thickness of 1.2R, 0.6R downstream, and 0.6R upstream, all

relative to the object of study radius R. These computational domain dimensions were expected to allow for wake expansion and avoid adverse boundary dependence effects. The boundary conditions are uniform velocity at the inlet, zero relative pressure at the outlet, open sides, and periodicity on the domain side.

Like the study by Ariffundin et al. (2016), for the rotating computational domain, the mesh was further refined in the blade/seed boundary layer, where the tetrahedral prism inflation mesh was implemented to create ten layers of unstructured meshes adjacent to the blade/seed. This is important to ensure that all first cells around the object of study can capture the viscosity effect.

For all cases, the domain has four main boundaries: inlet, outlet, wall, and blade/seed. The blade/seed is configured as a solid wall, the outlet and domain wall are pressure outlets, and the inlet is a velocity inlet. These boundaries are also labeled in Fig. 83. Finally, the SolidWorks®, ANSYS Meshing®, and Ansys-Fluent 2022 R1® software carried out this process. The software was chosen for its wide application and validation in turbomachinery, excellent support, and availability of student licensing.
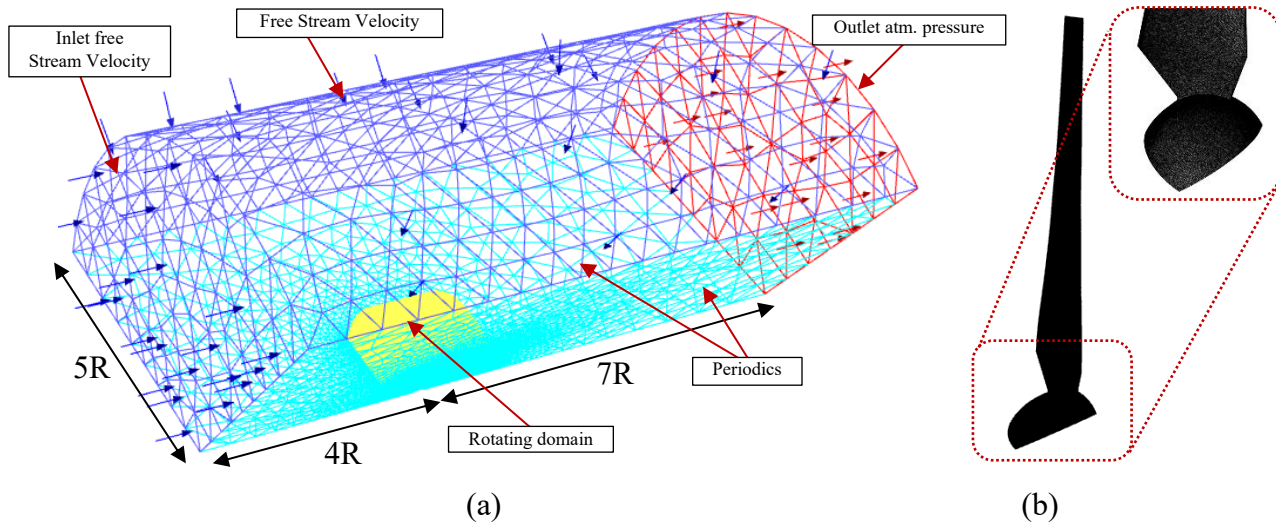
Figure 81. (a) Static domain and rotating domain around a HAWT model (b) Blade.

Finally, the boundary conditions include 5% turbulence intensity, air density of 1.225 kg/m³, kinematic viscosity of 1.46×10^{-5} m²/s, and a free-flow condition was imposed at the outlet with a relative pressure of 0 Pa, as shown in Tab. 7. For the grid convergence test of the reference and biomimetic blade, the inner zone of the cylinder was set to rotate at a constant angular velocity of 500 RPM relative to the center of the Z-axis of the computational domain and at a velocity of 6 m/s. For estimating the turbine power curve, simulations were conducted considering wind speed ranging from 4 m/s $\leq u_\infty \leq$ 12 m/s m/s with increments of 2 m/s, with Ω values ranging from 200 to 700 RPM.

The boundary between the rotating domain and the stationary region was established as an interface, ensuring a continuous fluid flow. The computational domain wall was designated as a free-slip wall condition. At the same time, the rotor and the blade/seed surface were specified as moving and non-slip walls, with the movement mode configured as follow-phase.

The Semi-Implicit Method for Pressure-Linked Equations (SIMPLE) was chosen as the numerical procedure to solve the fluid flow equations more accurately. The SST k-ω model was selected as one of the best turbulence models available for wind turbine simulation. A second-order spatial discretization scheme was chosen. Residuals of the specific dissipation ω, kinetic energy turbulence k, velocities, and continuity were limited to less than 10^{-4} during the solution process, and a maximum iteration of 1000 was selected. Furthermore, it was verified that the integral static pressure surface monitor remained constant for many iterations after convergence. The specific configuration parameters are shown in Table 7.

Table 7. Solver parameters.

Parameter	Option
Solver type	Based on pressure
Time	Steady state
Turbulence model	K- ω SST
Pressure-Velocity Coupling	SIMPLE
Residual Type and Accuracy	RMS 1.0×10^{-4}
Number of iterations	1000

The results are automatically exported to the post-processing module, where all the calculated data from the simulation is explored. The following section addresses the inspection and validation of the solution.

The rotational structure in the computational domain incorporated the rotor/seed velocity, considering the blade as a non-slip wall boundary condition. Prism inflation layers were implemented for the rotor face to optimize the flow resolution in the boundary layers, and unstructured meshes were employed in the computational domain, ensuring a wall distance (y+) less than 1. Tetrahedral elements with refinement near the rotor and 15-layer inflation aimed to maintain y+ ≤ 1, essential for the κ-ω-SST turbulence model selected due to its good agreement with experimental results. The total energy model was adopted for heat transfer, monitoring convergence through force and torque analysis. Figure 82 presents the y+ values on the seed surface, all of which are less than one.

Leeward surface

Windward surface
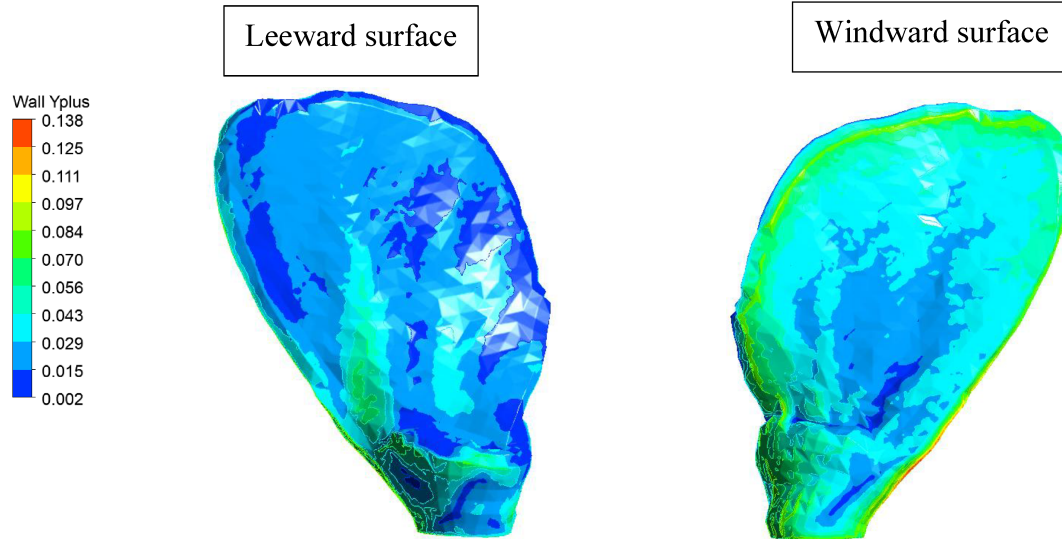
Figure 82. The y+ values at the maple seed surface are plotted as a color contour on the seed's suction (left) and pressure (right) sides.

6.4 EXPERIMENTAL ANALYSIS OF REFERENCE AND BIOINSPIRED BLADES

The experiments were set up according to the following methodological scheme presented in Figure 83, inspired by the experimental methodology adopted by Gaitan-Aroca, Sierra, and Castellanos (2020). The Torque vs. Air Flow Velocity curve, RPM vs. Air Flow Velocity, and Estimated Power vs. Velocity were constructed according to the measurement devices considered in this figure.
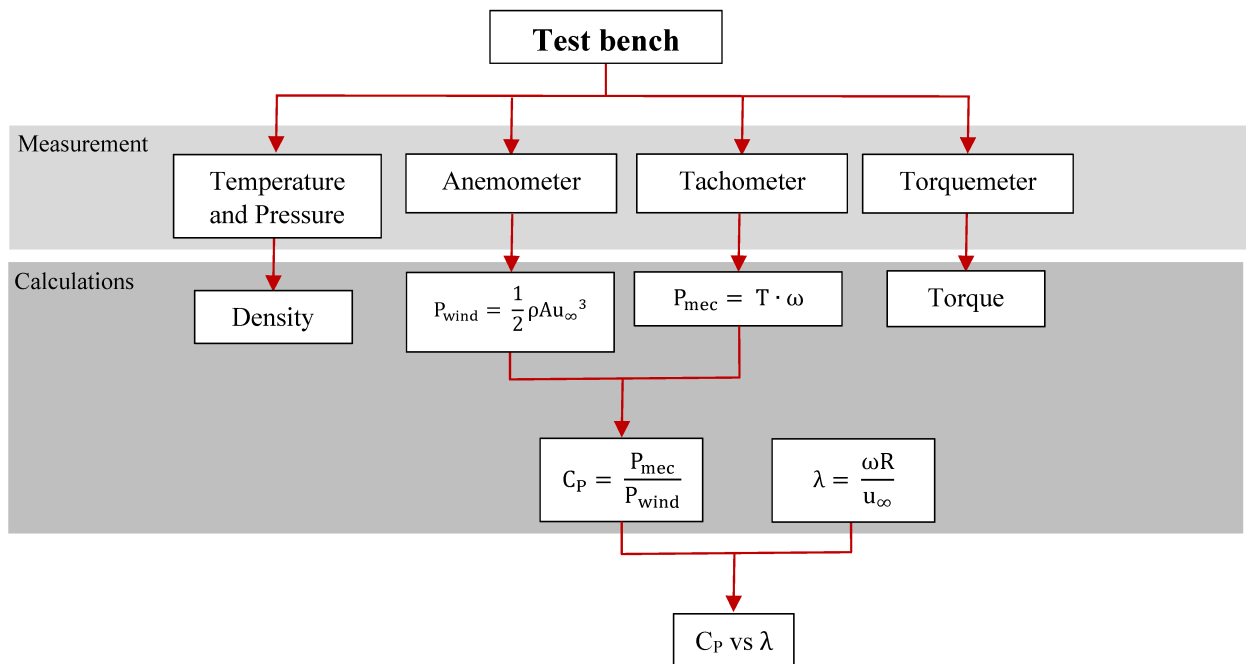
Figure 83. Schematic Measurement Method (Adapted from Gaitan-Aroca et al., 2020).

6.4.1 Experimental Facilities & Instrumentation

For the construction of the prototype, a Makerbot Replicator Z18® 3D printer provided by CPAERO was used, utilizing FDM (Fused Deposition Modeling) technology. The printing process was carried out in PLA (polylactic acid). This thermoplastic was preferred due to its high rigidity and strength, essential characteristics to withstand the aerodynamic demands of the turbine. Printing in two parts was a practical necessity due to the size of the blades. The process, in addition to requiring careful assembly, demanded considerable time and cost but provided a result adapted to the project specifications. It took approximately 240 hours to print all the blades of the wind turbine and the spinner, not considering that all the parts were finished in about a week, resulting in a total cost of approximately R$ 300.00 for printing material. Finally, the parts were assembled, sanded, painted, and treated to reduce roughness and improve aerodynamic performance.

(a)   (b)   (c)
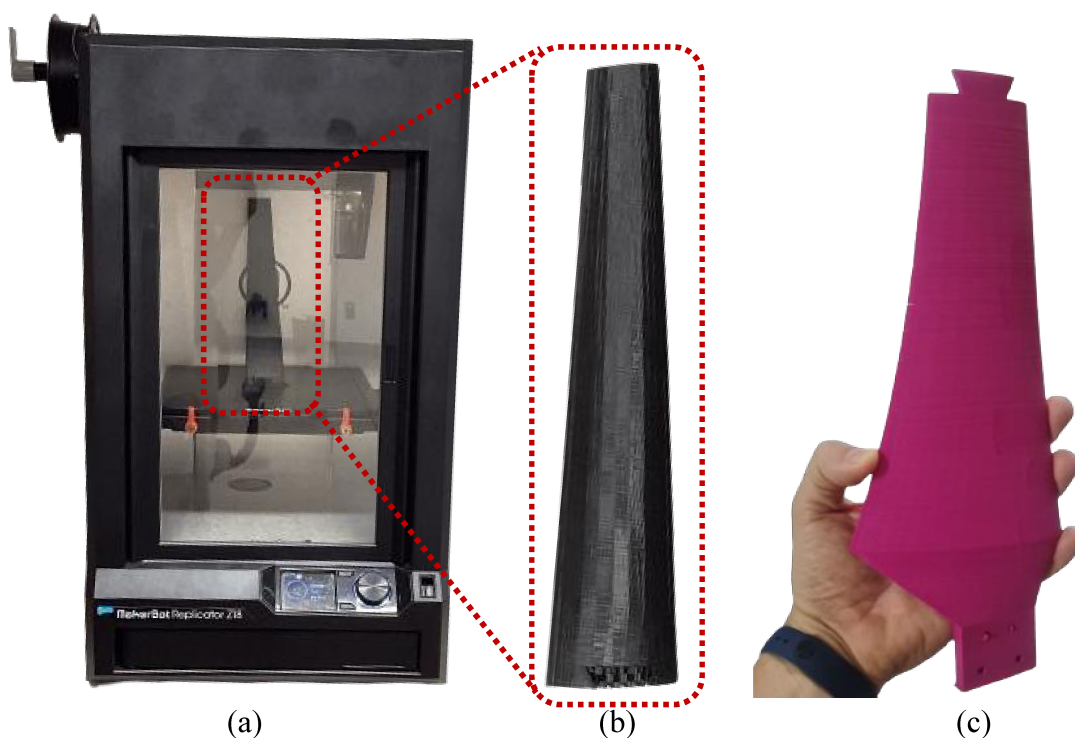
Figure 84. (a) Impressora 3D MakerBot Replicator Z18 (b) Parte superior impressa (c) Parte inferior impressa.

The experiments were conducted in the open-circuit wind tunnel with a test section of 0.6 m x 0.6 m available at LAEX, with a wind speed capacity of up to 28 m/s (60 Hz), suitable for low wind speed applications. The airflow is generated by a 12-blade rotor powered by a 25 HP electric motor, resulting in a turbulence intensity of $0.15 - 0.8\%$ across the entire speed range. Figure 85 shows the layout plan of the wind tunnel and the configuration of the measurement devices used in the test section. Additionally, considering the tip loss effect described in section 2.1, the size of the test section was increased by coupling a diffuser, expanding it to 1.69 m^2.
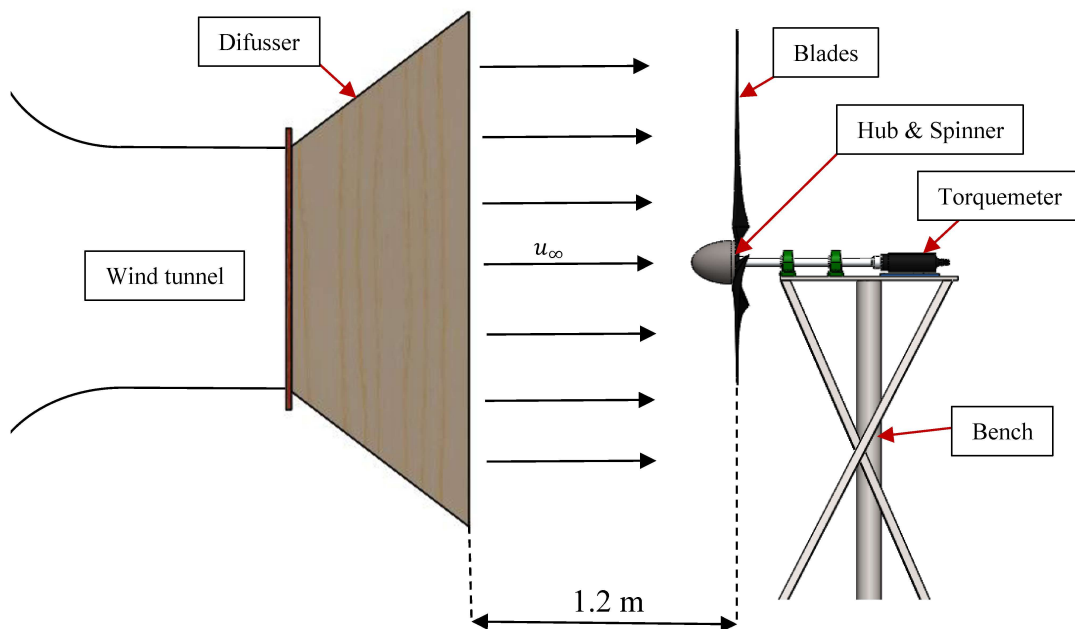
Figure 85. Schematic of a setup for torque and RPM measurements.

The pressure distribution and velocity calculation are performed using the AA-TVCR2® pressure module with 64 channels, enabling simultaneous data acquisition across all channels. This approach allows data storage according to user preference. Additionally, the pressure module offers two channels, referred to as high-side and low-side, where the high-side is related to the pressure being measured, while the low-side refers to the reference pressure. A pressure tap consists of a cylindrical tube connected to a hose, which is attached to the high-side input of the pressure module, while the module, in turn, is connected to a computer. Simultaneously, the reference pressure is connected to another hose, which is linked to the low-side input of the pressure module.
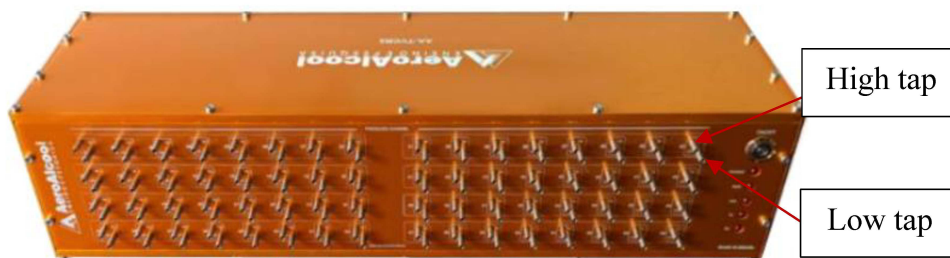
Figure 86. Módulo de pressão AA-TVCR2® (Adapted from AeroAlcool, 2021).

The air velocity was measured using a Pitot-Prandtl tube with a resolution of 0.1 hPa (Fig. 87a), which is connected to a pressure transducer (Kimo MP 200, Fig. 87b), indicating the flow velocity based on the pressure captured by the Pitot tube. A thermo-hygrometer with an accuracy of 0.8 °C (Fig. 87c) was used for ambient temperature readings. These instruments provide data such as static pressure to determine flow velocity and measure humidity and ambient temperature on the day of the experiment, respectively.

| (a) | (b) | (c) |
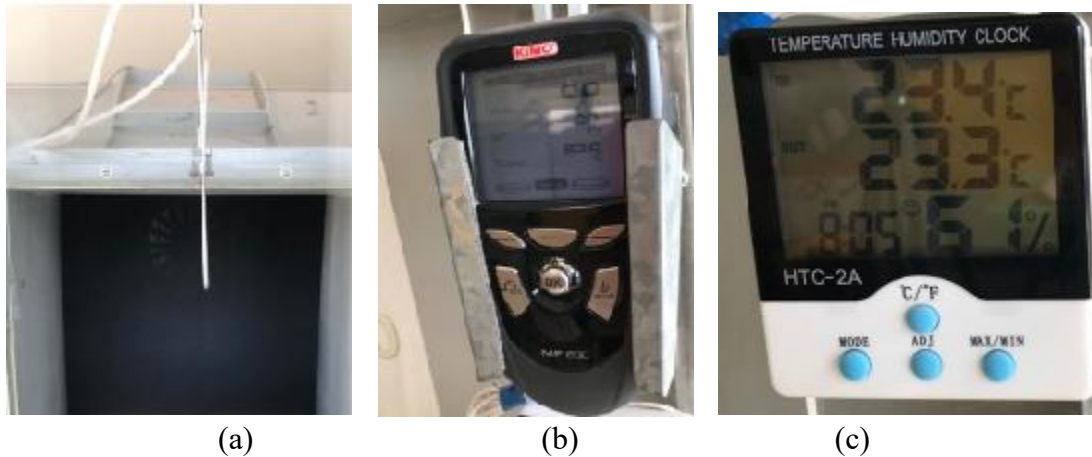
Figure 87. From left to right, auxiliary instruments are anemometer, Pitot tube, Kimo, and digital thermometer.

The power extracted from the freely rotating rotor against the flow was measured using a digital tachometer (ANNEX A) with an accuracy of ± 0.05 % and an in-line torque meter TQ-8801 Lutron (ANNEX C), with an accuracy of ± 1.5%, with the chuck attached to the turbine shaft. The complete specifications and certificate are available in ANNEX B.

6.4.2 Measures Methodology

For this study, the pressure distribution was measured to plot the velocity profile along the vertical cross-section. A device was constructed to perform pressure measurements, with the pressure module hoses connected to the pressure taps. The hoses from the pressure module are attached to a rod that varies vertically from the center of the wind tunnel up to 6 cm before the bottom wall of the diffuser. The device was positioned to occupy the central position in the wind tunnel test section.

For each pressure measurement, a reading was taken at the desired velocity to compare the values indicated on the pressure module and the Kimo instrument (Fig. 87c), validating the accuracy of the pressures. After each data collection in the module software, the wind tunnel was turned off to avoid potential errors or associated hysteresis. The procedure was repeated for each configuration.
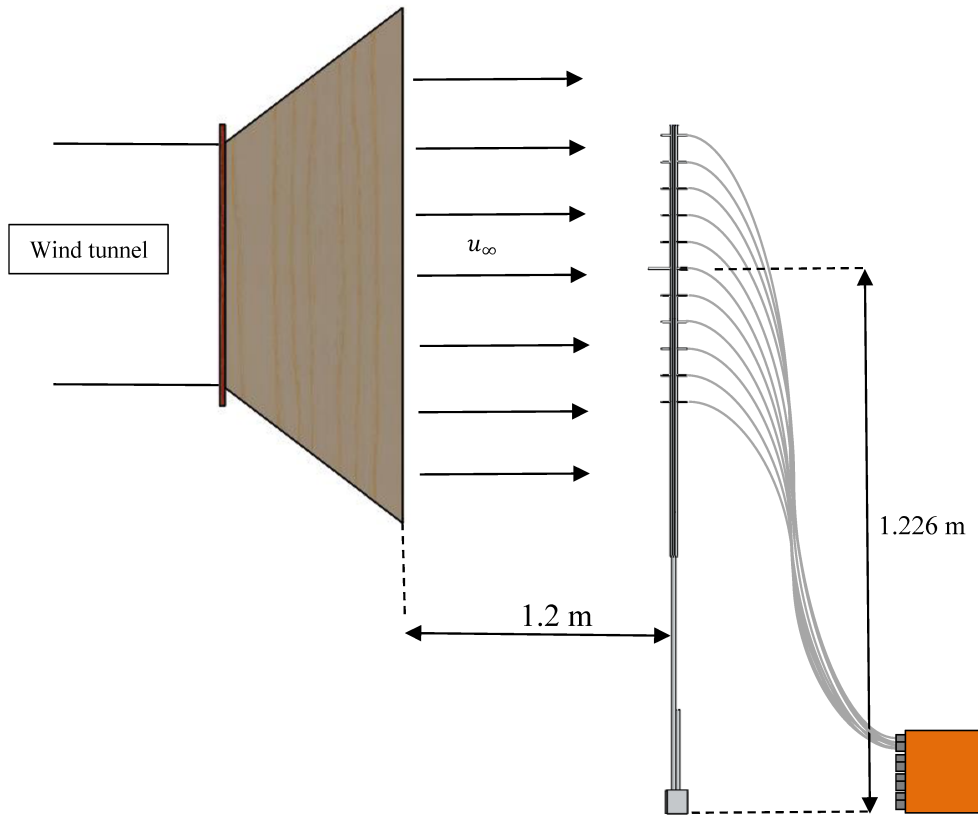
Figure 88. Measurement positions and positioning of pitot tubes.

Finally, it is essential to emphasize that the experimental investigation was not conducted as a fully operational wind turbine. Some studies, such as those by Krogstad and Lund (2012), control the rotor speed using electric motors, where the rotation speed can be defined through a frequency converter. Since our setup does not allow us to determine this operating condition, a measurement methodology like Garré (2015) was used. Thus, measurements were performed over free-flow velocities to verify the turbine performance dependency. Subsequently, these measurement points will be fitted to their respective C_P vs TSR curves to understand the blade performance in free-flow conditions.

Each static torque measurement for a given velocity results in ten distinct readings of static torque. The wind tunnel fan motor's sampling rate for the airflow velocity measurement was adjusted from 10 Hz to 28.3 Hz.

Subsequently, the turbine is detached from the torque meter to allow it to spin freely after the wind tunnel exhaust fan starts. The Uxsya DT-2234C+ tachometer emits a laser that reflects off a reflective surface attached behind the rotating blade near the base and records the measurement via a photoelectric method. In this case, the device is positioned downwind of the rotor axis and pointed towards the blades.
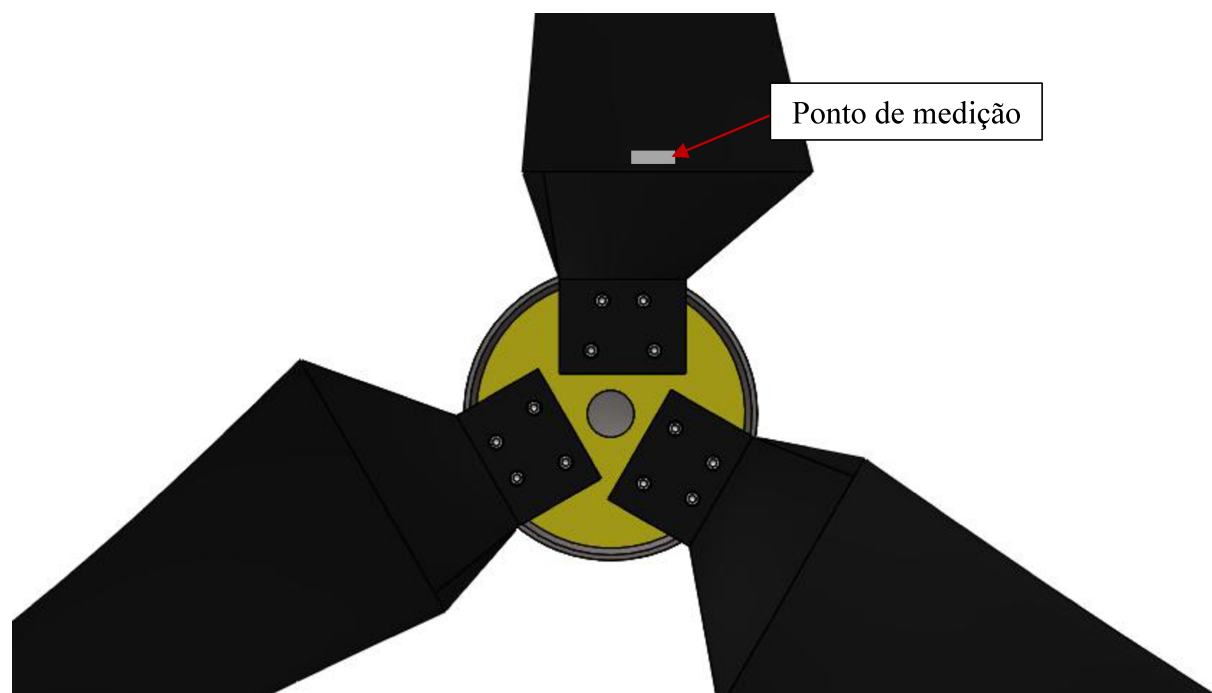
Figure 89. Location of the HAWT measurement point.

CHAPTER 7

7 RESULTS

7.1 FLIGHT BEHAVIOUR IN FREE FALL

Steady-state flight behavior varies among species, depending on the size and shape of the samara; however, the typical behavior can be described. The intermediate part of the trajectory of each falling sample was used to evaluate motion parameters and minimize any possible optical distortions. Figure 90 shows a typical overlaid image of an autorotating samara; it reaches a steady state, and its motion parameters are measured in the free-fall test.
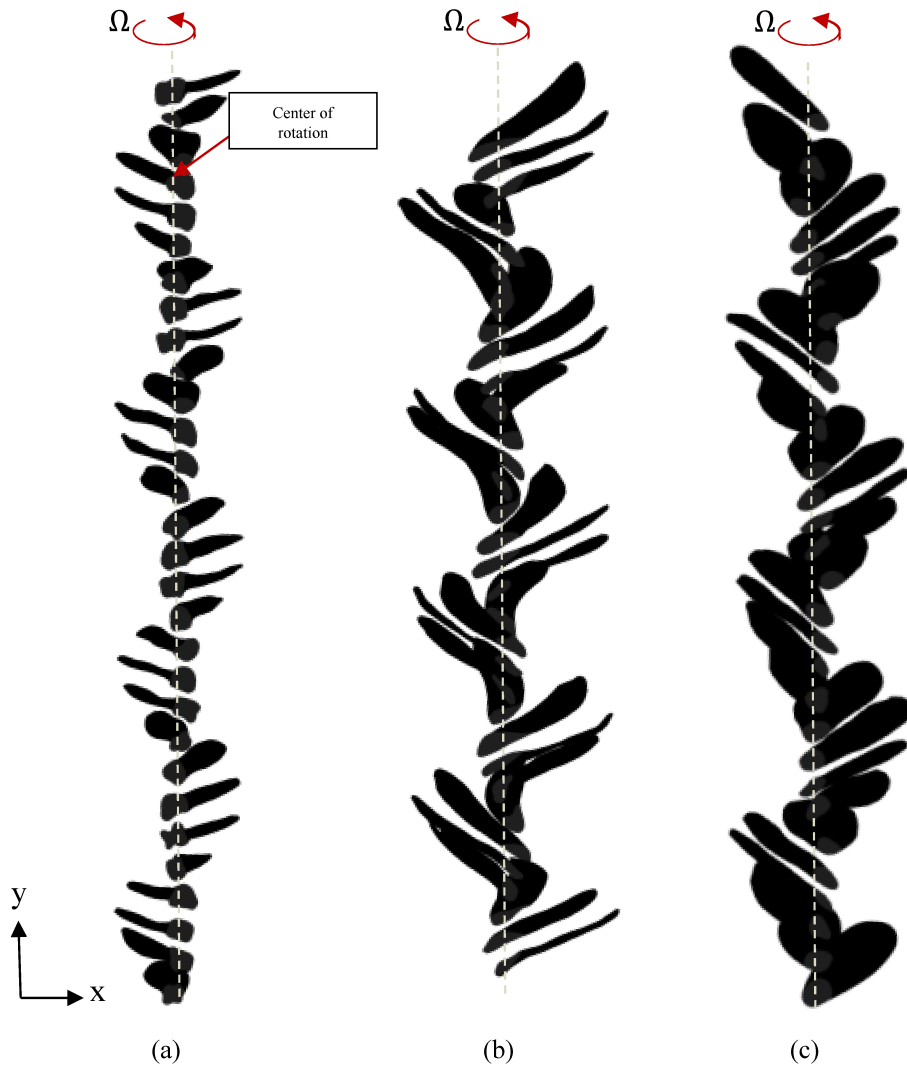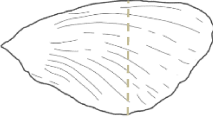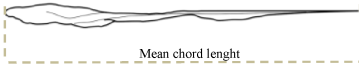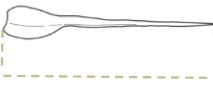
Figure 90. Overlay front view of superimposed images of samarids during free fall in stable rotation. (a) *Peixotoa tomentosa*, (b) *Qualea grandiflora*, and (c) *Banisteriopsis laevifolia*.

Considering their small magnitude, ensuring the tilt angle was challenging compared to the measurement precision of the experimental setup. Table 8 summarizes the physical dimensions and motion parameters, including descent velocity, rotation rate, and cone angle of the samples tested in this study. The motion parameters are consistent with values reported in previous studies for autorotating samaras (Norberg, 1973; Green, 1980; Augspurger, 1986; Azuma & Yasuda, 1989; Sipe et al., 1995; Azuma, 2003; Varshney et al., 2011; Lee & Lee, 2015; Lee et al., 2013; Sohn et al., 2019; Carré et al., 2022) and evidenced in Chapter 3 of this study.

Table 8. Experimental kinematic parameters were measured for the movement of samarids in three Brazilian savanna species.

Seed	*Qualea grandiflora*	*Banisteriopsis maevifolia*	*Peixotoa tomentosa*
Plan View			
Profile view			
Parameter	**Value ± STD**		
Mass (g)	0.1263 ± 0.0020	0.0430 ± 0.0008	0.0778 ± 0.0026
Descending speed (m/s)	1.65 ± 0.13	1.26 ± 0.02	2.07 ± 0.06
Coning angle (°)	26.08 ± 3.59	34.82 ± 1.32	24.60 ± 1.24
Total Wingspan (mm)	48.00 ± 0.63	28.20 ± 0.44	25.50 ± 0.59
Mean chord length (mm)	12.50 ± 0.42	15.00 ± 0.23	14.20 ± 038
Área (mm^2)	466.72 ± 14.26	279.51 ± 7.73	264.02 ± 11.40
Rotational speed (RPM)	810.00 ± 26.31	720.00 ± 20.62	720.00 ± 20.42
Aspect ratio (mm)	4.48 ± 0.18	2.78 ± 0.32	2.62 ± 0.12
Wing loading (N/mm^2)	2.60 ± 0.12	1.53 ± 0.05	2.70 ± 0.16
Tip speed ratio	0.61 ± 0.06	0.99 ± 0.03	1.05 ± 0.04

The choice of *Peixotoa tomentosa* samara over the options *Banisteriopsis malifolia* and *Qualea grandiflora* was based on its remarkable morphological similarity to seeds of *A. Negundo* (Holden et al., 2015), as well as to *A. platanoides* (Carré et al., 2022). The literature highlights the relevance of these similarities in understanding seed aerodynamics and implications for autorotation. Despite comparable results between *P. tomentosa* and *Q. grandiflora*, as evidenced in Tab. 8, *P. tomentosa* was made arbitrarily, considering the need to focus on a specific samara for deeper investigation.

With the rotating samara's physical dimensions, the seed's dynamic properties as it autorotates, and the simulated atmospheric conditions, it is possible to calculate the range of Reynolds numbers in this simulation and the TSR. Equation (3.1) is used to calculate the Reynolds number as follows:

$$\text{Re} = \frac{\sqrt{\left(75.40\,\frac{\text{rad}}{\text{s}} \cdot 0.025\,\frac{\text{m}}{\text{s}}\right)^2 + \left(2.071\,\frac{\text{m}}{\text{s}}\right)^2} \cdot 2.56 \cdot 10^{-4}\,\text{N}}{1.48 \cdot 10^{-5}\,\frac{\text{m}^2}{\text{s}}} = 2242.27$$

The calculation yields a Reynolds number of approximately 2,500. This is a deficient Reynolds number and implies that viscous forces in this situation significantly contribute more to the flow behavior than in most HAWT cases, where Reynolds numbers can quickly be about 1 million or higher. This Reynolds number places the simulation in a transitional flow regime, where the flow is laminar and turbulent. As mentioned in section 2.1, the TSR is the ratio of the tangential velocity at the blade tip to the wind velocity in the case of a wind turbine. In contrast, for the maple seed, it is the axial velocity. The TSR of a wind turbine is closely related to its efficiency and often falls in the range of $4 < \lambda < 10$, as shown in Fig. 7. The TSR is calculated by Eq. (2.31), resulting in 0.92, which lies at the lower end of the wind turbine spectrum.

$$\lambda = \frac{\Omega.R}{u_\infty} = \frac{\Omega.R}{V_d} = \frac{(720\,RPM) \cdot 0.10472 \cdot (0.0255\,meters)}{2.071\,m/s} = 0.92$$

P. tomentosa exhibits a rotation close to that defined by Norberg (1973) and Green (1980); however, it has approximately twice the speed, as stated in Chapter 3. Because of this, the species falls below the TSR range defined by Azuma and Yasuda (1989, $1.5 < \lambda < 5.5$) reported for samaras.

7.2 REFERENCE BLADE SETUP AND BIOMIMETICS

Figure 92a displays the reference HAWT, while Figure 92b illustrates the design of the bioinspired HAWT. Following the Blade Element Theory (BET) outlined in Section 2.2, both designs were segmented into ten parts, where the chord length of each part is the average chord length of the preceding and succeeding segments. For the conception of the bioinspired blade, the geometry shown in Figure 79c was adapted to have the same length and chord as the root, reducing its solidity, as depicted in Figure 91b. Adapting the geometry presented in Figure 79c for the bioinspired blade allows for the reproduction of the thickness distribution observed in the cross-sectional models of the samara, thereby conserving some of its aerodynamic properties.

In the case of the bioinspired blade, similar to Chu (2018), the rationale for adapting the samara geometry and adjusting the solidity aims to predict the effect on its performance when the chord length of the HAWT blade is reduced. In this study, this is proposed for a different type of seed, rather than the "helicopter" shape shown by Augspurger (1989) and Liu et al. (2020) in Table 1, and the inspiration for proposed HAWTs by Chu (2018) – D. aromatica, Section 4.3, and Vergara (2010) and Gaitan-Aroca et al. (2020) – *P. volubilis*, in Section 4.4, Herrera et al. (2018) – *T. Americana*, in Section 4.5, and using a self-rotating seed, as well as Holden, Caley, and Turner

(2015) and Holden (2015) – *A. Negundo*, Section 4.1, and Carré et al. (2022) – *A. platanoides*, in Section 4.2. A solidity for the bioinspired blade similar to the references was sought.
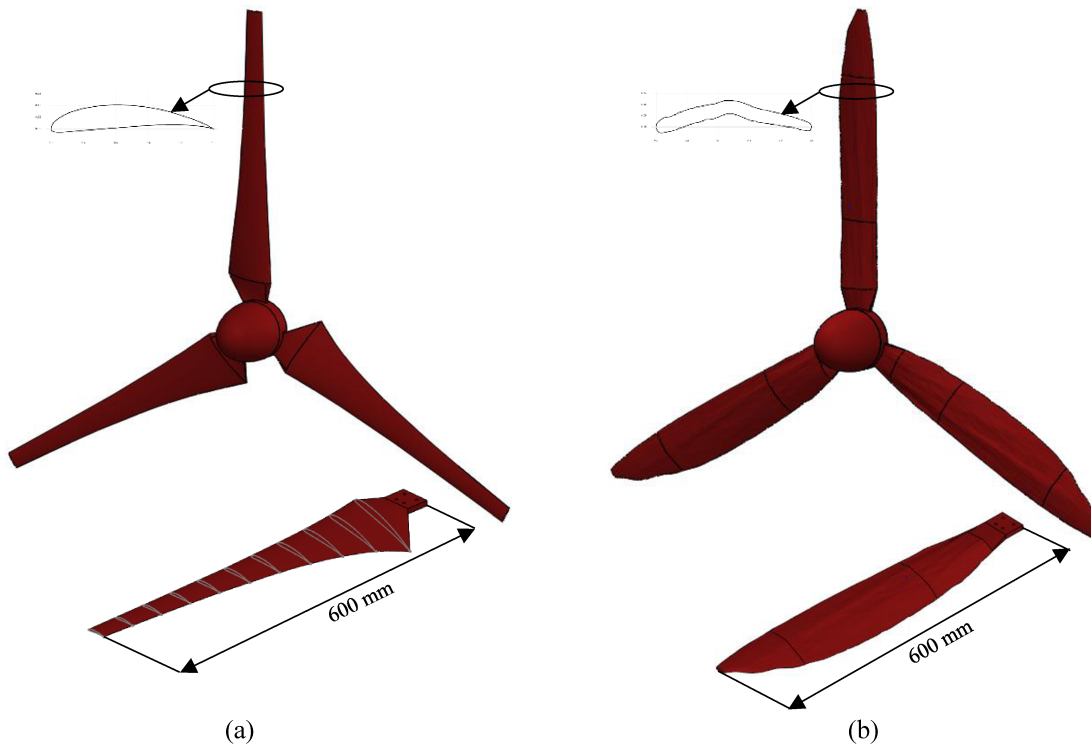
Figure 91. Geometry of (a) Standart (b) Bioinspired wind turbine model.

The choice of positioning the geometry of the bioinspired blade to obtain a configuration analogous to that of the reference was motivated by the need to ensure a more precise and meaningful comparison between the analytical results obtained for both versions. Both blades exhibit a comparable curvature line, which is necessary to pursue geometric uniformity. Geometric similarity was considered essential to effectively isolate the effects of the bioinspired modification, thereby ensuring that the observed differences in aerodynamic performance could be attributed to the bioinspired design. It is important to note that no conicity angle was assigned to the bioinspired blade.

Equation 44 determined the reference model's average solidity to be 9.7 %. At the same time, the bioinspired one had 25.1 %. This result suggests that the rotor has an intermediate solidity and that its use as a wind pump is suitable. The values align with Chu (2018), Vergara (2010), and Fig. 14.

Chamber line

(a)   (b)
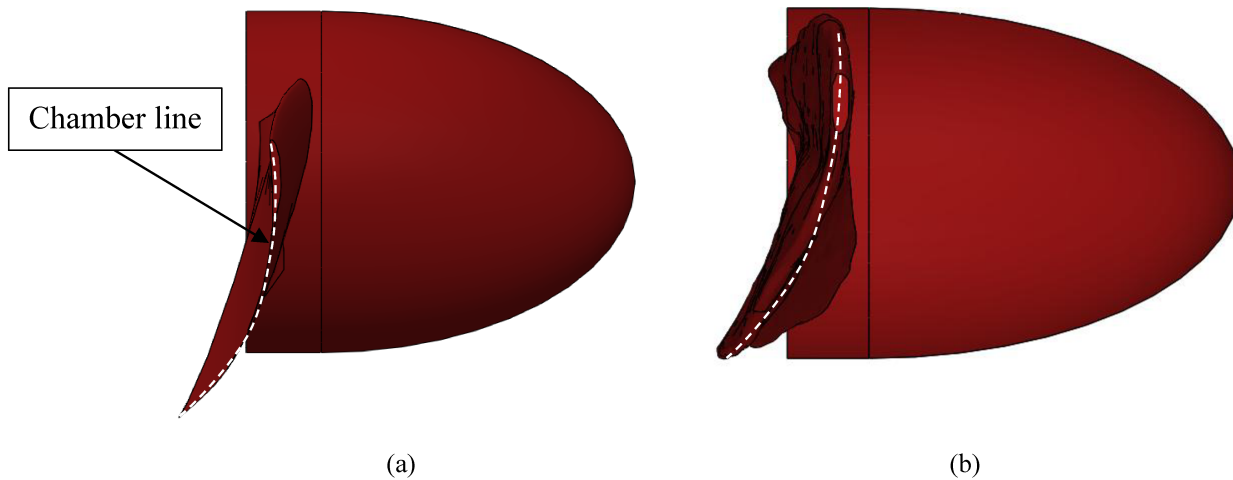
Figure 92. Top view of (a) Standart (b) Bioinspired wind turbine model.

Table 9 contains the distribution of chord, twist angle, and aerodynamic profiles along the rotor radius of the reference blade. Like the bioinspired blade, the reference blade does not have an angle of attack. It is intended to study this more thoroughly in future works, thus expecting a curve close to that in Figure 9 with β = 0° and C_P = 0.48.

Table 9. The parameter of the rotor blades.

Blade	
Radius of the blade (m)	0.6
Number of the blades	3
Airfoil types	SG6043
Nominal wind speed (m/s)	6 m/s
Angular speed (RPM)	500 RPM
Chord length (m)	Listed in Table 10
Twist angle (deg)	Listed in Table 10

Table 10. Design parameter of the blade.

Geometry of blade			
Section	r/R	Chord length (m)	Twist angle (deg)
1	0.1	0.115	20.023
2	0.2	0.094	13.345
3	0.3	0.077	9.378
4	0.4	0.060	5.856
5	0.5	0.050	3.579
6	0.6	0.044	2.533
7	0.7	0.040	1.703
8	0.8	0.036	1.028
9	0.9	0.033	0.470
10	1	0.030	0.000

7.3 EXPERIMENTAL MEASUREMENTS

7.3.1 Velocity Profile Acquisition

This section compares the velocity curves for each u_∞ on coincident graphs. Since the wind tunnel is symmetric, as shown in Fig. 93, it can reflect the measurements. After readings, the transverse profile in the wind tunnel test section is obtained. This velocity profile is determined for operating frequencies of the wind tunnel fan motor at 1.7 m/s (10 Hz), 2.4 m/s (15.2 Hz), 2.6 m/s (19.2 Hz), 5.3 m/s (24.3 Hz), 5.8 m/s (28.3 Hz), measured with the hot wire anemometer, as shown in Fig. 87a. The prototype was positioned in an area with more constant velocities (center of the channel). The graphical results of these analyses can be viewed in Fig. 93.
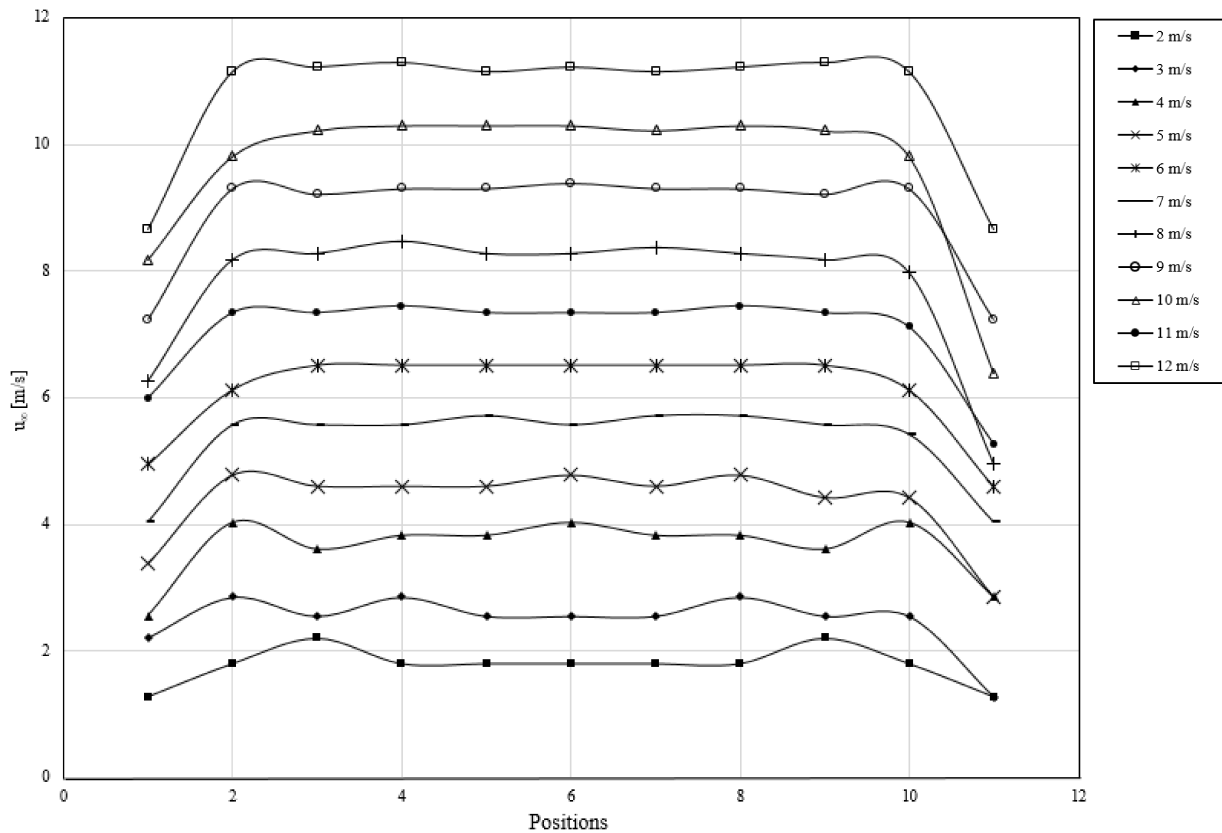
Figure 93. Velocity profiles plot.

The curves exhibit well-defined and similar behavior regardless of the velocity set in the wind tunnel. The first characteristic observed is that the shape resembles an "M," suggesting a region of more stable flow in the body's central region. After this extension, it assumes another characteristic: a progressive increase in the measured velocity with the change in horizontal position. This suggests the presence of a more active and complex flow field in that region.

7.3.2 Angular velocity and torque

Figure 94 documents the final assembly of the experimental setup proposed in Fig. 85. It comprises two P204 bearings with UC204 bearings supporting the rotating shaft coupled to a digital torque meter, precisely measuring the torque generated during the tests. Additionally, the setup features a hub that allows easy and secure attachment of the wind turbine blades, ensuring consistent replication of experimental conditions. The nosecone is also integrated into the setup.
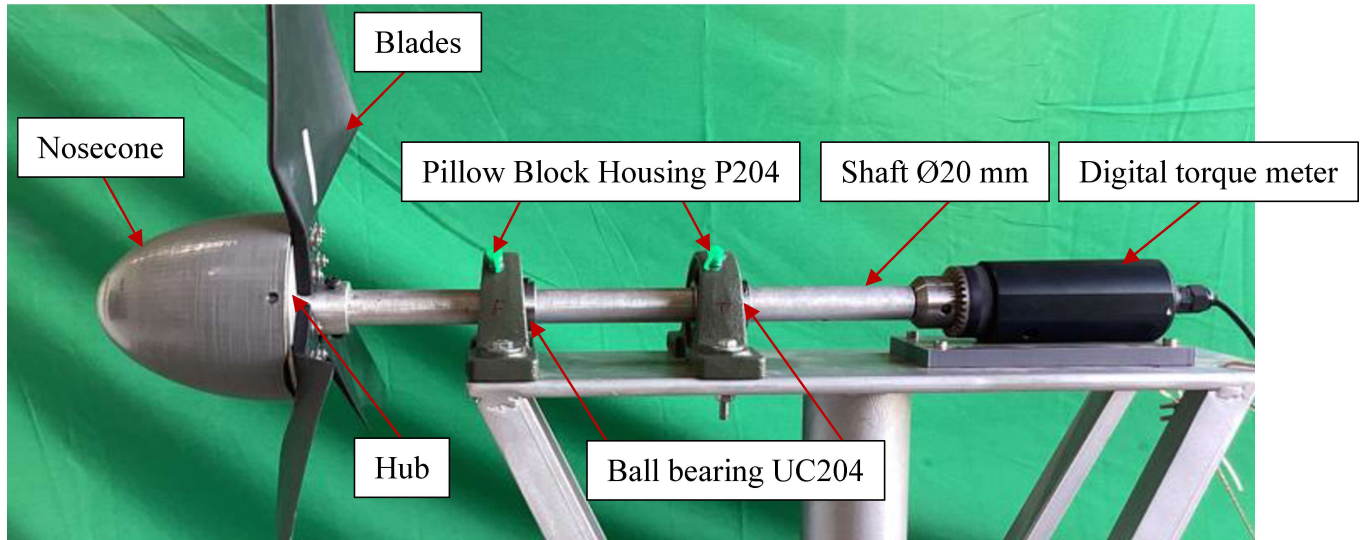
Figure 94. Experimental bench wind turbine setup.

The graphs show the Torque (Fig. 95) and Angular velocity (Fig. 96) observed about the airflow speed in free flow, showing a good agreement between both prototypes about the studied parameters.
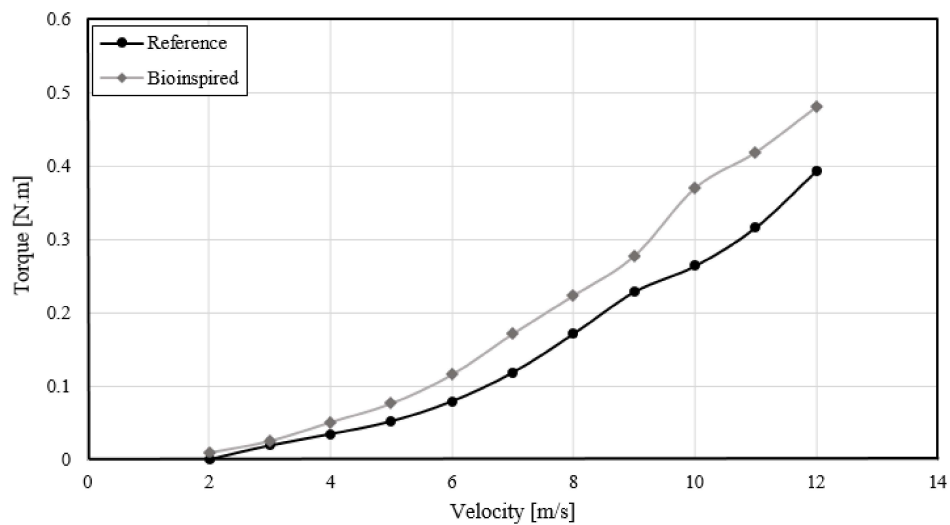
Figure 95. Toque vs Upstream velocity.

In the experiment, the blades exhibited lower torque due to the influence of the simple free-shaft system to which they were coupled. The free shaft configuration contributes to less resistance to rotation, resulting in lower opposition to the blades' movement. This behavior can be attributed to the absence of a more complex transmission mechanism that would introduce greater friction and resistance, potentially increasing torque.

By its simplified nature, the free shaft system allows for more accessible rotation of the blades, reducing the load and, consequently, generating lower torque. This observation is consistent with the expected characteristics of a free shaft system, where the absence of additional components that hinder or impede rotation results in less effort required for movement. The amount of torque measured in both cases does not contribute to power performance; however, the starting torque (torque at TSR = 0) is an important parameter because it affects the automatic starting capability of a wind turbine. A high starting torque means the wind turbine can easily overcome frictional torque. The experimental results show that the starting torques of the proposed biomimetic HAWT model are higher than those of the reference case, indicating that biomimetic wind turbines have better automatic starting capability. The reference blade has its autostart at 3 m/s with 0.0192 N.m, while the biomimetic blade has its autostart at 2 m/s with 0.092 N.m.
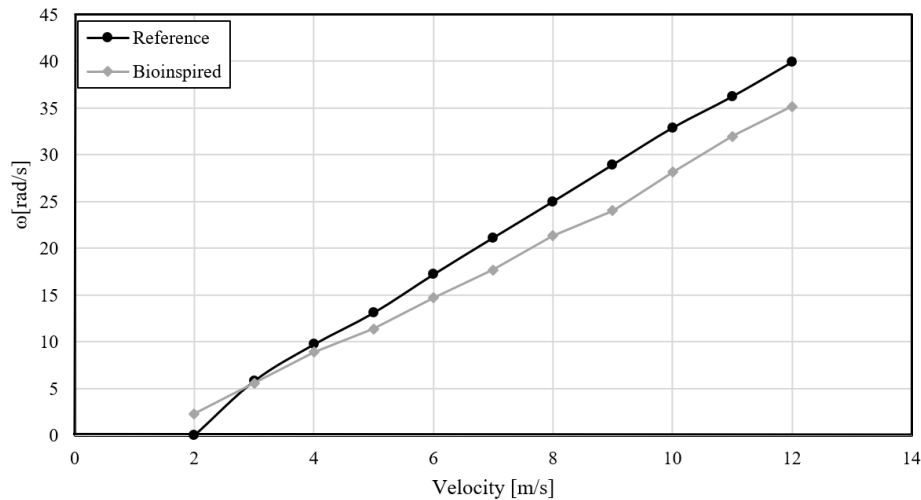
Figure 96. Angular velocity vs Upstream velocity.

A similarity in RPM values between the reference and biomimetic blades suggests a close relationship between these parameters. This similarity is crucial for CFD simulations, as it allows the adoption of the same proportion in the computational models. By maintaining a consistent relationship between rotations, simulations become more representative of the fluid dynamics observed in the wind turbine blades under study.

The congruence in RPM values implies that the aerodynamic and airflow characteristics between the reference and biomimetic blades are comparable. This strengthens the validity of the results obtained in CFD simulations, as similar operational conditions contribute to a more accurate representation of wind behavior and blade dynamics in the simulated environment.

Therefore, the proximity in RPM values provides a reliable basis for establishing initial conditions in CFD simulations, contributing to results that are more faithful to the observed reality.
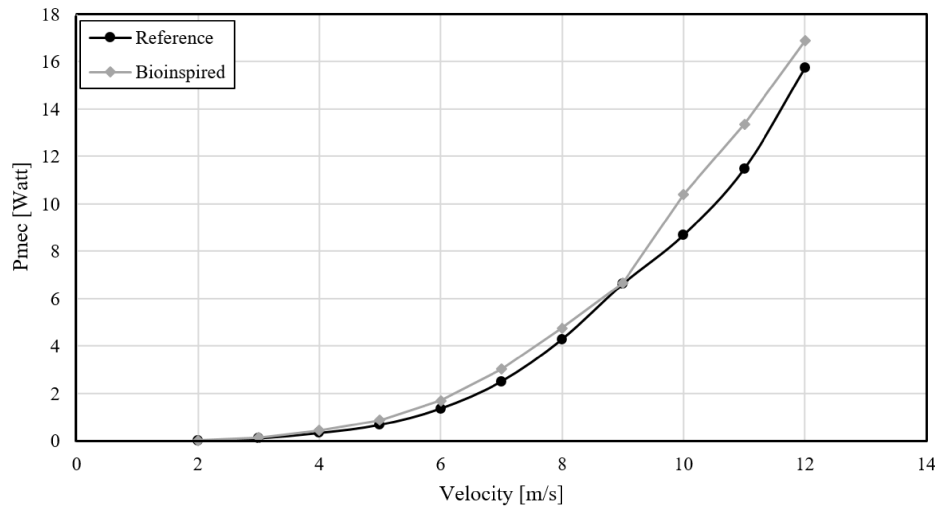
Figure 97. Power vs Upstream velocity.

The influence of the free shaft system on mechanical power values is in the direct relationship between torque and rotation speed, according to Eq. (2.21). With the free shaft system contributing to a lower torque on the blades, the resulting mechanical power, which is the product of torque and angular velocity, will also be proportionally reduced. The resulting mechanical power will be similarly affected if the torque is lower due to the free shaft system. This means that although the blades may rotate more freely, the total power generated by the system will be reduced due to the decrease in torque.

This relationship is crucial to understanding the system's overall performance, as mechanical power is a critical indicator of efficiency and power generation capacity. Thus, when considering the influence of the free shaft system on torque values, it is possible to infer direct consequences on the total mechanical power generation capacity of the set of wind blades.

7.4 CFD ANALYSIS AND VALIDATION

7.4.1 Convergence and Grid Dependency Validation

Table 11 summarizes the results of the mesh convergence study, which aimed to achieve mesh independence. It becomes evident that as the mesh becomes more refined, it positively impacts the quality; however, it also increases the total number of elements, leading to a significant increase in the computational time required for the simulation.

Table 11. Grid Convergence Study.

Blade Element Size (mm)	Number of Elements	Average Orthogonal	Average Skewness	Aerodynamic Torque (N.m)
Peixotoa tomentosa				
0.4 mm	678778	0.74373	0.2546	5.1615×10^{-6}
0.3 mm	843759	0.7442	0.2542	5.4155×10^{-6}
0.2 mm	1375423	0.7556	0.2431	5.5091×10^{-6}
0.15 mm	2093209	0.7642	0.2346	5.5457×10^{-6}
0.1 mm	3997278	0.7753	0.2235	5.6102×10^{-6}
0.08 mm	5227682	0.7789	0.2199	5.6536×10^{-6}
Reference				
4 mm	461175	0.7119	0.2727	0.687504
3 mm	655950	0.7285	0.2587	0.32424687
2 mm	1192143	0.7503	0.2404	0.35567337
1.5 mm	1928948	0.7606	0.2315	0.4708827
1 mm	3973962	0.7763	0.2182	0.44715768
0.8 mm	5927183	0.7827	0.2127	0.39295092
Bioinspired				
4 mm	151533	0.7352	0.2523	1.5177
3 mm	797015	0.7453	0.2432	1.5574
2 mm	15152967	0.7665	0.2255	1.5457
1.5 mm	2507297	0.7955	0.2021	1.3591
1 mm	5224506	0.7907	0.2061	1.3471
0.8 mm	7806187	0.7955	0.2021	1.3341

The k-ω SST turbulence model has high requirements for grid resolution near the model wall, so the nondimensional distance from the wall y must be less than or equal to 1. Therefore, the height of the first blade layer and hub surface satisfies the condition $y+ \leq 5$, while for the samarid, $y+ \leq 1$, both conditions are followed by other authors in Chapter 4. Table 11 presents a convergence study regarding aerodynamic torque to verify grid independence and, thus, be suitable for producing accurate CFD results. Seven types of grids were simulated: 500,000, 700,000, 1 million, 2 million, 4 million, 6 million, and 7 million, approximately, in the case of reference and bioinspired blades. For *P. tomentosa*, the following were tested: 850,000, 1.5 million, 2 million, 4 million, 6 million, and 8 million.

The torque begins to converge for a mesh size of 0.001 m, 0.045 m, and 0.5 m for the turbine, rotor, and stator domains, respectively. Thus, the standard blade meshes exceed 4 million for all cases. A slight difference of approximately 5 % in aerodynamic torque is observed between the refined mesh at 1 mm and 1.5 mm for the reference blade. However, there is also a significant increase in the number of elements. In the case of the bioinspired blade, there was a difference of 9 % between 1.5 mm and 1 mm, and for P. tomentosa, there was a difference of 10 % between 0.15 mm and 0.1 mm. As a result, the 1 mm surface mesh is adopted for all CFD simulations in this work in terms of computational cost and mesh quality.

The solutions of simulations that did not converge were considered converged based on the stability of the residual history, indicating a consistent response even in scenarios where standard convergence was not achieved. This alternative criterion provided a robust convergence assessment, enhancing the reliability of conclusions drawn from simulation results.

As the next section shows, the fluid flow solutions tested corresponded to experimental results at lower TSRs for the reported mesh sizes. Therefore, the same mesh properties were adopted from the validated reference HAWT case and implemented in the biomimetic HAWT cases. The simulation was executed using resources from LAEX at the University of Uberlândia. A Workstation with an Intel® Core™ i7-3930K CPU @ 3.20GHz, Windows operating system with 6 CPU cores was used for execution.

7.4.2 Seed's flow pattern

As previously stated, the autorotative flight of P. tomentosa is numerically simulated based on the 3D geometry and the motion parameters of natural seeds, as listed in Tab. 7, section 7.2.1. Observing 2D airfoil sections along the seed rotor provides more tangible evidence of autorotational behavior. Thus, it is possible to observe a crossflow formed over the lee surface of the seed blade (Fig. 99) and the transport of vorticity in the Leading-Edge Vortex (LEV), which governs the lee region of the seed (Fig. 100) in three cross-sectional shapes.

Firstly, some integrity checks on the solution are necessary to ensure that the results are close to the expected ones before proceeding with the qualitative analysis of fluid behavior. As shown by Norberg (1973), Fig. 22, in his study of samara autorotation flight mechanics, the contours of static pressure on the pressure and suction sides of the samara are a good indicator that it is functioning as a turbine rotor. Figure 99 shows similar pressure contours for the dimensionless pressure coefficient, enabling comparison through the RANS solution.
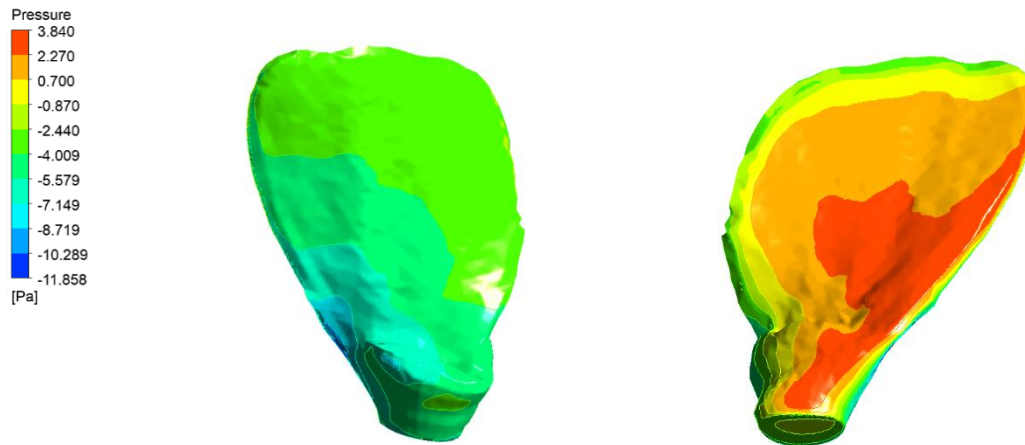
Figure 98. Surface pressure contour of *Peixotoa tomentosa*.

The highest suction pressure occurs mainly in the narrow region near the leading edge, approximately a quarter to three-quarters of the chord length. This corresponds to the location of the solid and compact Leading-Edge Vortex (LEV), in agreement with Holden (2015), Fig. 29, and Sohn et al. (2019). Due to its asymmetry, the leading edge influences the rotation axis so that almost the entire embryo/nut rotates opposite the blade rotor, contributing to torque and drag in the tangential direction.

As shown in Fig. 100, the prominent formation of the LEV on the inner extension of the chordin is highlighted at positions 0.25R and 0.5R, generating considerable suction pressure on its lee surface. The highest pressure occurs near the leading edge, influenced by the seed morphology. This high-pressure region explains how seeds maintain autorotational performance, even when most of the blade is damaged. At the 0.5R position, the LEV is less intense than at 0.25R, while they are even smaller at the 0.75R spanwise position.
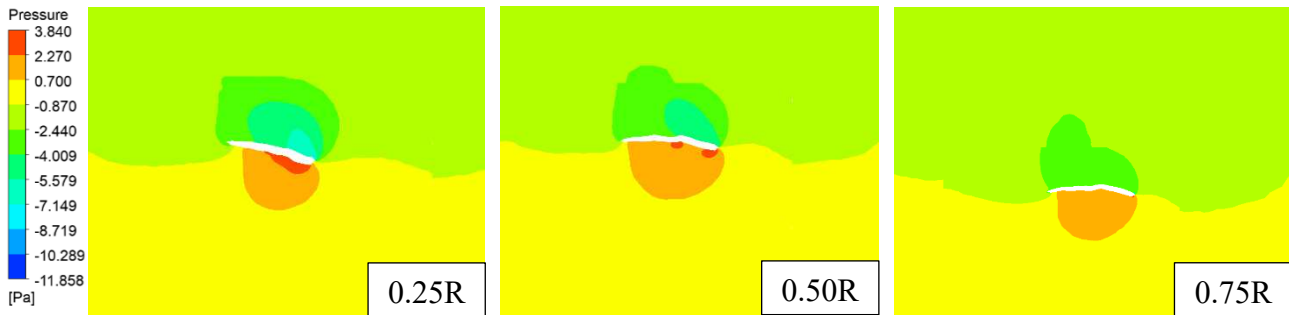
Figure 99. Pressure coefficient contours around the maple seed in autorotative flight.

The development of a spiral vortex, as shown in Figure 101, where fluid particles advance towards the trailing edge and separate from the surface near the leading edge to form a wake, as observed in the three sections (0.25R – Fig. 98a, 0.5R – Fig. 98b, 0.75R – Fig. 98c), is consistent with the experimental findings for seed edges by Lentink et al. (2009), Sohn (2016), Sohn (2014), and Fig. 21.
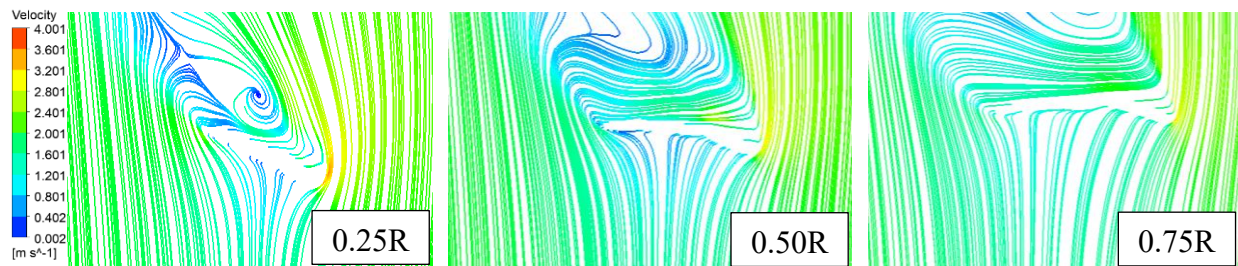
Figure 100. The flow pattern of sectional streamlines around the maple seed in autorotative flight.

Figure 102 depicts a spiral vortex developed in the lee region advancing towards the seed tip and merging with the flow passing over the tip, considered a mechanism for maintaining stable LEV (Leading Edge Vortex). This strong crossflow drains the LEV vorticity towards the wingtip vortex and prevents the LEV from growing and becoming unstable. The formed LEV resembles the conical spiral LEVs generated in delta-wing aircraft and those observed in the wing of a hawk moth (Ellington et al., 1996; Nakata & Liu, 2012).
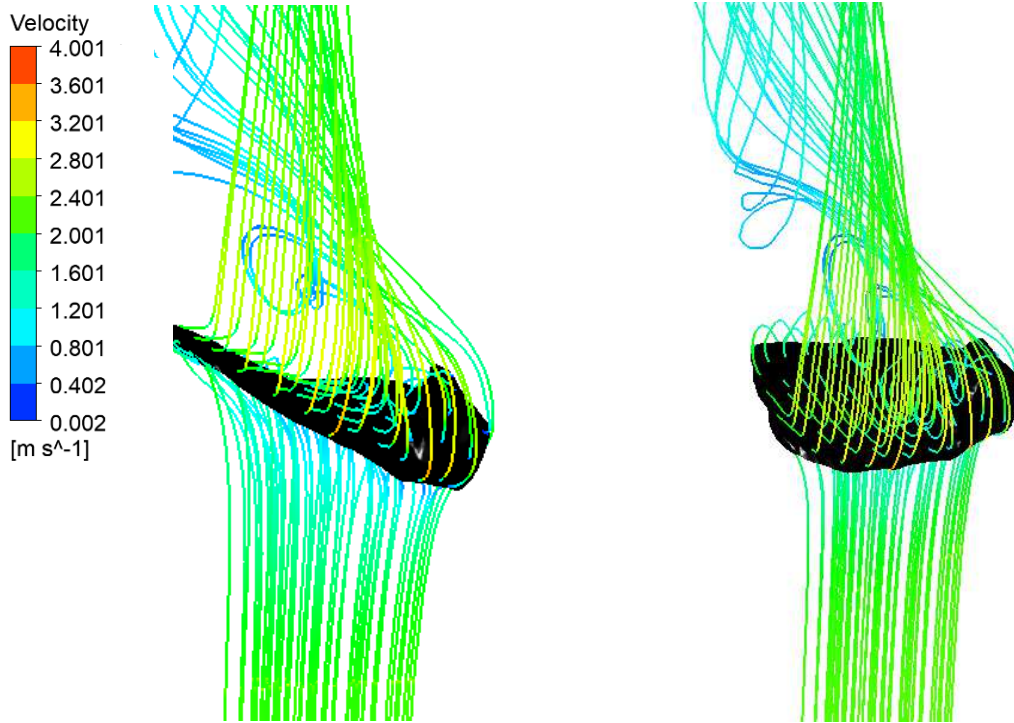
Figure 101. 3D flow structure of velocity distribution around the samarid in autorotative flight.

The velocity flow distribution also agrees with Lentink et al. (2009), Sohn (2016), Sohn (2014), and Holden (Fig. 30, 2015). Norberg (1973) explicitly states that natural seed edges have inclination angles ranging from -2 ° to 0°. For this study, an angle of attack of 0° was conventionally simulated, resulting in a torque of $5.6 \times 10\text{-}6$ Nm, like that found for the A. palmatum species studied by Sohn (2018), approximately 1.4×10^{-6} Nm.

7.4.3 Blades' flow pattern

The results of the CFD analysis of the blade sections are presented in Fig. 103 (Reference) and 104 (Bioinspired) at various radial positions from root to tip, through pressure contours (left) and flow streamlines (right), in both figures. Here, only the results at $\lambda = 5$ are presented, as this TSR represents the nominal wind speed of the conventional turbine, obtaining the best C_P results when it exhibits a defined behavior. Since there are no relevant visual contributions in the other conditions, it would be unfeasible to present the images of all simulations in this text.

The pressure and velocity distributions on the blade surface shown in Figures 102 and 103 from CFD simulations indicate variations in the contour pattern as the design angles of attack vary, with the direction of u_∞ in z+. As shown in Figure 17, the stagnation point is located at the leading edge of both cases, appearing from the fifth plane in the conventional blade and the fourth plane in the bioinspired blade. Therefore, the air flows faster over the bottom than the top surface, resulting in a pressure difference between the airfoil surfaces. In most radial sections of the blades studied, it becomes apparent that the static pressure values are usually lower on the bottom than

on the top surface. The variation in static pressure between the bottom and top surfaces decreases from root to tip. However, the difference in static pressure between the top and bottom surfaces, from root to tip, causes lift, tangential forces, and increased turbine power. In the case of the developed turbines, this may explain their low power.

The velocity streamlines in Figures 103 and 104 are extracted from full-scale 3D blade simulations using the plane cutting option in CFD post-processing, with 10 thousand points. Therefore, like Jin (2020), flow separation is not as abrupt, resulting in a less pronounced pressure gradient. This explains the presence of vorticity in the first three planes of interest of the conventional blade (r/R = 0.1 – 0.3) and the first plane of the bioinspired blade (r/R = 0.1), with sections closer to the root of the blade having a non-zero velocity magnitude in the mentioned vortices, which gradually reaches values close to zero in the section closest to the tip.

This suggests that the magnitude of the flow velocity in the 3D case has a significant non-zero component in the y direction along the blade. This can cause complex interactions between fluid and structure and, as a result, a more complicated flow pattern. One of the likely causes is the blade's asymmetry in 3D, mainly due to the twist angle between different sections of the blade.

One can compare the pressure coefficients' results with the velocity contours to gain a better understanding. For this flow condition, the wind velocity flow on the blade surface increases rapidly from the stagnation point to the pressure side at the leading edge. It increases towards the trailing edge, which is more evident for both the reference and bioinspired blades at planes above r/R = 0.3. As the design angles of attack increase (from tip to root), the wind velocity decreases at the leading edge and decreases further towards the trailing edge. Increasing the design angles of attack further reduces the pressure on the upper side while the pressure on the suction side remains relatively stable. Therefore, the attack's design angle influences the pressure differences between the pressure and suction sides. It is noteworthy that when considering the direction of wind flow, we observe a behavior that is practically opposite to what is predicted by theory.

In the bioinspired blade (Fig. 104), a significant reduction in recirculation is observed, especially at the edges. This indicates superior performance compared to the conventional airfoil. The magnitude of recirculation represents a loss for the flow in the Z+ direction; therefore, the smaller the recirculation, the smaller the flow separation, and consequently, the lower the losses. This analogy is relevant to aeronautics, where more significant recirculation areas often imply greater performance losses. The graphical representation clearly illustrates that the bioinspired blade exhibits a more efficient longitudinal flow pattern in the Z+ direction than the conventional blade, corroborating theoretical observations.
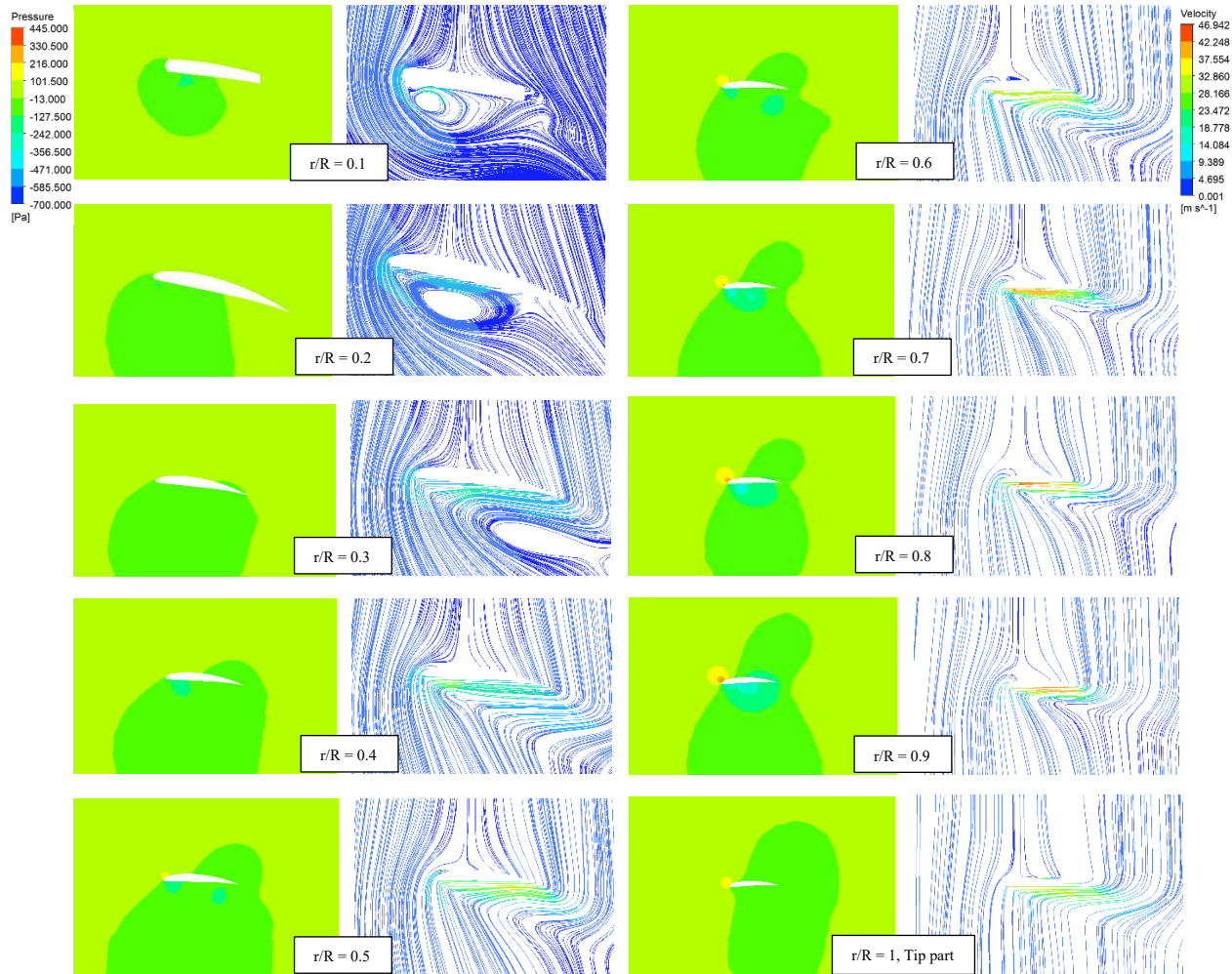
Figure 102. Pressure contour (left) and velocity streamlines (right) of the reference blade sections at different radial positions from the root to the tip (6 m/s – 460 RPM, u_∞ in z+).
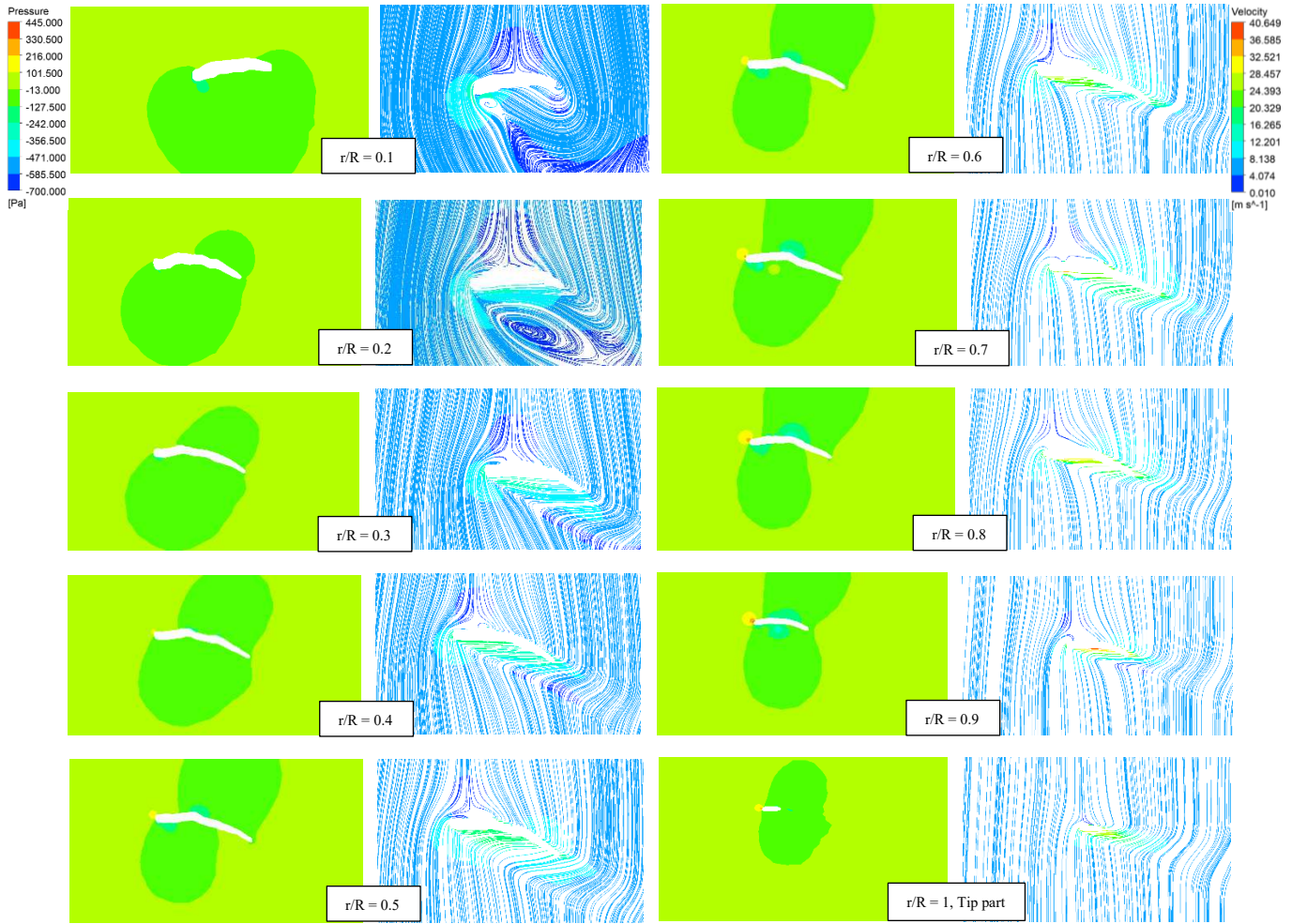
Figure 103. Velocity streamlines and pressure contour of the bioinspired blade sections at a different radial position from the root to the tip (6 m/s – 460 RPM, u_∞ in z+).

For a visual comparison, Fig. 104 presents the pressure distribution of the blades at a wind speed of 6 m/s and TSRs of 2 and 5. At TSR = 2, the pressure distributions on the standard and bioinspired blades exhibit similarity. The reference blade shows marginally higher pressure than the bioinspired blade, solely at the leading edge of the suction surface. These results in a slightly elevated wind energy coefficient for the reference blade compared to its conventional shape at low TSRs. At TSR = 5, the pressure distribution of both blades is almost identical. However, the pressure of the bioinspired blade at the leading edge of the blade is lower. This is caused by the irregular surface of the edge, which provides a deflection effect, which results in a non-smooth flow. Boundary layer separation is the main factor that decreases the blade's surface pressure.
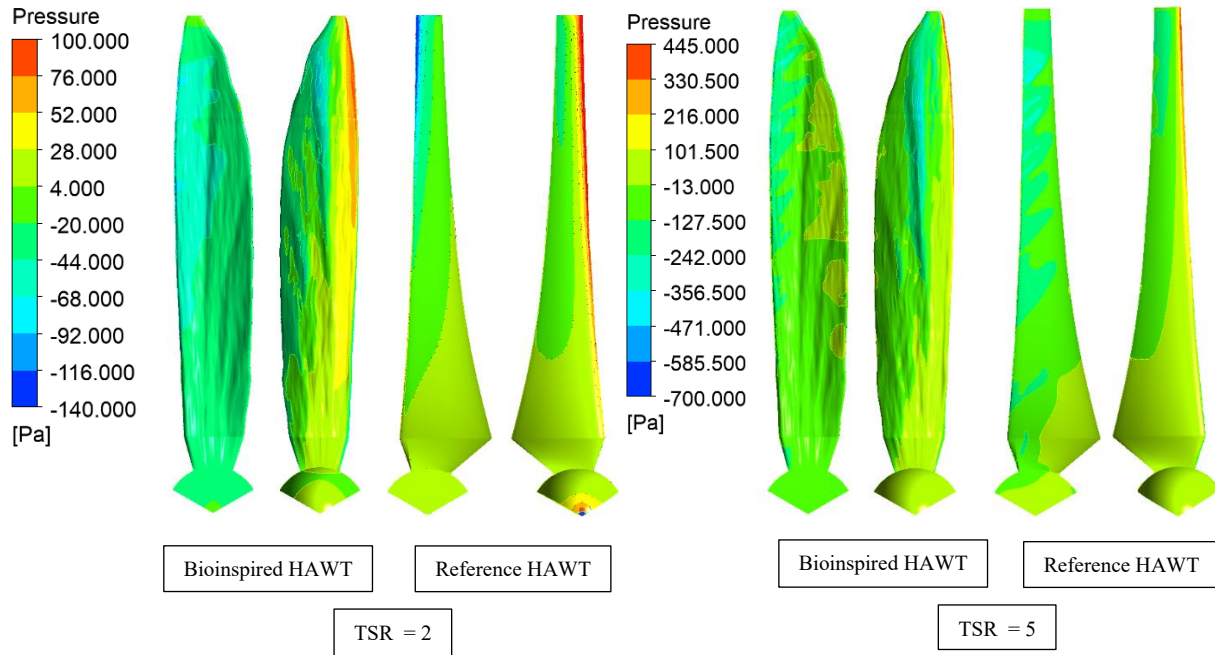
Figure 104. Surface cloud diagram of the blades at TSR of (a) 2 and (b) 5.

7.4.4 Performance Parameters

Based on the discussion regarding wind turbine performance in section 1.3, the critical performance parameters of interest in this study are P_{mec} and C_P, Eq. (2.18). The CL and CD curves of the SG6043 profile obtained by QBlade® were utilized to estimate the blade's power curve.

To achieve this, it is necessary to survey the torque in all simulations established previously in the methodology, whether experimental or numerical, for the blades. In the simulation case, the computed torque in the rotation direction must be multiplied by the number of blades and the angular velocity due to the periodicity of the adopted domains. The simulations covered a wind speed range from 4 to 12 m/s, with increments of 2 m/s, and a rotation speed of 200 to 700 RPM.

Thus, the ideal tip speed ratio (TSR = 5, between 300 – 500 RPM for the Reference and TSR = 6, around 400 RPM for the bioinspired blade) at which the coefficient of power Cp showed a maximum value was estimated (Fig. 105). At low TSRs (1 – 4.5), efficiency is naturally low as the turbine rotates slowly, but after TSR 5, the blade's performance remains remarkably high until TSR 5.5 – 6 for both cases. The behavior of the power coefficient reveals a significant improvement at high TSRs (5.5 – 7), meaning that even at high rotation speeds, the blade performs well. These results align with the findings of (Langtry & Menter, 2009), assuming that the ideal TSR is between 4 and 7 at low Reynolds numbers.

This phenomenon is attributed to the airfoil's favorable aerodynamic characteristics at low TSRs. At high TSRs, the geometry of the bioinspired HAWT blade is based on a samarid that acts

as a vortex generator, as shown in section 7.4.2, promoting higher torque and more significant energy capture.
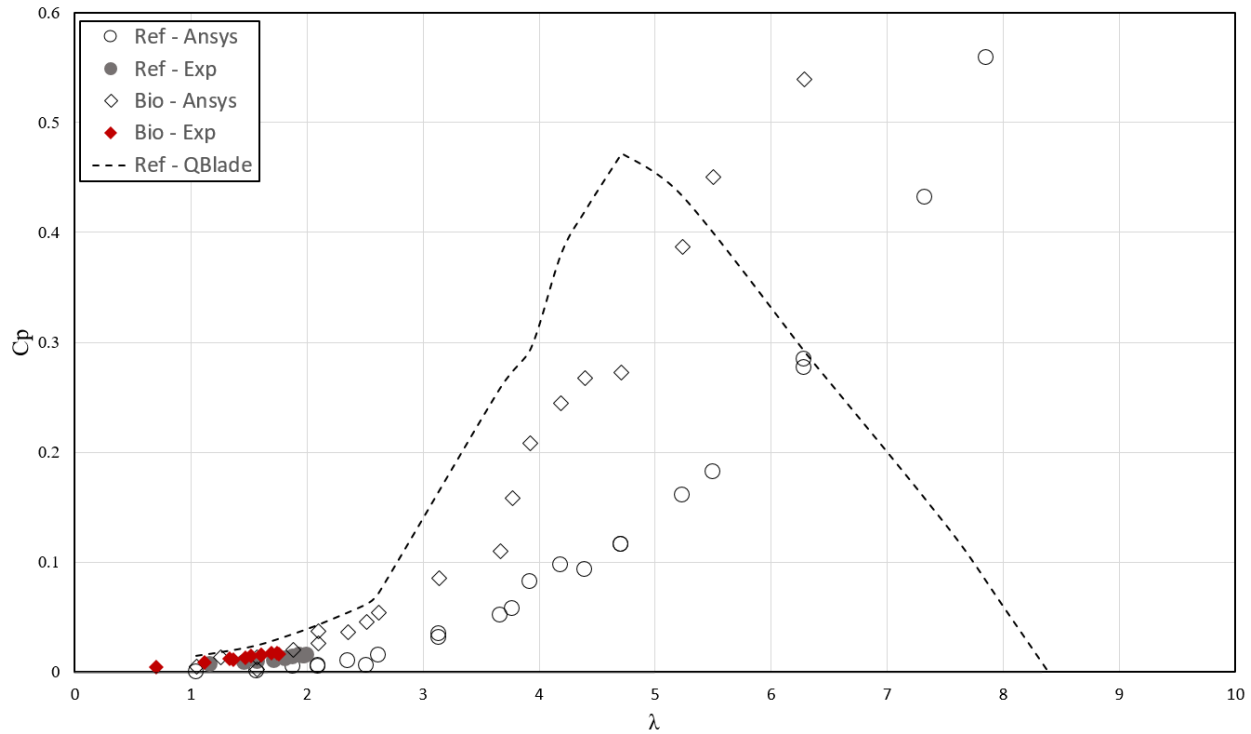
Figure 105. Comparison of the C_P for bioinspired and reference HAWT in QBlade®, Fluent® analyses, and experimental.

The experimental analysis in the wind tunnel demonstrated agreement with the onset of the C_P curve as a function of TSR for the bioinspired blades (diamond) and the reference blade (circle). Observing the initial position on the curve is crucial for understanding the blade's behavior under different operational conditions. It is worth noting that, due to the free shaft configuration, the blade does not function like a typical wind turbine, thus not producing significant torque, explaining why the experimental points are concentrated in the initial region of the graph (red diamond and gray circle).

As shown in Fig. 9, $C_{P,max} = 0.48$, theoretically occurs when $\beta = 0º$ and for $\lambda = 6.75$ (Soni; Kumar; Kumar, 2014). This value represents the ideal efficiency where the wind turbine extracts the maximum power from the wind (Molina; Mercado, 2011; Salles; Cardoso; Hameyer, 2011; Elbahi, 2017). For the developed blade, a value of 0.472 was obtained for $\lambda = 4.72$.

The initial position on the curve is coherent with the nearly absent torque, as both TSR and CP directly depend on this value. This scenario reflects the free shaft configuration, where the blade is not efficiently converting the wind's kinetic energy into mechanical torque. Although outside the typical operational context of a wind turbine, this experimental condition contributes to a comprehensive understanding of its behavior under various conditions.

The divergence between the CFD analysis data of the reference blade and the results obtained with the QBlade® software can be attributed to several reasons. Firstly, differences in the simulation models used in the two methods may be a crucial factor. Turbulence models, for instance, may vary among simulation tools, directly influencing predictions of the blade's aerodynamic behavior. Using different assumptions and simplifications in modeling may also introduce variations in results.

Additionally, initial conditions and simulation parameters may have been configured differently between the CFD analysis and QBlade®, contributing to the observed disparities. Both analyses must consistently represent the blade's geometry, material properties, and other specific model details to ensure comparable results.

Errors in defining boundary conditions, such as the accuracy of fluid properties and computational mesh characteristics, may equally influence results. Minor variations in these parameters can lead to significant divergences in results.

The gap between the CFD analysis and QBlade® data highlights the sensitivity of results to choices made during simulation, underscoring the importance of careful calibration and validation of the models used. Other comparative studies between RANS and QBlade® have also demonstrated some discrepancies (Koç et al., 2016; Surve et al., 2021; Laín et al., 2021; Dejene et al., 2024).

Finally, the C_{PS} for the three cases are calculated and listed in Tab. 12 for the RANS solution. It is important to note how closely the estimated values align with the theoretical maxima according to the Betz Limit.

Table 12. Performance values for the Qblade and RANS simulation compared to theoretical maximum values for an open turbine rotor according to Betz Limit.

Parameter	Value	Betz Maximum	(Betz – Value)/Betz
Reference (QBlade)	47,12 %		20 %
Reference (RANS)	55,90 %	59,26 %	5 %
Bioinspired (RANS)	53,89 %		9 %

Finally, the simulation and experimental results of the bioinspired blade developed in this work are compared to some experiments from Chapter 4, specifically Figures 60a, 60b, 64a, and 64b. These include studies by Gaitan-Aroca et al. (2020), Castañeda (2010), Wahanik (2015), Chu (2018), and Chu et al., (2022). All the curves displayed have similar boundary conditions, including a wind speed of $u_\infty = 10$ m/s. It is worth noting that all cases exhibit an inverted "U" shape in the C_P vs. TSR curves.
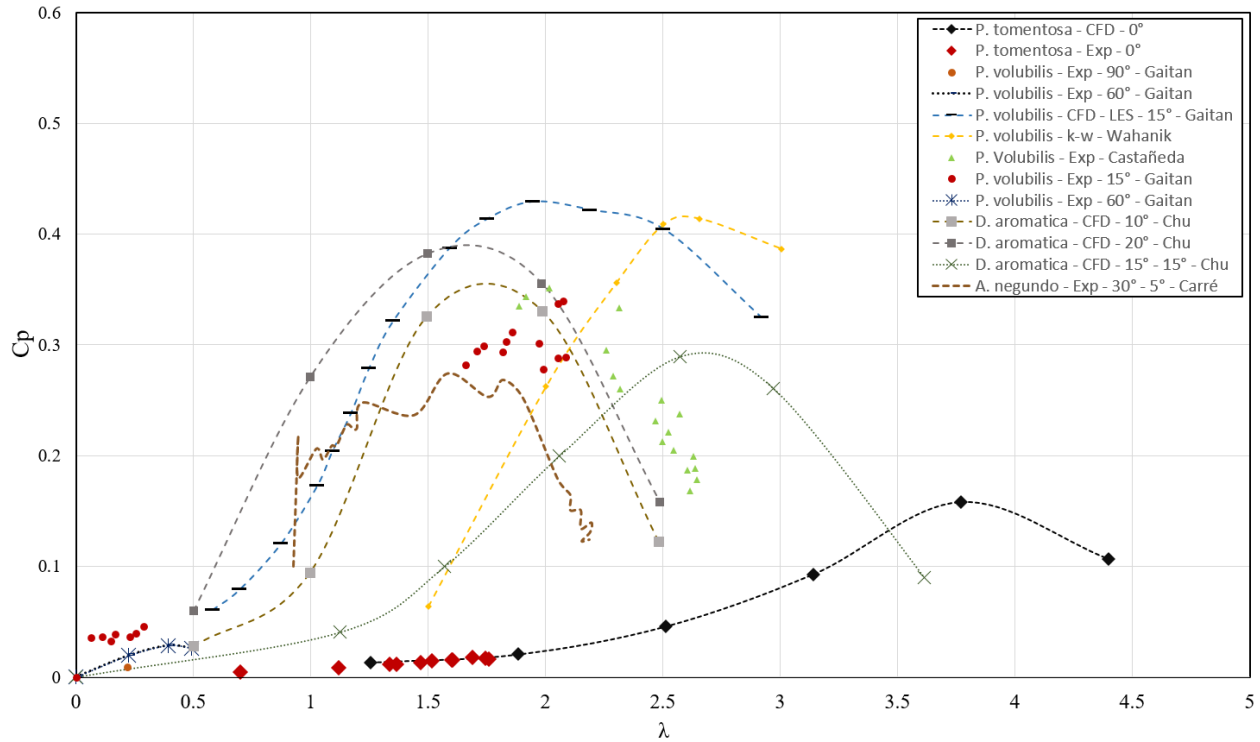
Figure 106. Comparison between C_P vs TSR of bioinspired blades.

The simulation results show that the biomimetic HAWT *P. volubilis* with a 15° bending angle of Gaitan-Aroca reached a maximum Cp value of 0.429 at λ of 1.94. Experimental results (both from Castañeda and Gaitan-Aroca) and LES simulation results have $C_{P,max}$ in the range of λ from 1.7 to 2.6. However, they have a 21 % difference due to disturbances caused by the measurement device used in the experimentation. Comparison with Wahanik's results shows a similar CP with a difference of 3.54 %, but with different values of λ. It is also noted that higher inclination angles, such as 60° and 90°, have considerably lower efficiency than smaller angles.

The *D. aromatica* rotor by Chu (2018) exhibited similar maximum C_P values for inclination angles of 10° and 20°, with average differences of 7.42 % for *P. volubilis* at the 10° angle and 16.1 % lower for the 20° angle. However, this initial study considered the seed's natural shape, altering only its bending angle. In 2022, adding the angle of attack αr, shown in Tab. 4, of 15° and a bending angle θr also of 15°, the $C_{P,max}$ was 0.2914. The $C_{P,max}$ value for *D. aromatica* in 2018 occurred at λ = 1.5; for 2022, it was at 2.6, while for *P. volubilis*, it was λ = 2.

It is essential to highlight that the HAWT developed by Carré et al. (2022), inspired by the A. negundo seed, has only a 44 mm diameter, and the curve presented is at a speed of 8 m/s. Thus, like Chu (2022), $\alpha = 30°$ and $\beta = 5°$ were adopted, with $C_{P,max} \approx 1.6$ in the range of $\lambda = 1.3 – 1.4$.

In the case of this study, for αr and θr of 0°, the prototype had a $C_{P,max}$ of approximately 0.16, in the range of 0.5 < λ < 4.5, considering both experimental and simulation values. The similarity in behavior between the curves of P. tomentosa and D. aromatica in 2022 is noticeable. As shown in Tab. 4, this was the worst case among the hypotheses raised by Chu et al. (2022).

This suggests that the blade developed in this work has the potential for performance like that of similar rotors at lower upstream speeds. Thus, this value can be optimized by studying other angles, such as the 24.5° angle in Tab. 8, obtained experimentally as the cone angle of the sampling collected from P. tomentosa samaras.

Determining the optimal α, β, and operating speed in a TSR range involves extensive simulations. These additional analyses would be essential to understand performance characteristics under various operating conditions better. However, conducting a comprehensive study of these parameters to optimize the performance of the bioinspired blade would require a significant number of simulations, which are beyond the time limitations of this master's thesis.

CHAPTER 8

8 CONCLUSIONS AND RECOMMENDATIONS FOR FUTURE WORKS

This study offers a comprehensive methodology for calculating specific performance parameters of conventional and bioinspired HAWTs utilizing seeds from the Brazilian Cerrado. By doing so, we gain a better understanding of their aerodynamic behavior.

The analysis delves into the autorotation behavior of three species of anemochoric samarids from the Cerrado, revealing consistent values with studies from other regions. Notably, this research is the first to focus solely on Cerrado seeds. Additionally, it provides new insights into a Cerrado samara's velocity and pressure flow behavior, making a unique contribution to the literature on the topic. We note notable flow patterns that resemble those documented in other cases through a detailed analysis of these specific aerodynamic parameters. These behaviors will be further explored in future publications.

This study provides valuable insights into the complex aerodynamics of the samara in autorotation, highlighting the significant impact of morphology on lift generation. The findings underscore the importance of a thick leading edge and undulating surface, corroborating previous research in this area. By deepening our understanding of the fluid dynamic behavior of these seeds, this study contributes to advancing knowledge in the field.

Moreover, the comprehensive aerodynamic characterization of the samara presented in this study is crucial for designing bioinspired blades for HAWTs. By analyzing the aerodynamic properties of the samara, including its autorotation behaviors, falling speeds, and flow patterns around an airfoil, through experimental analyses and CFD simulations, we establish a solid foundation for creating effective bioinspired technologies.

The data generated in this study can be used to optimize wind turbine blade design and replicate the samara's natural efficiency in capturing and converting wind energy. The correlation between experimental results and CFD modeling provides a grounded approach to innovation in small-scale wind turbines, validating and refining the bioinspired model. Overall, this study sheds light on the aerodynamic dynamics of the Cerrado samara and offers valuable insights into advancing bioinspired wind technology.

The comparative analysis between conventional and bioinspired blades revealed significant differences in terms of recirculation, especially at the tips. The reduction of recirculation in the bioinspired blade, notably at the tips, highlights superior performance to the conventional airfoil. The magnitude of recirculation represents a loss for flow in the Z+ direction, with higher recirculation resulting in more pronounced flow separation and, consequently, more significant losses, following aerodynamic logic. Figures 103 and 104 demonstrate that the bioinspired blade

exhibits a higher longitudinal flow in the Z+ direction than the conventional blade, corroborating the effectiveness of the bioinspired design.

In addition, this study has yielded valuable insights into wind turbine performance and torque, which are crucial for enhancing their effectiveness. Like the other examples in Chapter 4, the biomimetic wind turbines demonstrate greater initial torque than the standard HAWTs. This indicates that the suggested design for the biomimetic wind turbine will possess superior self-starting capabilities.

Overall, the performance of bioinspired wind turbines surpasses or equals that of conventional HAWT configurations in terms of CP and, consequently, energy conversion factor. This specific geometry has shown that the wind turbine has excellent potential to generate electricity in areas where wind speed is insufficient, for example, for countries that cannot afford more extensive and expensive devices. In the case of this study, although it is 3.6 % lower than the conventional blade in the zero angle of attack configuration, with some optimization adjustments of solidity and angle of attack, the provided wind power could be much higher.

It is also worth noting that this study presents some limitations, such as simplifying certain aspects of the wind environment. Among them, the freedom of the axis in the experimental analysis affects the consistency of some results. However, even in non-ideal situations, they maintain relative efficiency compared to simulated results.

Although the experimental data were limited by the absence of torque due to the free axis, it showed coherence with the trend predicted by CFD simulation. This alignment suggests a robust ability of bioinspired blades to respond to wind conditions, even in scenarios where torque is not fully utilized.

This phenomenon can be attributed to the adaptive capability of bioinspired geometry, which, even with the free axis, demonstrates behavior close to that predicted by CFD modeling. This observation highlights the resilience and effectiveness of these designs in challenging situations, indicating that their fundamental aerodynamic characteristics remain valid even when torque production is absent.

According to the results, the suggested biomimetic blade design for wind turbines can outperform the traditional design. Consequently, it is worth further exploring the biomimetic aerogenerator blade design, including optimizing its geometry to enhance power output and simplifying its structure to lower production expenses.

Considering these limitations in future research, developing strategies to mitigate them is recommended. As a proposal for future work, it is suggested:

- Experimental testing in a wind tunnel with prototype speed control through electric motors, where the rotation speed can be defined, like the approach of Krogstad and Lund (2012), to determine the turbine's response during different velocity profiles and examine LEV stability.
- Investigation of performance from the perspective of other angles of attack and taper ratio, as conducted by Chu et al. (2022).

- The collection of seed airfoil polar curves is used to optimize the lift-to-drag ratio by altering the angle of attack, as Pandolfi and Izzo (2013) suggested.
- Optimization of solidity was adopted for this study to enhance blade performance.
- Examination of vortex structure for different upstream velocities, as conducted by Gaitan-Aroca et al. (2020).
- Visualization of smoke and tuft flow using a wind tunnel equipped with high-speed cameras in Particle Image Velocimetry (PIV) analysis.

REFERENCES

Ackermann, T. Wind Energy- Part 4 for Renewable Energy Technology Course MJ2411 in KTH 2010. Royal Institute of Technolgy-KTH, Estocolmo, Suecia. 2010.

Akour, S. N.; Al-Heymari, M.; Ahmed, T.; Khalil, K. A. Experimental and theoretical investigation of micro wind turbine for low wind speed regions, Renew. Energy (2018). https://doi.org/10.1016/j.renene.2017.09.076

Anderson Jr, J. D. Fundamentals of aerodynamics, Tata McGraw-Hill Education, 2010.

Ansys. "Free Student Software: ANSYS Student." ANSYS, Inc. Accessed March 25, 2023. https://www.ansys.com/academic/free-student-products.

Augspurger, C. K. Morphology and dispersal potential of wind-dispersed diaspores of neotropical trees, American J. of Botany (1986) 353-363. https://doi.org/10.1002/j.1537-2197.1986.tb12048.x

Arranz, G., Moriche, M., Uhlmann, M., Flores, O.; Garcıa-Villalba, M. 2018 Bioinspiration & Biomimetics 13 036011. https://doi.org/10.1088/1748-3190/aab144

Ariffudin, M. H., Mohd Zawawi, F., Mohamed Kamar, H., & Kamsah, N. (2016). Effectiveness of blade tip on low speed horizontal axis wind turbine performance. Jurnal Teknologi, 78(8-4). https://doi.org/10.11113/jt.v78.9582

Aydın, N., Caliskan, M. E., Sabirli, M.U., Karagoz, I. An experimental study of the aerodynamic performance of a maple wing model at low Reynolds numbers, Mechanics Research Communications, Volume 130, 2023, 104104, ISSN 0093-6413, https://doi.org/10.1016/j.mechrescom.2023.104104

Azuma, A.; Yasuda, K. Flight performance of rotary seeds. J. Theor. Biol. 1989, 138, 23–53. https://doi.org/10.1016/S0022-5193(89)80176-6

Bai, S.; Chirarattananon, P. Design and take-off flight of a samara-inspired revolving-wing robot. In Proceedings of the 2019 IEEE/RSJ International Conference on Intelligent Robots and Systems (IROS), Macau, China, 3–8 November 2019; pp. 6070–6076. https://doi.org/10.1109/IROS40897.2019.8967600

Betz, A., 1920. Das maximum der theoretisch moglichen Auswendung des Windes durch Windmotoren, vol. 26. Zeitschrift fur gesamte Turbinewesen.

Biadgo, A. M.; Aynekulu, G. (2017). Aerodynamic Design of Horizontal Axis Wind Turbine Blades. FME Transactions, 45:647-660. https://doi.org/10.5937/fmet1704647M

Birch, J.M.; Dickinson, M.H. Spanwise flow and the attachment of the leading-edge vortex on insect wings. Nature 2001, 412, 729–733. https://doi.org/10.1038/35089071

Burton, T. et al. Wind energy handbook. West Sussex: WILEY, 2001. https://doi.org/10.1002/0470846062

Bodling, A.; Agrawal, B. R.; Sharma, A.; Clark, I.; Alexander, W. N.; Devenport; W. Numerical

investigations of bio-inspired blade designs to reduce broadband noise in aircraft engines and wind turbines. AIAA SciTech Forum - 55th AIAA Aerosp. Sci. Meet. January, 9 – 13 (2017), pp. 1-16. https://doi.org/10.2514/6.2017-0458

Branlard, E. Wind Turbine Tip-Loss Corrections: Review, Implementation and Investigation of New Models. Master's Thesis, Technical University of Denmark, Lyngby, Denmark, 2011.

Carré, A.; Roux, E.; Tabourot, L.; Gasnier, P. Innovative blade shape for micro wind turbines, 2022 Wireless Power Week WPW (2022) 121–125. https://doi.org/10.1109/WPW54272.2022.9854036

Castañeda, D. Diseño y Construcción de un Sistema Eólico para Bombeo Basado en un Rotor Bioinspirado. Universidad Nacional de Colombia: Bogotá, CO, USA, 2010.

CD-Adapco – STAR-CCM+. http://www.cd-adapco.com/products/star-ccm%C2%AE

Chowdhury, H., Islam, R., Hussein, M., Zaid, M., Loganathan, B., & Alam, F. (2019). Design of an energy efficient car by biomimicry of a boxfish. Energy Procedia, 160, 40–44. https://doi.org/10.1016/j.egypro.2019.02.116

Chu, Y. J. A new biomimicry marine current turbine: Study of hydrodynamic performance and wake using software OpenFOAM. J Hydrodyn 2016;28:125–41. https://doi.org/10.1016/S1001-6058(16)60614-5

Chu, Y. J., Chong, W.T. A biomimetic wind turbine inspired by Dryobalanops aromatica seed: Numerical prediction of rigid rotor blade performance with OpenFOAM®. Comput Fluids 2017;159:295–315. https://doi.org/10.1016/j.compfluid.2017.10.012

Chu, Y.J, Chong, W.T. Numerical study of conventional and biomimetic marine current turbines in tandem by using OpenFOAM®. J Mech 2018;34:679–93. https://doi.org/10.1017/jmech.2017.46

Chu, Y. J. Conceptual Design and Performance Analysis of a Biomimetic Wind Turbine Inspired by the Dryobalanops Aromatica Seed. Master Dissertation, University of Malaya, 2018.

Chu, Y. J, Lam H. F. Comparative study of the performances of a bio-inspired flexible-bladed wind turbine and a rigid-bladed wind turbine in centimeter-scale. Energy 2020;213:118835. https://doi.org/10.1016/j.energy.2020.118835

Chu, Y. J., Lam, H. F., Peng, H. Y. Numerical investigation of the power and self-start performance of a folding-blade horizontal axis wind turbine with a downwind configuration. Int J Green Energy 2021. https://doi.org/10.1080/15435075.2021.1930003

Custódio, R. S. Energia Eólica: para a produção de energia elétrica. 2. ed. Rio de Janeiro: Synergia: Acta: Abeeólica, 2013.

Cognet, V.; Pont, S.C.D.; Dobrev, I.; Massouh, F.; Thiria, B. Bioinspired turbine blades offer new perspectives for Wind Energy. Proc. R. Soc. A 2017, 473, 20160726. https://doi.org/10.1098/rspa.2016.0726

Corda, S. Introduction to Aerospace Engineering with a Flight Test Perspective, Wiley, New York, 2017.

Correa-Álvarez, M.; Villada-Quiceno, V.; Sierra-Pérez, J.; García-Navarro, J.; Nieto-Londoño, C. Structural design of carbon/epoxy bio-inspired wind turbine blade using fluid/structure simulation. Int J Energy Res, 40 (13) (2016), pp. 1832-1845. https://doi.org/10.1002/er.3564

Dang, H.S.; Lai, H.N. Investigating the design parameters of maple seed's aerodynamic force by Taguchi method to apply to wind turbine blades, in: 4th International Conference on Green Technology and Sustainable Development (GTSD), 2018, pp. 110–113. https://doi.org/10.1109/GTSD.2018.8595647

De Lellis, M., Reginatto, R., Saraiva, R., Trofino, A., 2018. The Betz limit applied to airborne wind energy. Renew. Energy 127, 32–40. https://doi.org/10.1016/j.renene.2018.04.034

Drela, M.; Youngren, H. XFOIL. Computer software. Xfoil: Subsonic Airfoil Development. Vers. 6.97. Massachusetts Institute of Technology, n.d. Web. 1 Feb. 2014

Døssing, M.; Madsen, H.A.; Bak, C. Aerodynamic optimization of wind turbine rotors using a blade element momentum method with corrections for wake rotation and expansion. Wind Energy 2012, 15, 563–574. https://doi.org/10.1002/we.487

Elbahi. A. Variation and the influence of the pitch angle of the rotational speed of the wind turbine. J. Electr. Eng., 17 (3) (2017), p. 11

Elizondo, J.; Martínez, J.; Probst, O. Experimental study of a small wind turbine for low- and medium-wind regimes, Int. J. Energy Res. (2009). https://doi.org/10.1002/er.1482

Ellington, C. P., van den Berg, C., Willmott, A. P., & Thomas, A. L. R. (1996). Leading-edge vortices in insect flight. Nature, 384(6610), 626–630. https://doi.org/10.1038/384626a0

Fedorov, S. (2002). GetData Graph Digitizer version 2.24. Russia: Get data-graph-digitizer-com.

Fish, F. E. "Limits of Nature and Advances of Technology: What Does Biomimetics Have to Offer to Aquatic Robots?", Applied Bionics and Biomechanics, vol. 3, Article ID 506474, 12 pages, 2006. https://doi.org/10.1533/abbi.2004.0028.

Fish, F.E., Weber, P.W., Murray, M.M. and Howle, L.E. (2011), "The tubercles on humpback whales' flippers: application of bio-inspired technology", Integrative and Comparative Biology, Soc Integ Comp Biol, Vol. 51 No. 1, pp. 203–213. https://doi.org/10.1093/icb/icr016

Ford, C.P.; Babinsky, H. Lift and the leading-edge vortex. J. Fluid Mech. 2013, 720, 280–313. https://doi.org/10.1017/jfm.2013.28

Gaitan-Aroca, J.; Sierra, F.; Castellanos Contreras, J.U. Bio-Inspired Rotor Design Characterization of a Horizontal Axis Wind Turbine. Energies 2020, 13, 3515. https://doi.org/10.3390/en13143515

Garré, S. O. Avaliação experimental do desempenho aerodinâmico de pequenas turbinas eólicas confeccionadas em prototipagem 3D. 2015: Dissertação (Mestrado em engenharia) - Escola de Engenharia, UFRGS. Porto Alegre, 2015. E-book. Disponível em: https://lume.ufrgs.br/handle/10183/132643.

Gasch, R. Twele, J., Wind Power Plants: Fundamentals, Design, Construction and Operation, 2nd ed., Springer-Verlag, Berlin, 2012. https://doi.org/10.1007/978-3-642-22938-1

Gasnier, P.; Alessandri, B.; Fayer, T.; Garraud, N.; Pauliac-Vaujour, N.; Boisseau, S. Modelling and Characterization of a High-Efficiency, Cm-Scale and Low Velocity Airflow-Driven Harvester for Autonomous Wireless Sensor Nodes, Proc. Power-MEMS (2019). https://doi.org/10.1109/PowerMEMS49317.2019.41031600279

Gasnier, P.; Willemin, J.; Boisseau, S.; Goubault De Brugière, B.; Pillonnet, G.; Gomez, B.; et al. A cm-scale, low wind velocity and 250◦ C-compliant airflow-driven harvester for aeronautic applications. Proc PowerMEMS 2018. https://doi.org/10.1088/1742-6596/1407/1/012071

Glauert, H. Airplane propellers. In Aerodynamic Theory; Springer: Berlin/Heidelberg, Germany, 1935; pp. 169–360. https://doi.org/10.1007/978-3-642-91487-4_3

Global Wind Energy Council. GWEC Global Wind Report 2023; Global Wind Energy Council: Bonn, Germany, 2023.

Giguère, P.; Selig, M.S., "Low Reynolds number airfoils for small horizontal axis wind turbines", Wind Engineering 21 (6), 367-380, 1997.

Giguère, P. Selig, M. S. New Airfoils for Small Horizontal Axis Wind Turbines, J. Sol. Energy Eng. (2008).

Greene, D.; Johnson, E. Seed mass and dispersal capacity in wind-dispersed diaspores, Oikos (1993) 69-74. https://doi.org/10.2307/3545096

Habali, S. M.; Saleh, I. A. Local design, testing and manufacturing of small mixed airfoil wind turbine blades of glass fiber reinforced plastics. Part I: design of the blade and root, Energy Convers. Manag. (2000). https://doi.org/10.1016/S0196-8904(99)00104-1

Hadi, A.E.; Tezara, C.; Fitriyana, D.F.; Siregar, J.P.; Oumer, A.N.; Hamdan, M.H.M.; Jaafar, J.; Irawan, A.P.; Zalinawati, M. Effect of Water Absorption Behaviour on Tensile Properties of Hybrid Jute-Roselle Woven Fibre Reinforced Polyester Composites, International Journal of Automotive and Mechanical Engineering: Vol. 18 No. 4 (2021): December. https://doi.org/10.15282/ijame.18.4.2021.02.0705

Hansen, M.O. Aerodynamics of Wind Turbines; Routledge: London, UK, 2015. https://doi.org/10.4324/9781315769981

Hau, E. (2006). Wind Turbines. Fundamentals, Technologies, Application, Economics. 2edition. https://doi.org/10.1007/3-540-29284-5

Herrera, C.; Correa, M.; Villada, V.; Vanegas, J.D.; Garcia, J.G.; Nieto-Londoño, C. et al. Structural design and manufacturing process of a low scale bio-inspired wind turbine blades. Compos Struct, 208 (2019), pp. 1-12. https://doi.org/10.1016/j.compstruct.2018.08.061

Holden, J. R., Caley, T. M., & Turner, M. G. Maple Seed Performance as a Wind Turbine. In 53rd AIAA Aerospace Sciences Meeting. 2015. https://doi.org/10.2514/6.2015-1304

Holden, J. R. Experimental Testing and Computational Fluid Dynamics Simulation of Maple Seeds and Performance Analysis as a Wind Turbine. Master's thesis, University of Cincinnati, 2016.

Howe, H. F.; Smallwood, J. Ecology of seed dispersal, Annual Review of Ecology and Systematics (1982) 201-228. https://doi.org/10.1146/annurev.es.13.110182.001221

Ikeda, T, Tanaka H, Yoshimura R, Noda R, Fujii T, Liu H. A robust biomimetic blade design for micro wind turbines. Renew Energy 2018;125:155–65. https://doi.org/10.1016/j.renene.2018.02.093

Ikeda, T. "Study on noise-reduction and high-efficiency of bird wing-inspired micro-wind turbines." PhD diss., 千葉大学= Chiba University, 2018.

Ingram, G. Wind Turbine Blade Analysis using the Blade Element Momentum Method. https://community.dur.ac.uk/g.l.ingram/download/wind_turbine_design.pdf

Jin, J. Y., Virk, M; Hu, Q.; Jiang, X.. (2020). Study of Ice Accretion on Horizontal Axis Wind Turbine Blade Using 2D and 3D Numerical Approach. IEEE Access. 8. https://doi.org/10.1109/ACCESS.2020.3022458

Jaszczur, M., Młynarczykowska, A. (2020). A General Review of the Current Development of Mechanically Agitated Vessels. Processes, 8(8), 982. https://doi.org/10.3390/pr8080982

Koç, E., Gunel, O., & Yavuz, T. (2016). Mini-scaled horizontal axis wind turbine analysis by Qblade and CFD. International Journal of Energy Applications and Technologies, 3(2) 87 – 92, 2016.

Kolvart, M. New Blade Profile Shapes for Small Urban Wind Turbines Applications. Master's Thesis, University of Groningen, Groningen, The Netherlands, 2021.

Krogstad, P-Å., and J. A. Lund. "An experimental and numerical study of the performance of a model turbine." Wind Energy 15, no. 3 (2012): 443-457. https://doi.org/10.1002/we.482

Kreith, Frank (Ed.): Mechanical Engineering Handbook. Boca Raton : CRC Press, 1999. https://doi.org/10.1201/NOE0849397516

Kumar, K.S., Pendyala, S. (2022). Computational Analysis of Morphing Geometry Inspired From Butterfly Wings in the Application Micro Aerial Vehicles. J Robot Auto Res, 3(3), 300-307. https://doi.org/10.21203/rs.3.rs-1368767/v1

Laín, S.; Contreras, LT; López, OD Caracterização Hidrodinâmica de uma Turbina Hidrocinética Tipo Garman. Fluidos 2021 , 6 , 186. https://doi.org/10.3390/fluids6050186

Lanzafame, R.; Mauro, S.; Messina, M. Wind turbine CFD modeling using a correlation-based transitional model. Renew. Energy Int. J. 2012, 52, 31–39. https://doi.org/10.1016/j.renene.2012.10.007

Langtry, R.B.; Menter, F.R. Correlation-Based Transition Modeling for Unstructured Parallelized Computational Fluid Dynamics Codes. AIAA J. 2009, 47, 2894–2906. https://doi.org/10.2514/1.42362

Lissaman, P.B.S. Low-Reynolds-Number Airfoils, Annu. Rev. Fluid Mech. (1983). https://doi.org/10.1146/annurev.fl.15.010183.001255

Lee, M.H., Shiah, Y. C., Bai, C. J. Experiments and numerical simulations of the rotor-blade performance for a small-scale horizontal axis wind turbine. J Wind Eng Ind Aerodyn 2016;149:17–29. https://doi.org/10.1016/j.jweia.2015.12.002

Leishman, J. G. Principles of helicopter aerodynamics with CD extra, Cambridge U.P. (2006)

Lentink, D., Dickson, W. B., van Leeuwen, J. L., & Dickinson, M. H. (2009). Leading-Edge Vortices Elevate Lift of Autorotating Plant Seeds. Science, 324(5933), 1438–1440. https://doi.org/10.1126/science.1174196

Lynch, C. E. (2011). Advanced CFD Methods for Wind Turbine Analysis. PhD thesis, Georgia Institue of Technology.

Maliska, C. R. Transferência de Calor e Mecânica dos Fluidos Computacional: Fundamentos e Coordenadas Generalizadas. 2 ed. LTC, 2012McCutchen, C. W. 1977 Science 197 691–692.

Manwell, J. F.; McGowan, J. G.; Rogers, A. L. John Wiley & Sons, 2010. 7782, 2010. Lead acid ... Wind energy explained 2, 91-155, 2009. 93, 2009.

Menter FR, Kuntz M, Langtry R. Ten years of industrial experience with the SST turbulence model. Turbulence, Heat Mass Transfer 2003;4(1):625–32.

Menter, F. R. Two-equation eddy-viscosity turbulence models for engineering applications. AIAA J 1994;32(8):1598–605. https://doi.org/10.2514/3.12149

Miller, N.; Price, W.; Snachez-Gasca, J. " Dynamic modeling of GE 1.5and 3.3 wind turbine generators", Version 3.0, October 27, 2003

Minami, S.; Azuma, A. Various flying modes of winddispersal seeds, J. of Theoretical Biology, 225 (2003) 1-14. https://doi.org/10.1016/S0022-5193(03)00216-9

Molina, A. G.; Mercado, P. E. (2011). Modelling and Control Design of Pitch-Controlled Variable Speed Wind Turbines. Wind Turbines. https://doi.org/10.5772/15880

Moriarty, P. J.; Hansen, A. C. AeroDyn Theory Manual. Colorado: National Renewable Energy Laboratory; 2005. https://doi.org/10.2172/15014831

Nakata, T., Liu, H. 2012 Aerodynamic performance of a hovering hawkmoth with flexible wings: a computational approach. Proc. R. Soc. B 279, 722–731. https://doi.org/10.1098/rspb.2011.1023

Nathan, R.; Katul, G. G.; Horn, H. S.; Thomas, S. M.; Oren, R.; Avissar, R.; Pacala, S. W.; Levin, S. A. Mechanisms of long-distance dispersal of seeds by wind, Nature 418 (July) (2002) 409–414. https://doi.org/10.1038/nature00844

Nathan, R. Long-Distance Dispersal of Plants, Science 313 (2006) 786–788. https://doi.org/10.1126/science.1124975

Nave, G. K., Hall, N., Somers, K., Davis, B., Gruszewski, H., Powers, C., et al. Wind dispersal of natural and biomimetic maple samaras. Biomimetics 2021;6(2). https://doi.org/10.3390/biomimetics6020023

Norberg, R.Å. Autorotation, self-stability, and structure of single-winged fruits and seeds (samaras) with comparative remarks on animal flight. Biol. Rev. 1973, 48, 561–596. https://doi.org/10.1111/j.1469-185X.1973.tb01569.x

Okulov, V.L.; Sørensen, J.N. Refined Betz limit for rotors with a finite number of blades. Wind. Energy 2008, 11, 415–426. https://doi.org/10.1002/we.274

OpenFOAM. The open source CFD Toolbox, user guide. OpenCFD Ltd; 2015.

Ortega-Jimenez, V. M., Kim, N. S.-W., & Dudley, R. (2019). Superb autorotator: rapid decelerations in impulsively launched samaras. Journal of The Royal Society Interface, 16(150), 20180456. https://doi.org/10.1098/rsif.2018.0456

Paiva, L. F. Experimental analysis of biomimetic blades for small wind turbines. 2021. 103 f. Trabalho de Conclusão de Curso (Graduação em Engenharia Aeronáutica) – Universidade Federal de Uberlândia, Uberlândia, 2021.

Patel, Y. (2010) Numerical iInvestigation of flow past a circular cylinder and in a staggered tube bundle using various turbulence models. Master's thesis. Lappeenranta University of Technology.

Pinto, M. O. Fundamentos de energia eólica. 1. ed. Rio de Janeiro: LCT, 2013.

Pletcher, R. H., Tannehill, J. C., and Anderson, D. Computational fluid mechanics and heat transfer , CRC Press, 2012.

Rabault, J.; Fauli, R.A.; Carlson, A. Curving to fly: Synthetic adaptation unveils optimal flight performance of whirling fruits. *Phys. Rev. Lett.* **2019**, *122*, 024501. https://doi.org/10.1103/PhysRevLett.122.024501

Ragheb, M.; Ragheb, A.M. Wind Turbines Theory—The Betz Equation and Optimal Rotor Tip Speed Ratio; INTECH Open Access Publisher: London, UK, 2011. https://doi.org/10.5772/21398

Ralston E.; G. Swain. Bioinspiration – The solution for biofouling control? Bioinsp. Biomim. 4 (2009). ttps://doi.org/10.1088/1748-3182/4/1/015007

Rao, M.; Hoysall, D.C.; Gopalan, J. Mahogany seed–a step forward in deciphering autorotation. *Curr. Sci.* **2014**, *106*, 1101.

Reinders, A., Diehl, J. C., & Brezet, H. (Eds.). (2012). The Power of Design. https://doi.org/10.1002/9781118361177

Rezgui, D.; Arroyo, I.H.; Theunissen, R. Model for sectional leading-edge vortex lift for the prediction of rotating samara seeds performance. *Aeronaut. J.* **2020**, *124*, 1236–1261. https://doi.org/10.1017/aer.2020.25

Rijs, R. P. P., Smulders, P. T.: Blade Element Theory for Performance Analysis of Slow Running Wind Turbines, Wind Engineering, Vol.14 No.2, 1990.

Rosato, M.A. Small Wind Turbines for Electricity and Irrigation; CRC Press: Boca Raton, FL, USA, 2018. https://doi.org/10.1201/b22493

Rosen, A.; Seter, D. Vertical autorotation of a singlewinged samara, J. of Applied Mechanics, 58 (1991) 1064-1071. https://doi.org/10.1115/1.2897683

Rosyadi, M., Muyeen, S. M., Takahashi, R., & Tamura, J. (2012). A Design Fuzzy Logic Controller for a Permanent Magnet Wind Generator to Enhance the Dynamic Stability of Wind Farms. Applied Sciences, 2(4), 780–800. https://doi.org/10.3390/app2040780

Sairam, K., 2013. "The Influence of Radial Area Variation on Wind Turbines to the Axial Induction Factor". Master's thesis University of Cincinnati.

Salles, M.B., Cardoso, J.R.and Hameyer, K. (2011) Dynamic Modeling of Transverse Flux Permanent Magnet Generator for Wind Turbines.Journal of Microwaves, Optoelectronics and Electromagnetic Applications, 10, 95-105. https://doi.org/10.1590/S2179-10742011000100010

Sane, S.P. The aerodynamics of insect flight. J. Exp. Biol. 2003, 206, 4191–4208. https://doi.org/10.1242/jeb.00663

Sarkar, M. R., Julai, S., Tong, C. W., Uddin, M., Romlie, M. F., & Shafiullah, G. (2020). Hybrid Pitch Angle Controller Approaches for Stable Wind Turbine Power under Variable Wind Speed. Energies, 13(14), 3622. https://doi.org/10.3390/en13143622

Schluter, J., "Derivation of the Reynolds-Averaged Navier-Stokes Equations Part 1," Online lecture, 2014 November.

Schmitz, S. Aerodynamics of Wind Turbines: A Physical Basis for Analysis and Design; Wiley: Hoboken, NJ, USA, 2020; ISBN 9781119405597.

Seidel, C.; Jayaram, S.; Kunkel, L.; Mackowski, A. Structural analysis of biologically inspired small wind turbine blades. Int J Mech Mater Eng, 12 (1) (2017), pp. 1-9. https://doi.org/10.1186/s40712-017-0085-3

Seter, D.; Rosen, A. Study of the vertical autorotation of a singlewinged samara. Biol. Rev. 1992, 67, 175–197. https://doi.org/10.1111/j.1469-185X.1992.tb01018.x

Seter, D.; Rosen, A. Theoretical and experimental study of axial autorotation of simple rotary decelerators. J. Aircr. 2014, 51, 236–248. https://doi.org/10.2514/1.C032305

Silva, N. G. Dimensionamento de perfis aerodinâmicos de uma torre eólica/ Nathan Gazon da Silva – Macaé: UFRJ/Campus UFRJ-Macaé, 2017. XVI, 122 p.: il.; 29,7 cm. Orientador: Esdras Pereira de Oliveira Projeto de Graduação – UFRJ / Campus UFRJ-Macaé / Curso de engenharia civil, 2017.

Siddappaji, K., 2012. "Parametric 3d blade geometry modeling tool for turbomachinery systems". Master's thesis University of Cincinnati.

Skews, B. W. (1991) Autorotation of many-sided bodies in an airstream. Nature 352:512–513. https://doi.org/10.1038/352512a0

Smith, E. H. (1970) Autorotating wings: an experimental investigation. Cambridge University Press, Cambridge

Snel, H. (2003). Review of Aerodynamics for Wind Turbines. Wind Energy, 6(3), 203–211. https://doi.org/10.1002/we.97

Soni, R.; Kumar, A.; Kumar, R.; Singh, S. (2014). Comparative Study of SVM and Hysteresis Control Strategies for Grid Side Converter of PMSG. 11th IEEE India Conference: Emerging Trends and Innovation in Technology, INDICON 2014. https://doi.org/10.1109/INDICON.2014.7030546

Sohn, M.H., Im, D.K. Flight characteristics and flow structure of the autorotating maple seeds. J Vis 25, 483–500 (2022). https://doi.org/10.1007/s12650-021-00812-9

Sovran, G.; Morel, T.; Mason, W. T. Jr.: Aerodynamic drag mechanisms of bluff bodies and road vehicles. New York : Plenum Press, 1978. https://doi.org/10.1007/978-1-4684-8434-2

Stevenson, R. A., Evangelista, D., Looy, C. V. When conifers took flight: a biome-chanical evaluation of an imperfect evolutionary takeoff. Paleobiology.2015; 41:205–25. https://doi.org/10.1017/pab.2014.18

Surve, M. L., Unde, S. S., Sutar, K. B., Dhurpate, P., Kumbhar, D. G. (2021) Computational Studies on Airfoil for Micro-Capacity Horizontal Axis Wind Turbine. Indian Journal of Science and Technology 14(29): 2427-2438. https://doi.org/10.17485/IJST/v14i29.824

Swanson, T.; Isaac, K. M. Biologically inspired wing leading edge for enhanced wind turbine and aircraft performance. 6th AIAA Theor. Fluid Mech. Conf. June, 27 –30 (2011), pp. 1-10.

Top, L. Biomimetic Blade Profile Shapes for Efficient Small Urban Wind Turbines. Master's Thesis, University of Groningen, Groningen, The Netherlands, 2022.

Ulrich, E. R.; Pines, D. J.; Humbert, J. S. From falling to flying: the path to powered flight of a robotic samara nano air vehicle, Bioinspiration & Biomimetics, 5 (2010). https://doi.org/10.1088/1748-3182/5/4/045009

Varshney, K., Song, C., Wang, Z. J. The kinematics of falling maple seeds and the initial transition to a helical motion. Nonlinearity. 2011;25:C1-8. https://doi.org/10.1088/0951-7715/25/1/C1

Vincent, J.F. 1990b. Structural Biomaterials. Princeton University Press, United States of America.

Xia, G.; Cao, Y.; Qian, Z.; Zhu, Y.; Wang, J.; Guo, T.; Yang, Y.; Zhang, W.; Wang, Y.; Wu, G. Optimization Layout and Aerodynamic Performance Research on Double Nautilus Vertical-Axis Wind Turbine. Appl. Sci. 2023, 13, 10959. https://doi.org/10.3390/app131910959

XFLR5- http://www.xflr5.com/xflr5.htm

Wahanik, W.F. Simulación de Fluidos de una Turbina Bioinspirada Usando OpenFoam; Universidad Nacional de Colombia: Bogotá, CO, USA, 2015.

Walsum, T.A.v. Penguin Flipper Hydrodynamics. Master's Thesis, University of Groningen, Groningen, The Netherlands, 2013.

Wang, Q.; Zhou, H.; Wan, D. Numerical simulation of wind turbine blade-tower interaction. J. Mar. Sci. Appl. 2012, 11, 321–327. https://doi.org/10.1007/s11804-012-1139-9

Wilcox, D. C. et al., Turbulence modeling for CFD, Vol. 2, DCW industries La Canada, CA, 1998.

Willson, M. Dispersal mode, seed shadows and colonization patterns, Vegetatio, 107 (1993) 261-280. https://doi.org/10.1007/978-94-011-1749-4_19

Wilson, R. E. et al.: Aerodynamic Performance of Wind Turbines. Energy Research and Development Administration, ERDA/NSF/04014-76/1, 1976. https://doi.org/10.2172/7315651

Wiklak, P.; Kulak, M.; Lipian, M.; Obidowski, D. Experimental Investigation of the Cooperation of Wind Turbines. Energies 2022, 15, 3906. https://doi.org/10.3390/en15113906

Wood, D. Small Wind Turbines: Analysis, Design, and Application (Green Energy and Technology); Springer: Berlin/Heidelberg, Germany, 2011. https://doi.org/10.1007/978-1-84996-175-2

Yasuda, K.; Azuma, A. 1997 Journal of Theoretical Biology 185 313–320. https://doi.org/10.1006/jtbi.1996.0299

Zakaria, M.Y.; Dos Santos, C.R.; Dayhoum, A.; Marques, F.; Hajj, M.R. Modeling and prediction of aerodynamic characteristics of free fall rotating wing based on experiments. In Proceedings of the International Conference on Aerospace Sciences and Aviation Technology. The Military Technical College, Cairo, Egypt, 9–11 April 2019; pp. 1–15. https://doi.org/10.1088/1757-899X/610/1/012098

Zari, M. P. (2007). Biomimetic Approaches to Architectural Design for Increased Sustainability. Sustainable Building Conference.

Zhao, D., Han, N., Goh, E., Cater, J., Reinecke, A., 2019. Chapter 1 - general introduction to wind turbines. In: Zhao, D., Han, N., Goh, E., Cater, J., Reinecke, A. (Eds.), Wind Turbines and Aerodynamics Energy Harvesters. Academic Press. https://doi.org/10.1016/B978-0-12-817135-6.00001-6

Zeisberger, V.M. Derive New Profile Shapes for Efficient Smal Urban Wind Turbines—A Biomimetic Approach. Master' Thesis, University of Groningen, Groningen, The Netherlands, 2021.

Zhou, B.; Lu, J.; Lo, K. (2017) A Summary Study of Wind Turbine with Related Control. Energy and Power Engineering, 9, 270-280. https://doi.org/10.4236/epe.2017.94B032

ANNEX A – TORQUE METER

Features

Model	Lutron TQ-8800
Operating principle	Elastomer
Scale Kgf/cm	0...15 Kgf/cm
Scale Lbf/in	0...13.02 Lbf/in
Scale N/cm	0...147.1 N/cm
Resolution Kgf/cm "High" mode	0.01 Kgf/cm
Resolution Lbf/in "High" mode	0.01 Lbf/in
Resolution N/cm "High" mode	0.1 N/cm
Resolution Kgf/cm "Low" mode	0.1 Kgf/cm
Resolution Lbf/in "Low" mode	0.1 Lbf/in
Resolution N/cm "Low" mode	1 N/cm
Accuracy for all scales	$\pm1.5\% + 5$ digits
Sampling rate "Fast" mode	0.125 s
Sampling rate "Slow" mode	0.334 s
Maximum overload Kgf/cm	22.5 Kgf/cm
Maximum overload Kgf/cm	19.53 Lbf/in
Maximum overload N/cm	220.1 N/cm
Ambient temperature	< 80% RH
Sensor weight	665 g

Digital torque meter Lutron TQ-8800

ANNEX B – CERTIFICATE

impac comercial e tecnologia ltda.

CERTIFICADO DE CALIBRAÇÃO

NÚMERO	▉▉▉▉▉	PÁGINA	1 de 2

CALIBRAÇÃO REALIZADA EM	CERTIFICADO EMITIDO EM	VALIDADE RECOMENDADA
30/11/2022	30/11/2022	30/11/2023

CLIENTE
Empresa - Fundação de Apoio Universitário
Endereço - Rua Francisco Vicente Ferreira, 126 - Bairro Santa Mônica - Uberlândia - MG

OBJETO DO ENSAIO
Equipamento - Torquimetro Digital Lutron Modelo TQ-8800 nº série - 62426
Identificação - Não fornecido
Data do recebimento - Equipamento novo

CARACTERÍSTICAS DO OBJETO
* Faixa de Medição - (0 ... 15 Kg-cm x 0,01 ou 0,1 Kg-cm)
* Faixa de Medição - (0 ... 13,02 LB-inch x 0,01 ou 0,1 LB-inch)
* Faixa de Medição - (0 ... 147 N x 0,1 ou 1 N-cm)
* Precisão -   ± 1,5% + 5 digitos na temp. 23ºC± 5ºC
* Carcaça Plástica
* Leitura Digital
* Indicador - (LCD) Display de Cristal Líquido

CONDIÇÕES AMBIENTAIS
TEMP. AMBIENTE	23ºC	UMIDADE RELATIVA	66%

DESCRIÇÃO DO MÉTODO
* A incerteza dos resultados obtidos foi determinada conforme procedimento interno
* Esta Calibração foi realizada conforme Procedimento MEC-11.022
  Nível de Confiança de ≅ 95 % e K ≅ 2.

RASTREABILIDADE
* Esta calibração foi realizada utilizando os seguintes equipamentos :
* Jogo de pesos-padrão identificados através de tipagem marcados de 1 a 10 conforme relatado
no certificado de calibração Nº R-65271/20 sob etiqueta do INMETRO
num.CAL0091- Validade 07/10/2025
* Jogo de pesos-padrão identificados através de tipagem marcados de 1 a 10 conforme relatado
no certificado de calibração NºR-65270/20 sob etiqueta do INMETRO num.CAL0091- Validade 07/10/2025

OBSERVAÇÕES
* Nosso Laboratório opera de acordo com o previsto na norma NBR ISO/IEC 17025:2005
* Este Certificado é válido exclusivamente para o objeto ensaiado. A reprodução
 parcial ou total só será permitida mediante prévia autorização da Impac Comercial e Tecnologia.

GERENTE TÉCNICO	TÉCNICO
▉▉▉▉▉	▉▉▉▉▉

Rua: Murtinho Nobre, 17 Butantã - CEP 05502-050 - São Paulo - SP - Tel.: (11) 3816-0371
CNPJ: 64.112.295/0001-70   -   IE: 114.541.037.111
Site: www.impac.com.br   -   e-mail: vendas@impac.com.br

impac comercial e tecnologia ltda.

CERTIFICADO DE CALIBRAÇÃO

NÚMERO	███████	PÁGINA	2 de 2

TABELA DE RESULTADOS OBTIDOS NA CALIBRAÇÃO

OBS: Utilzada alavanca multiplicadora de 10 cm

PADRÃO (g)	TORQUE (Kg-cm)	ERRO (g)	DESVIO PADRÃO	INCERTEZA ± (g)
132,262	1,31	-1,26	0,05	0,11
209,392	2,08	-1,39	0,05	0,11
286,521	2,85	-1,52	0,03	0,10
341,654	3,40	-1,65	0,05	0,11
439,508	4,38	-1,51	0,03	0,10
516,048	5,14	-2,05	0,03	0,10
571,770	5,69	-2,77	0,05	0,12
669,742	6,66	-3,74	0,03	0,10
746,231	7,43	-3,23	0,05	0,12
822,726	8,19	-3,73	0,05	0,12
898,338	8,95	-3,34	0,03	0,10
1239,992	12,36	-3,99	0,03	0,10
1372,254	13,68	-4,25	0,05	0,12

PADRÃO (g)	DESCTORQUE (Kg-cm)	ERRO (g)	DESVIO PADRÃO	INCERTEZA ± (g)
132,262	-1,30	2,26	0,03	0,10
209,392	-2,06	3,39	0,03	0,10
286,521	-2,83	3,52	0,03	0,10
341,654	-3,38	3,65	0,05	0,11
439,508	-4,35	4,51	0,05	0,11
516,048	-5,12	4,05	0,05	0,11
571,770	-5,67	4,77	0,03	0,10
669,742	-6,63	6,74	0,03	0,10
746,231	-7,40	6,23	0,03	0,10
822,726	-8,16	6,73	0,03	0,10
898,338	-8,92	6,34	0,05	0,12
1239,992	-12,30	9,99	0,05	0,12
1372,254	-13,62	10,25	0,03	0,10

OBS: Os resultados referem-se à média de tres leituras

GERENTE TÉCNICO	TÉCNICO
███████	███████

Torque meter calibration certificate

ANNEX C – TACHOMETER

Features

Model	DT-2234C+
Accuracy	±0.05% + 1 digits
Sampling time	0.8 seconds.
Test interval selection	Automatic
Time Base	Quartz Crystal
Detection distance	approx. 50~500mm
Test range	2.5~9999RPM
Operating temperature	0-50°C, i.e. 0-50°C
Resolution	0.1RPM to 2.5~999.9 RPM
	1 RPM to over 1000 RPM

ANNEX D – SCANNER

3D STRUCTURED LIGHT SCANNER RANGE VISION STANDARD PLUS.

SCAN STRATEGY: Automatic rotating base.

Scanner specifications

Scanning area number	[1]	[2]	[3]	[4]	[D700]
Scanning Area (WxHxD) (mm)	460*345*345	300*225*225	133*100*100	66*50*50	920*690*690
3D point accuracy*	0.085 mm	0.05 mm	0.03 mm	0.03 mm	0.16 mm
3D resolution:					
Standard/ Standard Plus	0.35 mm	0.23 mm	0.1 mm	0.05 mm	0.7 mm
Advanced	0.3 mm	0.2 mm	0.085 mm	0.043 mm	0.6 mm
Premium	0.18 mm	0.12 mm	0.05 mm	-	0.35 mm
Operating distance	0.9 m	0.52 m	0.3 m	0.27 m	2 m

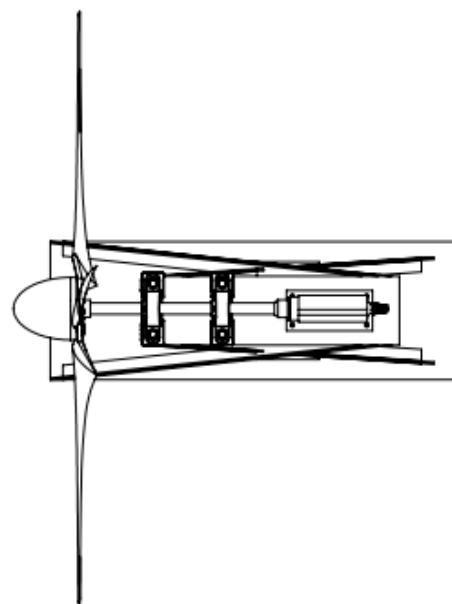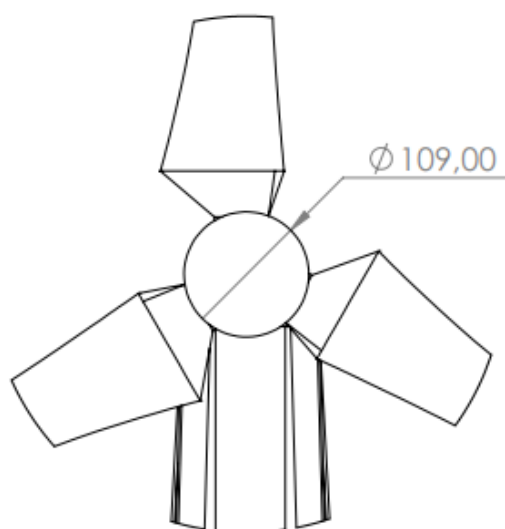| Model	Standard	Standard Plus	Advanced	Premium
Resolution of cameras	1,3 Mpix	1,3 Mpix	2 Mpix	5 Mpix
Matrix diagonal, body of the cameras	1/2", plastic	1/1.8", metal	1/1.8", metal	2/3", metal
Scanning time	~ 7 sec	~ 7 sec	~ 12 sec	~ 15 sec
Model calculation time	~ 5 sec	~ 5 sec	~ 10 sec	~ 20 sec
Scanning black	-	-	+	+

ANNEX E – TECHNICAL DRAWING
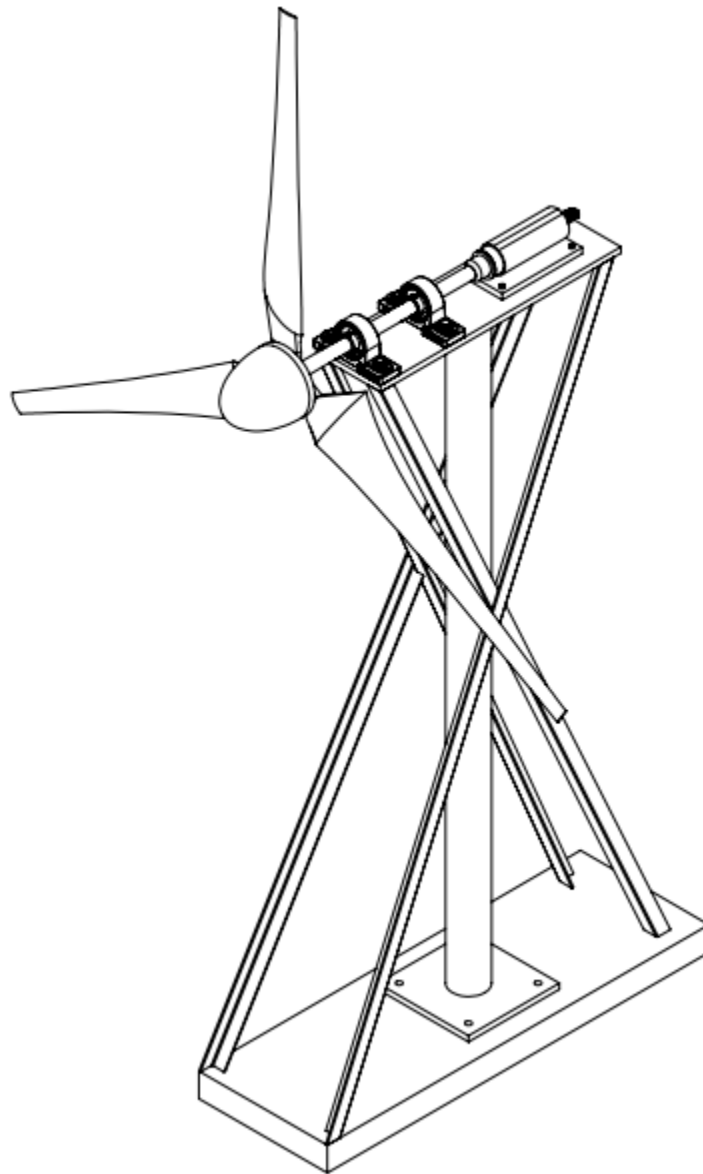
Technical drawing of the components of experimental wind turbine bench
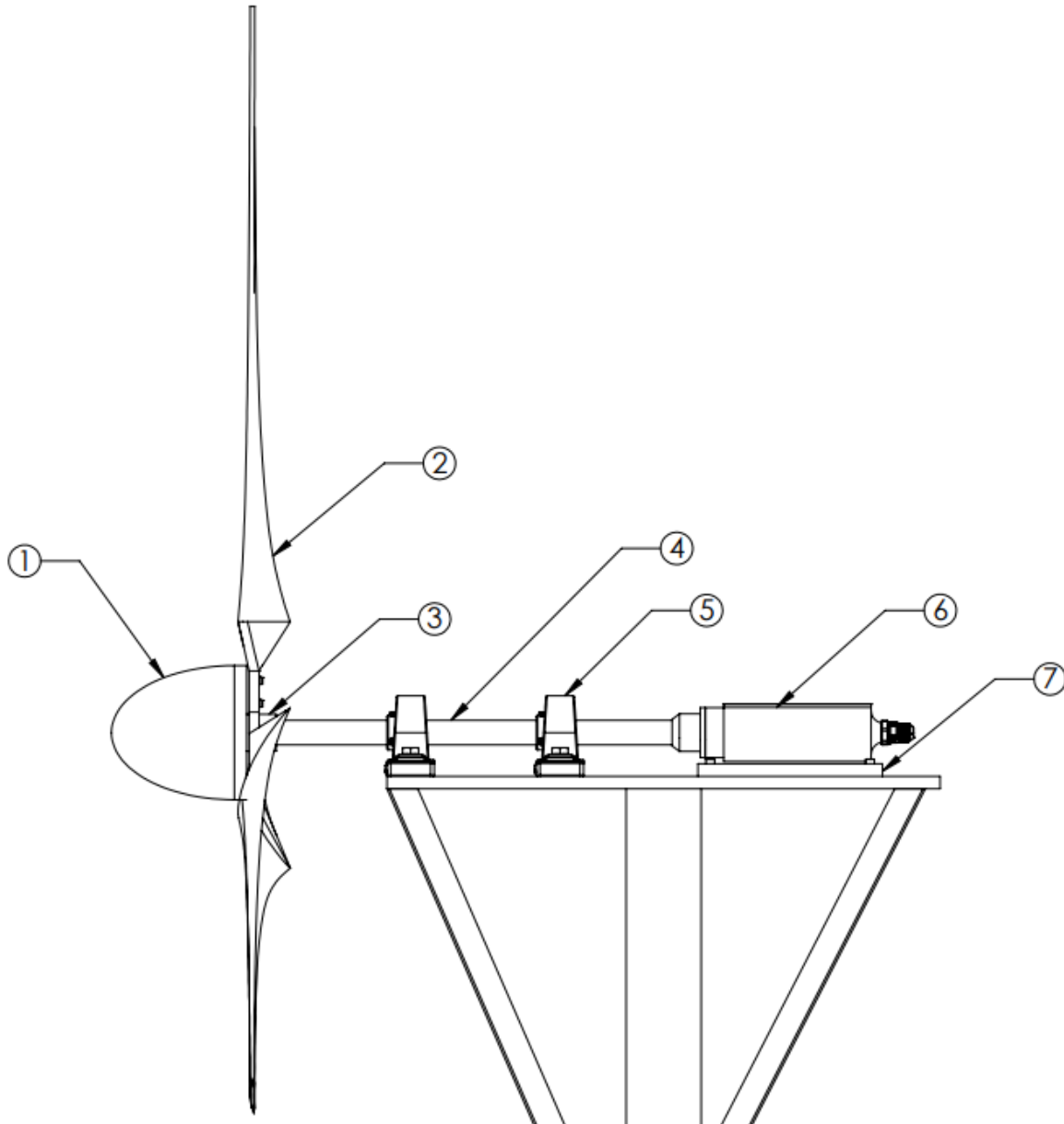
Component	Description
1	Nose cone
2	Blade
3	Hub
4	Shaft
5	Bearing housing unit
6	Torque meter
7	Bench

Ø 109,00

DETALHE A

ESCALA 1 : 6

Ø 1180,30

A

Ø 61,00

112,00

42,37

1200,00

45,00

715,00